An Investigation into the Causes for the Reduction in the Variability of the El Niño-Southern Oscillation in the Early Holocene in a Global Climate Model

William Henry Gordon Roberts

A dissertation submitted in partial fulfillment
of the requirements for the degree of

Doctor of Philosophy

University of Washington

2007

Program Authorized to Offer Degree: Atmospheric Sciences

University of Washington
Graduate School

This is to certify that I have examined this copy of a doctoral dissertation by

William Henry Gordon Roberts

and have found that it is complete and satisfactory in all respects,
and that any and all revisions required by the final
examining committee have been made.

Chair of the Supervisory Committee:

_____

David Battisti

Reading Committee:

_____

David Battisti

_____

Dennis Hartmann

_____

Christopher Bretherton

Date: _____

In presenting this dissertation in partial fulfillment of the requirements for the doctoral degree at the University of Washington, I agree that the Library shall make its copies freely available for inspection. I further agree that extensive copying of this dissertation is allowable only for scholarly purposes, consistent with "fair use" as prescribed in the U.S. Copyright Law. Requests for copying or reproduction of this dissertation may be referred to Proquest Information and Learning, 300 North Zeeb Road, Ann Arbor, MI 48106-1346, 1-800-521-0600, to whom the author has granted "the right to reproduce and sell (a) copies of the manuscript in microform and/or (b) printed copies of the manuscript made from microform."

Signature_____

Date_____

University of Washington

Abstract

An Investigation into the Causes for the Reduction in the Variability of the El Niño-Southern Oscillation in the Early Holocene in a Global Climate Model

William Henry Gordon Roberts

Chair of the Supervisory Committee:
Professor David Battisti
Atmospheric Sciences

A large body of evidence shows that during the early Holocene the variability on interannual timescales in the tropical Pacific was much reduced in comparison to today. We investigate a possible cause for this using output from a Global Climate Model forced by present day and early Holocene boundary conditions, and a simplified model that is known to simulate the El Niño-Southern Oscillation(ENSO).

We devise a scheme to incorporate mean state data into the background states of a linearisation of the Zebiak and Cane model (Zebiak and Cane, 1987), due to Thompson and Battisti (2000). We show that when sets of background states are compiled using observations of the present climate that ENSO mode in the linearised model is stable.

Using the method for incorporating mean state data into the linearised coupled model on output from the Community Climate System Model (Otto-Bliesner et al., 2003) run with present day an 8.5 thousand years before present(ka) forcing we find that the mean state change in the tropical Pacific at 8.5ka is sufficient to explain the reduction in the variance of the model's nino3 index. We show that changes in the ocean are not responsible for increasing the stability of the ENSO mode, and decreasing the variance of the modelled

nino3, but are responsible for changing the pattern of the ENSO variability at 8.5ka. We show that the general cooling in the sea surface temperature at 8.5ka, compared to today, results in a reduction in the windstress variance which acts to stabilise the ENSO mode, and so reduce the variance of nino3 at 8.5ka.

Table of Contents

List of Figures

List of Tables

Acknowledgments

Thanks to those who made the time
I spent upon this thesis,
Such a pleasant and fruitful stretch,
I did not fall to pieces.

To those who funded my travail
And advised me in my labour,
I offer thanks and hope you find
This thesis meets your favour.

Ma and Pa, thank you for everything.

Chapter 1

Introduction

1.1 Introduction

A large body of evidence suggests that around 8.5 thousand years ago (8.5ka) there was much reduced climatic variability in the tropical Pacific on interannual timescales. The dominant source of interannual variability on interannual timescales in the tropical Pacific is the El Niño-Southern Oscillation (ENSO), so a reduction in sea surface temperature (SST) variability on interannual timescales implies a reduction in the activity of ENSO. To date none of the hypotheses that have been put forward to explain this reduced variance due to ENSO have ever been tested. It is the purpose of this thesis to develope a tool that may be used to examine what could cause a reduction in the amount of interannual variability due to ENSO during the early Holocene, and to use it to diagnose the cause of the reduction in ENSO variance from 8.5 ka to the present as modelled by a Global Climate Model (GCM).

For the rest of this introduction we shall describe in more detail the observational evidence detailing the climate of the early Holocene, with a special focus on the mean state and interannual variability in the tropical Pacific. We shall then describe what models tell us about the early Holocene climate in the tropical Pacific as well as what hypotheses have been put forward to explain the reduction in ENSO variability. We shall then summarise how the rest of this thesis is laid out.

1.2 The Early Holocene Climate

1.2.1 Globally

The annual mean climate during the early Holocene, between 10 and 6 ka, was generally very similar to today's. The global temperature had already risen since the last ice age, melting the ice sheets and leaving the continental geometry and sea level much the same as today. The global atmospheric concentration of CO_2 of about 270ppm (see for example Broecker and Stocker, 2006), was very close to the preindustrial value. The major change in the forcing of the climate from 10 ka until around 1850 was the change in insolation due to orbital variations. During the early Holocene, the time of perihelion was in late August: today it occurs in December. This meant that in the northern hemisphere, the summer maximum of insolation was about 5% stronger than today. Conversely, during winter the northern hemisphere minimum insolation was about 5% less than today. This enhanced seasonal cycle of insolation in the northern hemisphere is suggested to have strengthened the monsoons (see for example Liu et al. (2004) and references therein). Indeed a large body of paleo-evidence shows that the monsoons were stronger, for example the northern African Monsoon extended much farther inland than today (Street-Perrott and Perrott (1993), Jolly et al. (1998)) and the Asian monsoon stronger (e.g. Vancampo et al. (1982) and Dykoski et al. (2005)).

We shall now describe what is known about the climate of the tropical Pacific in the early Holocene, starting with the interannual variability.

1.2.2 Interannual Variability

Tudhope et al. (2001) examined a time series of $\delta^{18}O$ measured in uplifted corals in Papua New Guinea and found 80% less variance on interannual timescales at 6.5ka than today. Figure 1.1 shows the location of this, and other, proxy-data sources described in this section. The $\delta^{18}O$ reflects a mixture of salinity and SST changes, with high $\delta^{18}O$ showing cooler

and/or saltier conditions. At present, on interannual timescales, both cooler and saltier conditions in the surface ocean off Papua New Guinea are associated with the warm phase of ENSO, when the precipitation in the western tropical Pacific is shifted farther east, away from Papua New Guinea. Thus the reduction in the variance of $\delta^{18}O$ at 6.5ka is inferred to reflect a decrease in ENSO activity.

McGlone et al. (1992) and Shulmeister and Lees (1995) both show that in Australia before around 6ka the types of pollen present came from plant species that were not resistant to drought. Absence of drought resistant plants indicates an absence of drought which, because drought in this region is highly correlated with the warm phase of ENSO, indicates an absence of ENSO. Also from Australia, Lees and Y. Lu (1992) show that there was more interannual dune activity after about 3ka. Again, this indicates that during the early Holocene there was less interannual variability over eastern Australia, than in the modern climate.

In the east Pacific, Sandweiss et al. (2001) examined the species of mollusc shells left in archaeological middens, and concluded that there was a shift to more variability in SST off the coast of Peru around 6ka. SST variability there is strongly correlated with ENSO activity. However, DeVries and Diaz (1997) and Wells and Noller (1997) both contend that there are other ways to interpret these data: rather than pan-east Pacific changes in SST; the molluscs only reflect SST changes in their immediate vicinity. In the Andes, Moy et al. (2002) argue, using records of flood debris into Lake Pallcacocha, that there were fewer flood events before 5ka than after. At present flood events into Lake Pallcacocha generally occur during the warm phase of ENSO, so an absence of flood events is assumed to reflect an absence of ENSO activity before 5ka.

All told, these data paint a fairly coherent picture that the present amount of tropical Pacific interannual variability due to ENSO began some time after about 6ka. It is less clear what the Tropical Pacific mean state looked like in the early Holocene.

1.2.3 Mean State of the tropical Pacific in the early Holocene

Looking first at SST in the far west Pacific, Gagan et al. (1998) examined the Sr/Ca and $\delta^{18}O$ taken from Great Barrier Reef corals, and concluded that the SST was possibly 1.2°C warmer in the warm pool during the early Holocene. Stott et al. (2004) examined Mg/Ca from sediment foraminifera from sites around the warm pool and concluded that the west Pacific was around 0.5°C warmer than today. Both studies show a warmer warm pool, but the estimate of Gagan et al. (1998) is more than twice that of Stott et al. (2004). The derivation of SST from coral Sr/Ca (Devilliers et al., 1995), is somewhat less certain, which could explain the larger SST change derived by Gagan et al. (1998) than Stott et al. (2004). It is possible that Sr/Ca uptake by corals is highly dependent upon their biology, leading to possibly large errors in the SST derived from the Sr/Ca ratio (Devilliers et al., 1995). The estimates of the SST change from $\delta^{18}O$ in Gagan et al. (1998) are smaller than those from Sr/Ca; although Gagan et al. (1998) hypothesise that this is primarily due to differences in salinity, it is also possible that the Sr/Ca approximations are an overestimate. Thus, although the data consistently point towards warmer SST in the warm pool during the early Holocene than today, the exact magnitude is not well constrained, but most likely lies between 0.5 and 1.2°C.

Looking at eastern Pacific SST, Koutavas and Lynch-Stieglitz (2003) argue that sediment cores taken from near the Galapagós show that the SST there was around 1°C lower at 10ka than today. The proxies used are $\delta^{18}O$ and Mg/Ca taken from various species of near surface dwelling foraminifera. In contrast, Lea et al. (2006) contend, again using foraminiferal $\delta^{18}O$ and Mg/Ca, that the east Pacific SST was in fact about 1°C warmer at 10ka. These two analyses, using the same proxies taken from the same general area, draw two very different conclusions. A possible explanation for this is that, as the cores were all taken from very close to the Galapagós islands, coastal effects, such as local upwelling, played a large role in determining the SST recorded by the foraminifera there. Thus the derived SST

is representative only of the immediate vicinity of the core site, rather than the broader east Pacific. Furthermore the strong equatorial SST front lies around the core sites, and a very small meridional shift in the front could cause a significant change in the SST. Therefore it is not clear whether these data show a shift in the equatorial front, a change in local upwelling or a pan-east Pacific change in SST.

There are also a number of records from the east Pacific that describe the early Holocene rainfall there. Baker et al. (2001) using Lake Titicaca, and Bush et al. (2005) using Lake Chochos sediment cores, report that the lake levels were lower before 5ka than after. Thus they infer that the rainfall in the Andes was less before 5ka than after. Colinvaux and Schofield (976a,b) use Galapagós lake levels to show that the rainfall there was less during the early Holocene. All these data indicate a drier east Pacific, but it is not obvious what causes this. Rainfall in the Andes is strongly dependent upon the large scale flow, so a change in precipitation there could be determined well outside the tropical Pacific. Rainfall in the Galapagós strongly correlates with ENSO, so the reduced rainfall there could be due to the reduced ENSO activity rather than due to a general drying of the east Pacific. As with all proxies, interpretation to a wider perspective is difficult.

Finally, Thompson et al. (2000) show using Andean glacier ice core $\delta^{18}O$ that the early Holocene was warmer than the present. What is not clear is what the ice cores tell us about where it was warmer, since the source of the water that gives the $\delta^{18}O$ record is not precisely known. Vuille (1999) shows that it is possible that the $\delta^{18}O$ signature in the Andean ice cores is actually a response to changes in the climate over the Amazon basin, whence the precipitated water comes.

All these data do not give an entirely consistent description of the mean state climate in the early Holocene. There is general agreement that the west Pacific was warmer than today, but outside the far west Pacific there are sparse and contradictory data on the mean state climate.

Having described how the observations describe the early Holocene tropical Pacific cli-

mate, we shall now describe the view from climate models.

1.3 The Early Holocene - models

Outside the tropical Pacific, where data are very limited, observations show that the annual cycle during the early and middle Holocene was very different from that of the present. The monsoons, especially the African, were all stronger than today (see for example Liu et al., 2004, and references therein). This makes a good test case to study the performance of GCMs in altered climate regimes. Indeed 6ka is a target run in the Paleo Model Intercomparison Project (PMIP). Although 6ka is somewhat close to the period when proxies show that the interannual variability in the tropical Pacific was changing most, there are a good number of model runs that have attempted to model this time during the mid Holocene. Since the goal of this thesis is to examine tropical Pacific interannual variability, we shall describe in detail only those models that have examined how their tropical Pacific interannual variability changed at 6ka. In less detail, we shall also describe those models that have shown how the mean state of the tropical Pacific changed at this time.

Otto-Bliesner (1999), using an early version of Community Climate System Model (CCSM), found no change in the model's interannual variability at 6ka compared to today. In the mean the SST over the tropical Pacific cooled, especially in the east. It should be noted that the model's tropical Pacific interannual variability is much weaker than today and does not show the same spectral characteristics as observed.

Clement et al. (2000) using the Zebiak and Cane model (Zebiak and Cane, 1987) to model the tropical Pacific throughout the last 12 thousand years found fewer large warm events during the early part of the Holocene than there are today. We should note that the model used in this study is not global.

Liu et al. (2000) using the Fast Ocean Atmosphere Model found a 20% reduction in the variance of nino3 at 6ka and 11ka compared to today. This reduction in interannual variance is smaller than that observed (c.f. Tudhope et al., 2001, who report an 80% decrease in

variance on interannual timescales). In the far west Pacific, however, the model's SST variance increased, which is not consistent with any paleo-record. In the mean, the tropical Pacific SST cooled. Beneath the thermocline in the east Pacific, the temperature was seen to warm and combined with the surface cooling, this acted to reduce the strength of the thermocline.

Otto-Bliesner et al. (2003) using a later version of CCSM, the CSM 1.4 (hereinafter paleoCCSM) described in Otto-Bliesner and Brady (2001), found that the variance of the model's nino3 was reduced to 80% of the present in a 6ka run. The model was also run at 8.5ka and this run also showed a 20% reduction in variance compared to the modern climate. 8.5 ka is a better time to examine the tropical Pacific than 6ka, because much of the proxy evidence indicates that a change in the climate occurred around 6ka. In the mean, both the 6 ka and 8.5 ka runs showed a tropical Pacific that was around 1°C cooler than today, especially in the east over the cold tongue. The easterly Trades were stronger in both runs and the thermocline was also weaker at 6ka and 8.5ka than today. This was due to a warming beneath the thermocline and a cooling at the surface.

Brown et al. (2006) using HadCM3 show a 10% reduction in the variance of the model nino3 index at 6ka. This difference however is within the range of the models interdecadal variability so it is hard to argue its significance. In the annual mean the tropical Pacific SST is cooler everywhere at 6ka by no more than 1.0°C. Seasonally, the cold tongue is cooler during the winter and warmer during the summer at 6ka also the easterly Trades are stronger during the summer at 6ka.

A number of other models have also shown their tropical Pacific mean state in the early Holocene. Bush (1999), Kitoh and Murakami (2002) and Liu et al. (2003), all show a general cooling of the tropical Pacific of between 0.5°C to 1.0 °C, with a maximum cooling of the cold tongue at 6ka. All these models also show stronger Trades at 6ka compared to the present. These stronger Trades are hypothesised to be due to either the stronger Asian Monsoon, which forces a stronger Walker circulation (Liu et al., 2000, 2003), or due to a

stronger flux of easterly momentum from mid-latitudes to the tropics (Bush, 2001).

Given that some models have managed to reproduce the observed reduction in ENSO, what are the proposed hypotheses to account for this?

1.4 Hypotheses

Clement et al. (2000) argue that a seasonal strengthening of the Trades in the early Holocene inhibits the growth of an incipient ENSO event. Their argument goes as follows: as a result of the stronger zonal SST gradient during autumn, the easterly Trades are then stronger. These seasonally stronger easterlies act to reduce the amplitude of any westerly wind anomalies that arise from ENSO. This argument does not seem to be self-consistent however, since the windstress goes as the square of the windspeed, larger windstress anomalies will result from any windspeed anomalies superposed on a stronger mean wind. Therefore the coupled system will tend to be less stable, so we would expect more variance in ENSO rather than less. Further inconsistencies in the argument are outlined in appendix A along with a re-examination of why the model produces the reduced variance in the early Holocene. For the present discussion, suffice to say, that it is not obvious how the results presented in Clement et al. (2000) can be applied to the real world.

Liu et al. (2000, 2003) propose that the stronger Asian monsoon during the early Holocene causes an amplification in the seasonality of Trades. They propose that this seasonal change then tends to inhibit the growth of ENSO windstress anomalies, although this hypothesis is never examined. However as is discussed by Wang and An (2002) there is no reason why a change in the seasonal cycle of the Trade winds would cause a reduction in ENSO variability.

Liu et al. (2000) also show that in FOAM at 6ka the vertical temperature gradient over the thermocline weakens and they then hypothesise that the reduction in the vertical temperature gradient stabilises ENSO. They hypothesise that the change in the vertical temperature gradient is due to a shift in the location of the subduction of the waters that

are subducted into the thermocline.

All of the above hypotheses that are proposed to explain the reduced variance of ENSO in the early Holocene invoke changes in the mean state. Most also propose that it is an increase in the amplitude of the seasonal cycle that promotes the change. There is, however, no logical argument that supports this hypothesis. A further possible way to reduce the variance due to ENSO is to change the structure or amplitude of the noise forcing. Chiang (2007, personal communication) have shown that in their model, at 6ka the pattern that stochastically forces the model's ENSO displays less variance. The reduced variance in this forcing pattern is hypothesised to lead to less variance in the modelled ENSO.

We shall propose a new hypothesis for how ENSO was suppressed during the early Holocene in the paleoCCSM. Using a simple model known to simulate ENSO and output from the paleoCCSM, the model that most closely captures the observed reduction in ENSO variance, we shall show that the general cooling of the tropical Pacific at 8.5ka reduces the windstress variability, which in turn reduces the variance due to ENSO.

1.5 Goals of the Thesis

The goal of the thesis is to examine why the 8.5ka paleoCCSM run performed by Otto-Bliesner et al. (2003) displays reduced SST variance in the tropical Pacific (in particular the region associated with ENSO), when compared to the present day run of the model. We shall do this by examining the structure and stability of the coupled model's ENSO when it is approximated by a linearised version of the Zebiak and Cane model (Zebiak and Cane, 1987, ZCM). We shall examine ENSO in this simplified framework using background states from the present day and 8.5ka runs of the paleoCCSM. First we will need to come up with a system that assimilates climatological mean data into the linear model. In order to verify that the system works, we shall first assimilate the climatological mean state from observations into the linear model and show that the linear model can produce an ENSO mode that is consistent with that observed. Having verified that the procedure

for calculating the background states works for the observed climate, we then apply the technique to the output from paleoCCSM. We will show that the ENSO mode that results from the linearised model is consistent with that which comes from the CCSM. We will show that the reduced variance in ENSO in the 8.5ka run, compared to the present day run, is due to a change in the mean state at 8.5ka: no change in the amplitude of the noise forcing is necessary. Finally we will show that the most important processes in determining the stability of the ENSO mode in paleoCCSM are the change in the models response to thermocline displacements, which destabilises and lengthens the ENSO mode, and the general cooling of the SST, which stabilises the ENSO mode. In the net, the cooling effect dominates the thermocline effect so the model's ENSO variability is decreased in the early Holocene in comparison to the present day.

In Chapter 2, we shall first describe the physics of the linear model that we shall use as a diagnostic tool. Then we shall describe a way of taking three dimensional climatological data and processing it so that it may be used in linearised model. Throughout the chapter we will derive a set of background states using real data from the present day to show how the process works. We will compare these new background states to those originally used in the Zebiak and Cane model.

Chapter 3 will verify that the process outlined in Chapter 2 produces valid mean states by stochastically running linearised model with the new background states. We will show that the new background states perform as well, if not better, than those used in the original Zebiak and Cane model. We will show that after independently tuning the atmosphere and ocean to best fit the observations, the leading eigenmode of the coupled system is consistent with the canonical cycle of ENSO, and that this "ENSO mode" is stable. This lends weight to the hypothesis that in nature ENSO may be thought of as being a damped mode of the coupled atmosphere ocean system in the tropical Pacific.

In Chapter 4, we will analyse the stability of the ENSO mode in the present day and 8.5ka simulations of the CCSM. We will show that the linearised model accurately repre-

sents the original model's interannual variability. We will then compare the present day and 8.5ka model runs and will show that changes in the background states of both ocean and atmosphere are sufficient to explain the change in the structure and amplitude of the variance in the tropical Pacific. We shall show that the change in the stability of the ENSO is sufficient to explain all of the observed reduction in the model's nino3 variance: no change in the noise forcing is required to effect the change. We will show that the change in the mean thermocline background state tends to destabilise the system, whereas the change in the atmospheric response to SST anomalies tends to stabilise the system. In the net the ENSO mode at 8.5 ka is stabilised because the reduced sensitivity of the atmospheric response to SST is is more important than the increases sensitivity of the ocean to windstress anomalies. We will show that changes in the seasonal cycle are not important for explaining any reduction in the variance of ENSO in the early Holocene.

Finally, in Chapter 5, we will summarise the findings of the thesis, and discuss their implications. We will discuss how the framework for examining the importance of background state changes to ENSO that is developed in the thesis may be applied to examine how the ENSO may change in the future.

In Appendix A we will discuss in more detail the results of Clement et al. (2000). We will explain how the ZCM as used by Clement et al. (2000) can give the reduced number of warm events that is does, and show that this is due to model limitations rather than a real physical phenomenon. Furthermore, we shall show that within the model framework the given explanation is not entirely consistent.

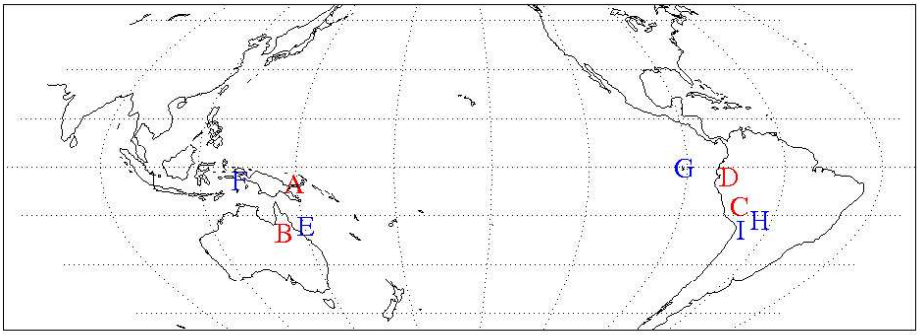

Figure 1.1: Summary figure of the cited paleo-datasets. Blue letters are datasets detailing the mean state changes and red those indicating changes to the interannual variability. A: Tudhope et al. (2001); B: McGlone et al. (1992), Shulmeister and Lees (1995) & Lees and Y. Lu (1992); C: Sandweiss et al. (2001), DeVries and Diaz (1997) & Wells and Noller (1997); D: Moy et al. (2002); E: Gagan et al. (1998); F: Stott et al. (2004); G: The Galapagós, Koutavas and Lynch-Stieglitz (2003), Lea et al. (2006), Colinvaux and Schofield (976a,b); H: Baker et al. (2001) & Bush et al. (2005); I: Thompson et al. (2000).

Chapter 2

New Background State Calculation

2.1 Introduction

During the late 1980s, when the Zebiak and Cane model (Zebiak and Cane, 1987, hereafter ZCM). was first written, atmospheric and oceanic data in the tropical Pacific were pretty sparse. The SST and windstress were reasonably well observed with the Rasmusson and Carpenter (1982, hereafter referred to as RC) 30 year climatologies, but the temperature beneath the surface was not well observed. Furthermore, ocean current measurements in the Pacific ocean basin were virtually non existent. This lack of observations meant that in order to have a full set of background states to prescribe in the model, Zebiak and Cane (1987) needed to make some approximations. The mean ocean currents and upwelling were estimated by forcing the 1.5 layer ocean model with the RC climatological windstress and calculating the resultant seasonal cycle of the currents. Subsurface temperature parameterisations, which are also needed in the model, were devised on an *ad hoc* basis.

Now, twenty-some years after the model was written, the tropical Pacific ocean is much better observed. The TAO array (McPhaden et al., 1998) makes real-time measurements of the ocean temperature within 10° of the equator all along its east to west span, to depths of hundreds of metres. Satellites give observations of the windstress and SST, and a number of model-data assimilation products also give ocean current data. With all these new data we can now calculate background states that far more accurately represent the true mean state of the tropical Pacific than those that were originally used in the ZCM. In this chapter we shall describe how these new data may be used to make new sets of background states to prescribe in a linearised version of the ZCM. This same method will also serve as a way to

assimilate mean field output from a GCM into the linearised model. Furthermore the more extensive subsurface data allows us to calculate more accurate subsurface parameterisations that are designed to empirically fit the observations.

With this new set of background states and subsurface parameterisations we shall be able to fit the remaing parameters, that were arbitrarily chosen in ZCM, to give the best possible model of the tropical Pacific ocean and atmosphere in the simplified ZCM framework. This will be done by tuning the ocean and atmosphere to give the best fit to the obesrved anomalies.

This chapter shall proceed as follows. First we shall describe in detail the variant of the ZCM that we shall use, then we shall describe the horizontal background states and show how the new states differ from those originaly used. Next we shall describe how the subsurface parameterisations can be calculated from the data. Finally we shall describe how the remaining parameters in the two model components can be determined from the best fit of the uncoupled component models to the observed record of interannual anomalies.

2.2 Simple ENSO Models

The simple model of the coupled atmosphere-ocean system that we shall use is a linearised version of the ZCM which, as is described extensively in the literature, is an anomaly model about a prescribed set of background fields that vary over the annual cycle. When the model is run it produces interannual SST anomalies that broadly replicate the observed pattern of ENSO. This model has an irregular ENSO cycle. Battisti (1988) rewrote the ZCM to produce what we shall call B88M. The minor differences in the parameters used in ZCM and B88M are extensively discussed in Mantua and Battisti (1995). The biggest difference that results from the parameter differences between the two models is that the ENSO cycle in B88M is regular. This allowed Battisti (1988) to diagnose the processes important in the model's ENSO and then to hypothesise that the dynamics principally responsible for the interannual variability are linear (Battisti and Hirst, 1989). In linearising the system

Battisti and Hirst (1989) found that this linear viewpoint held true, as the model still produced interannual variability very similar to the full nonlinear system. In thinking of the system as linear, one can envision the system as being dominated by the ENSO mode: the ENSO mode will be the least damped Floquet mode of the linear system[1].

The next step in the evolution of the ZCM was due to Thompson and Battisti (2000). Using the linearisation of Battisti and Hirst (1989), Thompson and Battisti (2000) reformulated the ZCM model into a single matrix to describe the time evolution of the model (see Thompson, 1998, for a more detailed discussion of the formulation of this model). This model was given the name the Linear Ocean Atmosphere Model (LOAM). As was described in Thompson (1998) some of the parameters in the original ZCM were not set to values that well reflect their actual value in nature (although the prescribed mean fields were the same as those originally used in Zebiak and Cane (1987)). Thus Thompson (1998) undertook a number of parameter studies to give these parameters values that better represent the real system. The western boundary reflection coefficient was set to 0.7, rather than 1.0, and the ocean mechanical damping coefficient was set to 8.7 month^{-1} rather than 30 month^{-1}. A summary of the constants used by Thompson (1998) in LOAM, is shown in Table 2.1. The leading eigenmode of LOAM with these values of western boundary reflection and ocean damping is very close to the canonical ENSO, hence it was called the ENSO mode. This mode has a period of 3.8 years and decays at a rate of 0.8 year^{-1}. LOAM with this set of parameters was given the name $LOAM$(T80). Because the ENSO mode (and all other modes) of $LOAM$(T80) are damped, to run the model it must be stochastically forced. In $LOAM$(T80) this forcing is spatial and temporal white noise applied to the SST field: in nature the leading idea is that the stochastic forcing is provided by wind variability that is independent of the state of ENSO (see for example Goddard and Philander, 2000).

[1]The irregular ENSO cycle in ZCM is due to the nonlinear interaction between the first two modes of the coupled system, the ENSO mode and the mobile mode. The mobile mode is a an unstable coupled mode in the ZCM that is not observed in nature (Mantua and Battisti, 1995; Zebiak, 1984).

The model that we shall use is based upon $LOAM$(T80), but shall make further parameter changes and use a set of background states that more accurately model the observed mean state than do the background states used in ZCM, B88M or $LOAM$(T80).

2.3 Surface means

The horizontal background states are derived by calculating monthly averages from the observed data and interpolating them onto the LOAM atmosphere and ocean grids. The background states required are: surface winds, SST and surface ocean currents.

Available wind stress products are from Florida State University (Bourassa et al., 2001, hereafter referred to as FSU), shown in fig. 2.1(a)-(f), and the NCEP reanalysis, (Kalnay et al., 1996) [2], shown in fig. 2.2(a)-(f). There are significant differences between these two datasets themselves and between these datasets and the RC climatologies originally used in ZCM. We see in figs. 2.1(a)-(c) and 2.2(a)-(c) that the easterly Trade winds from both FSU and NCEP are stronger than the RC Trades, especially in the east central Pacific. In figs. 2.1(d)-(f) and 2.2(d)-(f) we see that the observed meridional winds are also stronger than their RC counterparts. What is also notable in fig. 2.3(a)-(c), is that the equatorial Trades in FSU are stronger than those in NCEP.

The SST from the Simple Ocean Data Assimilation (Carton et al., 000b,a, hereafter referred to as SODA) and the NCEP/OI data (Reynolds et al., 2002) [3] are shown in figs. 2.1(g)-(i), 2.2(g)-(i) and 2.3(g)-(i). We see in figs. 2.1(g)-(i) and 2.2(g)-(i) that both SODA and NCEP show a much stronger cold tongue than the original SST used in ZCM ; this gives a stronger zonal temperature gradient. We see in fig. 2.3(g)-(i) that the SODA and NCEP/OI SST agree well with each other, and that the difference between the original SST in ZCM

[2]NCEP Reanalysis Derived data provided by the NOAA/OAR/ESRL PSD, Boulder, Colorado, USA, from their Web site at http://www.cdc.noaa.gov/

[3]NOAA_OI_SST_V2 data provided by the NOAA/OAR/ESRL PSD, Boulder, Colorado, USA, from their Web site at http://www.cdc.noaa.gov/

and the NCEP/OI and the SODA SST is greater than the difference between the NCEP/OI and SODA SST.

The currents needed are averages over the top fifty metres of the ocean. This 50m is the depth of the surface layer that is embedded in the 1.5 layer ocean in ZCM. Surface currents are harder to remotely observe than either windstress or SST, and, as a result, background states for these are from model-data assimilations. The two assimilation products that we shall use are the Global Ocean Data Assimilation System (Behringer and Xue, 2004, hereafter referred to as GODAS) and SODA (Carton et al., 000b,a). Both assimilate available observations of temperature and climatological salinity into ocean models, which are then forced with observed winds and various surface fluxes, to produce full three dimensional fields which include currents and temperature. Recall that the background ocean currents in the original in ZCM were computed using the 1.5 layer ocean model forced by the RC winds. Hence the original ZCM currents present a much cruder representation of the currents than the assimilation products. The ocean model used in both assimilations is the Geophysical Fluid Dynamics Laboratory, Modular Ocean Model.

Zonal currents from SODA and GODAS, which are shown in fig. 2.4(a)-(c), agree with each other: there is westward flow flanking the equator and eastward flow on the equator. There is, however, little agreement between the currents from either of the two assimilation products and those used in ZCM: see figs 2.5(c) and 2.6(c) for the difference between the currents from ZCM and, SODA and GODAS, respectively. Absent the ZCM background currents is the reversal of the current on the equator at around 250°E; this is the equatorial undercurrent coming to the surface. In the ZCM background state the maximum in the north equatorial counter current is located farther to the west than in either of the assimilation products. Meridional currents in SODA and GODAS broadly agree, as is shown in fig. 2.4(d)-(f), however, as is shown in figs. 2.5(d)-(f) and 2.6(d)-(f), ZCM currents are too strong in the far east. This results in too much divergence away from the equator in the ZCM mean currents and, as can be seen in figs. 2.5(g)-(i) and 2.6(g)-(i), this means

that the ZCM upwelling strength is much stronger than that in either of the assimilation products. Furthermore, the maximum upwelling is displaced farther east in LOAM than in the assimilation products. The differences between the current estimates from the model-data assimilations and the 1.5 layer model can mostly be explained by the differences in the models used. Using the same windstress product that forced the ocean model in GODAS to force the 1.5 layer model used in the ZCM, results in currents that are very similar to those obtained by forcing the 1.5 layer model with the RC winds. Hence we may conclude that the differences in the windstress from RC compared to NCEP are not the cause of the differences in the current patterns, rather it is the difference in the ocean models.

We have shown in this section that there are significant differences between the best estimates of the present climatological background states and those originally used in *LOAM*(T80) and ZCM. These background states are not the only fields that need to be specified in order to run LOAM. There remains the two subsurface parameterisations, which were originally derived on a somewhat *ad hoc* basis, to be specified: these are discussed next.

2.4 Subsurface Mean Fields & the Estimate of a Parameterisation for Ocean Entrainment and Mixing.

Subsurface temperature data are available from a number sources. From direct observations there is the Bureau of Meteorology Research Centre analysis (Smith, 1995a,b, hereinafter referred to as BOM). BOM takes all the available temperature data, such as XBT, CBT and TAO data and interpolates it onto a three dimensional grid. Three dimensional temperature fields are also available from the two model-data assimilation products, SODA and GODAS.

The ZCM includes an ocean thermodynamic equation for the top 50m of the ocean. In LOAM the linearisation of the SST tendency equation for this layer is written (see Thompson, 1998, for more details):

$$\frac{\partial T}{\partial t} = -u_1 \frac{\partial}{\partial x}\bar{T} - v_1 \frac{\partial}{\partial y}\bar{T} - \left[\bar{u_1}\frac{\partial}{\partial x} - \bar{v_1}\frac{\partial}{\partial y}\right]T$$

$$-K_w(x,y)w_1 - K_T(x,y)h + d(x,y)T \ , \tag{2.1}$$

where

$$K_w(x,y) \equiv \delta_w \ H_1 \ \bar{T_z} \ H(\bar{w_1}) \ , \tag{2.2}$$

with H(x) the Heaviside function:

$$H(x) \equiv \begin{cases} 0, & \text{when } x < 0 \\ 1, & \text{when } x \geq 0 \ . \end{cases} \tag{2.3}$$

$$K_T(x,y) \equiv -\delta_T \frac{\Delta(\bar{w_1})}{H_m} \ \Gamma(x) \ , \tag{2.4}$$

with

$$\Gamma(x) = \left.\frac{\partial T_s}{\partial h}\right|_{h=0} \ , \tag{2.5}$$

and

$$d(x,y) = \alpha_s + \delta_T \frac{\Delta(\bar{w_1})}{H_m} \ . \tag{2.6}$$

Variables with an overbar represent background state quantities (which include an annual cycle), and unadorned variables represent anomalies calculated by the model. u_1, v_1 and w_1 are the surface layer currents, zonal, meridional and vertical respectively. T is the SST and h is the upper layer depth anomaly. $\bar{T_z}$ is the mean vertical temperature gradient at

the base of the surface layer and $T_s(h)$ the anomalous temperature there: this is a function of the thermocline depth, expressed in terms of the depth of the interface of the 1.5 layer model. We will discuss $T_s(h)$ and $\bar{T_z}$ in more detail later. δ_w and δ_T are so called efficiency factors that represent a raft of processes absent the 1.5 layer model: there is more discussion of these two terms later. Δ is defined as

$$\Delta(x) \equiv \begin{cases} 0, & \text{when } x < 0 \\ x, & \text{when } x \geq 0 \ . \end{cases} \tag{2.7}$$

α_s is the thermal damping, set to a value of 125 days^{-1}. Finally $H_m = 50m$, is the surface layer depth. See Seager et al. (1988) for more discussion of the SST equation in the ZCM, and Thompson (1998) for more discussion on the linearisation of the SST equation.

The first three terms on the right hand side of eqn. 2.1 represent horizontal advection. The next term, involving $K_w(x, y)$, represents the effect of the anomalous upwelling, w_1, of the mean temperature gradient. The penultimate term in eqn. 2.1, which involves $K_T(x, y)$, represents the effect of the mean upwelling of the anomalous temperature gradient and, finally, $d(x, y)$ is a damping term.

Background state quantities are specified in the above terms by the horizontal means previously described. Only $T_s(h)$ and $\bar{T_z}$ remain unspecified. We will now outline how each of these terms may be estimated from data and incorporated into LOAM.

2.4.1 $\bar{T_z}$, the mean temperature gradient at the base of the surface layer

Figure 2.7 shows estimates of $\bar{T_z}$ along the equator from the various ocean temperature datasets. This value is an annual mean, averaged over 4.5°N-4.5°S at the 26 points of the LOAM grid between 127-271°E. Although $\bar{T_z}$ is really a function of latitude and longitude the term is only important in determining SST anomalies right on the equator, thus Zebiak and Cane (1987) ignored meridional variations in $\bar{T_z}$ for the sake of simplicity and because

of the lack of data. In the present study we retain this simplification and use an average over 4.5°N-4.5°S that represents well the mean equatorial value.

There is broad agreement amongst the various datasets upon the size of $\bar{T}_z$ as we traverse the equator from west to east until around 220°E, where the new values greatly exceed those in originally used in LOAM.

2.4.2 $T_s(h)$

The term K_T represents the mean upwelling of anomalous temperature gradient. This anomalous temperature gradient arises from thermocline displacements, which change the temperature at the base of the surface layer, $T_s(h)$. The original parameterisation for this term was defined in Zebiak and Cane (1987) as:

$$T_s(h) = \Theta(h)\big\{tanh\big[\lambda\ (\bar{h}_{20} + \xi|h|)\big] - tanh(\lambda\bar{h}_{20})\big\}\ , \tag{2.8}$$

where, in B88M,

$$\begin{cases} \Theta = +28K \text{ and } \lambda^{-1} = 80m & \text{when } h > 0 \\ \Theta = -40K \text{ and } \lambda^{-1} = 33m & \text{when } h \leq 0\ , \end{cases} \tag{2.9}$$

$\xi = 1.5$ and $\bar{h}_{20}$ is the mean depth of the thermocline as defined by the 20 °C isotherm. h is the perturbation to the interface height calculated in the 1.5 layer ocean model used in ZCM and LOAM (this is the layer in which the thermodynamic mixed layer defined by eqn. 2.1 is embedded). In the original ZCM and B88M the values of Θ and λ were chosen on an *ad hoc* basis.

In order to fit $T_s(h)$ to data, Seager et al. (1988) devised an empirical scheme to fit model layer depth changes, h, to observed thermocline depth changes, which were defined by the 20 °C isotherm depth h_{20}, and then they fit the observed h_{20} to observed 50m temperature changes, T_{50}. Combining these two fits gives a fit of h to T_{50}. Since the base of the surface

layer is at a depth of 50m this fit is analogous to $T_s(h)$. We shall follow this procedure to calculate $T_s(h)$ from observations and then use a linearisation of the result in LOAM.

The 1.5 layer ocean model approximates the real ocean thermocline as the interface between the upper and lower model layers. The density change over the real thermocline is a continuous function, whereas in the 1.5 layer model it is a step change. Thus we would not expect that, for the same windstress forcing, h from the 1.5 layer model be the same as h_{20} in the real ocean. For this reason a mapping of thermocline depth, h_{20}, to upper layer height, h, is required. We shall call this mapping $f(h)$: $h_{20} - \bar{h}_{20} = f(h)$. Seager et al. (1988) derive this by fitting the observed annual cycle of thermocline depth, taken as the 20°C isotherm depth, to h from the 1.5 layer model forced by the annual cycle of windstress. For reasons stated in Seager et al. (1988), a quadratic fit is used. Note that the annual cycle in both h_{20} and windstress is used here, rather than anomalies about the annual cycle. An annual average value of $f(h)$ is then used in calculating $T_s(h)$.

In order to obtain $f(h)$ from the new data, we force the 1.5 layer ocean with the two different windstress climatologies, FSU and NCEP, to get the annual cycle of h. We then calculate the annual cycle of h_{20} from the three ocean temperature datasets, BOM, SODA and GODAS and fit this to the annual cycle of h. Figure 2.8 shows the scatter of points when this is done using h_{20} calculated from SODA, and h computed by forcing the linearised 1.5 layer ocean with the climatology of NCEP windstress. Other combinations of wind and temperature datasets yield very similar results. Also shown in fig. 2.8 is the resulting annual average $f(h)$.

Next the mapping of 50m temperature, T_{50}, to thermocline depth changes, h_{20}, is calculated. This is obtained by fitting the observed annual cycle of T_{50} to the observed annual cycle of h_{20} using a cubic spline with 6 tie points. We shall call this mapping $cs(h_{20})$: $T_{50} = cs(h_{20})$. Again, note that the annual cycle of T_{50} and h_{20} are used, and then an annual average value of $cs(h_{20})$ calculated.

A scatter plot of T_{50} against h_{20} is shown in fig. 2.9 for the SODA subsurface temperature

data. The annual average of $cs(h_{20})$ derived from the data is also shown by the solid line. All three temperature datasets yield qualitatively similar $cs(h_{20})$.

With the pair of $cs(h_{20})$ and $f(h)$ estimated, all that remains is to linearise them, in order that they may be used in the LOAM SST tendency equation (eqn. 2.1). Using $cs(h_{20})$ and $f(h)$ to define $T_s(h)$ we obtain

$$T_s(h) = cs(f(h)) \ . \tag{2.10}$$

Recalling that $T_s(h)$ linearises as:

$$T_s(h) \simeq \frac{\partial T_s(h)}{\partial h} \cdot h \equiv \Gamma \cdot h \ , \tag{2.11}$$

therefore

$$\Gamma = \left.\frac{\partial cs}{\partial h_{20}}\right|_{f(\bar{h})} \cdot \left.\frac{\partial f}{\partial h}\right|_{\bar{h}} . \tag{2.12}$$

Figure 2.10 shows values of Γ across the equator. Shown for comparison is the linearisation of the B88M parameterisation used in LOAM. As with the $\bar{T}_z$ parameterisation the general shape of the old and new functions are broadly similar, but the new parameterisations are larger especially in the east central Pacific. There is a spike in the function Γ derived from the BOM temperature and FSU windstress data at 260°E. This can be explained by the shape of the function $cs(h_{20})$. In eqn. 2.12 we see that Γ is a function of the gradient of $cs(h_{20})$ and as can be seen in fig. 2.9, at thermocline depths of around 50m, the gradient of $cs(h_{20})$ is at its steepest: deeper and shallower than 50m, the gradient of $cs(h_{20})$ is less. Figure 2.11 shows $\bar{h}_{20} = f(\bar{h})$, derived using values of $\bar{h}$ calculated by forcing the 1.5 layer ocean with the observed seasonal cycle of windstress. A number of combinations of temperature and windstress data sets are used. One can see in fig. 2.11 that, of all the new parameterisations, the BOM temperature and FSU windstress derived $\bar{h}_{20}$ is shallowest in

the far east. This is due to the stronger equatorial easterlies in the FSU dataset than in the NCEP dataset (see fig. 2.3). These shallower values of $\bar{h}_{20}$ in the east mean that the gradient of $cs(h_{20})$ is evaluated closer to the steepest part when using $\bar{h}_{20}$ from FSU/BOM than when using $\bar{h}_{20}$ from other datasets. Right along the eastern edge of the basin, $\bar{h}_{20}$ is so shallow that it goes beyond the steepest part of the curve and the gradient of $cs(h_{20})$ decreases. Hence the value of Γ decreases in the far eastern basin. For all other data sets the gradient of $cs(h_{20})$ is evaluated further from the steepest point, thus they do not have a spike in their Γ.

Given that $T_s(h)$ is an approximation for T_{50} from h, it would seem most simple to merely regress observed anomalies of T_{50} against h calculated by forcing the 1.5 layer model with observed windstress anomalies. However, although the various reanalysis and observational datasets span a greater time than ever before, allowing for a much more accurate computation of the climatology, the ocean temperature data still lacks either the quality or the time span for a reasonable regression using anomalies.

We have now devised functions that fit Γ and $\bar{T}_z$ to the data. Before we can calculate K_w and K_T we should notice that in both of these functions there are multipliers δ_w and δ_T. These represents processes that are unresolved in the crude 1.5 layer model. In both the ZCM and B88M, δ_w and δ_T are set equal to 0.75. Zebiak and Cane (1987) argue that as the two terms, K_w and K_T, are both evaluated at a point at the base of the surface layer, and, since SST is actually the average over the whole 50m of the surface layer, these point values of $\frac{\partial}{\partial t}T$ will be too high, hence δ_w and δ_T should be less than one. There are also unresolved surface mixing processes, present in reality, that are absent the 1.5 layer model: these are incorporated into δ_w and δ_T. In the real ocean, the mixed layer depth is not constant across the equator, thus the amount of mixing into the top 50m of the ocean is also not constant. This suggests that using one single value of δ_T and δ_w everywhere in the ocean may not be optimal. Furthermore there is no a priori reason to expect that δ_T and δ_w are the same, because K_w and K_T represent very different processes that affect

SST. Therefore using the same single value for δ_w and δ_T at all points in the ocean is not likely to be optimal. In the next section we will describe how appropriate values for these constants may be determined.

2.4.3 Estimating δ_w and δ_T

In order to establish suitable values for δ_w and δ_T, we insert the new mean fields (currents and upwelling) and their respective parameterisations of Γ and $\bar{T}_z$ into the linearised version of the ZCM ocean model that is used in LOAM. δ_w and δ_T in K_w and K_T are then set to various values between 0.1 and 1 in increments of 0.1, giving, in total, 100 different ocean models for each set of background states. In each model, δ_w and δ_T are the same for all points in latitude and longitude. Each of these 100 different ocean models is then forced by the time series of 1970-2005 NCEP windstress anomalies. These anomalies have been subjected to two passes of a three month running mean filter, in order to remove their high frequency variability. Each ocean model then computes the SST, and from this the nino3 index is calculated. Figure 2.12 shows an example Taylor diagram (Taylor, 2001) comparing the observed 1970-2005 nino3 index to the nino3 index computed by the ocean model with background states derived using SODA currents and temperature and NCEP windstress. On the Taylor diagrams each concentric ring represents a line of equal RMSE and the angle down from the vertical represents the correlation. Note that the scaling for the correlation is not linear, rather the angle varies as the squared correlation. Each of the coloured lines represents a set of models with equal δ_w. Tick marks along those lines are at intervals of 0.1 δ_T, with δ_T varying between 0.1 and 1. Thus the third tick from the end of the darkest blue line that is labelled 0.1, is an ocean model with $\delta_w = 0.1$ and $\delta_T = 0.3$. For clarity only lines of $\delta_w = 0.1, 0.2, 0.3$ are shown.

Upon examining Taylor diagrams averaging SST between 5°N-5°S at each longitudinal point, it was observed that the values of δ_w and δ_T that optimised SST locally were different at each longitudinal point; three examples are shown in fig. 2.13(a)-(c). The values of δ_w

and δ_T that optimise the SST at each longitude point were then chosen to create $\delta_w(x)$ and $\delta_T(x)$, so now δ_w and δ_T vary with longitude (fig. 2.14 shows values of δ_w and δ_T used for various data sets). When the ocean model is compiled with $\delta_w(x)$ and $\delta_T(x)$, instead of holding δ_w and δ_T constant with longitude, the fit of the modelled to the observed SST is optimised at each point along the equator. This can be seen in fig. 2.13(a)-(c), where the circles show the correlation and RMSE of the modelled SST when $\delta_w(x)$ and $\delta_T(x)$ are used. Note in fig. 2.12 that the fit to nino3 is optimised using $\delta_w(x)$ and $\delta_T(x)$ as well. $\delta_w(x)$ and $\delta_T(x)$ are constant over latitude because outside the equatorial waveguide upwelling does not play an important role in ENSO dynamics, thus it is only important to get the correct value of $\delta_w(x)$ and $\delta_T(x)$ on the equator. As we go east to west across the equator, the SST is not especially sensitive to changing δ_w however, quite different values of δ_T are optimal at each longitude point. Nowhere are the optimal values of δ_w and δ_T the same.

This procedure for choosing δ_T and δ_w is somewhat subjective, but over the east central Pacific, where the SST variability associated with ENSO is greatest, the optimal values of δ_w and δ_T are easy to choose. Furthermore, as is shown in Chapter 3, when we couple a variety of ocean models to the atmosphere, each model gives an ENSO mode that is qualitatively similar. Each of the ocean models uses a different set of Γ and $\bar{T}_z$ which yield very different K_w and K_T. Since the differences in K_w and K_T that arise from using different values of Γ and $\bar{T}_z$ are larger than the differences using the same Γ and $\bar{T}_z$ but different, yet plausible, values of δ_w and δ_T, choosing the values of δ_w and δ_T that give the best fit to the observed anomalies is not of paramount importance.

2.4.4 The Final Compilation

Now that all the terms in K_T and K_w can be calculated, we are in a position to be able to compile the ocean component of LOAM that best fits the observations. With the number of required background states and the number of different data sets available, there is a large number of possible model configurations using various different combinations of backgrounds

states and subsurface parameterisations. Rather than present and test all possible models, in the next chapter we will show just three that represent a large spread of possible K_w and K_T. A summary of the data sets used in each model is presented in Table 2.2. These three models represent the models that have K_T and K_w that lie at the extremes and middle of the distribution of possible K_T and K_w. We should, however, note that there is no reason to expect that these three ocean models should represent the largest spread of *coupled* models but it will show us how sensitive the coupled model is to the ocean parameterisations. Figures 2.15-2.17 show how the terms K_w and K_T vary for these candidate oceans and for the $LOAM$(T80). The characteristic differences between old and new estimates are that K_T and K_w are generally smaller in the new oceans than in the old, this is especially true in the far east. The maximum in K_w is shifted westward, into the central basin, in the new models compared to that in $LOAM$(T80).

2.5 Atmosphere

With the ocean independently tuned to give the best fit to the data, the atmosphere still requires validation. To do this we shall compare observed windspeed anomalies to those produced by the LOAM atmosphere component, forced by the observed SST anomalies.

The atmospheric component of LOAM, is the linear atmosphere model due to Gill (1980) that includes a linearisation of the convergence feedback that was devised by Zebiak and Cane (1987). This model is forced with the observed SST anomalies from 1970-2005 from the NCEP/OI dataset and the resulting windspeed is then calculated. The modelled and the NCEP zonal windspeed anomalies for the same period are then averaged over 10°N-10°S, 140°E-240°E, this is shown in fig. 2.18. This spatial average was chosen because it matches the region that explains most of the variance on interannual timescales in both the Gill model and the NCEP data. The two timeseries were both smoothed by two passes of a 3 month running mean filter. This removes the high frequency variance from the timeseries which, because it is not a response to the SST anomalies, we do not expect the Gill model

to be able to model. Thus these frequencies are excluded from the analysis. The regression coefficient between these two series is .56, indicating that over the equatorial waveguide the Gill atmosphere with the linearised convergence feedback tends to underestimate the zonal windspeed by a factor of .56. This is unsurprising since the Gill model winds are an average over the whole lower tropopause, rather than the surface wind. Since the windstress goes linearly with windspeed in the linearised model, to get the correct windstress anomalies to force the ocean model the windspeed from the atmosphere model needs to be multiplied by approximately $\frac{1}{.56}$. Assuming that the correct drag coefficient is $1.25 \cdot 10^{-3}$, in order to get windstress anomalies of the correct amplitude, the drag coefficient used to couple the the atmosphere and ocean in the new versions of LOAM needs to be $2.1 \cdot 10^{-3}$. This is about 80% of the value that was originally used in ZCM, which was $2.51 \cdot 10^{-3}$. We should note that the results in the next chapter are not particularly sensitive to the value of the drag coefficient used.

2.6 Summary

We have shown in this section how we can take observed climatological mean fields and incorporate them into the background states of LOAM. We have also shown how, in an uncoupled sense, we can tune the 1.5 layer ocean to give the best fit to hindcast SST anomalies when the model is forced by observed windstress anomalies. Similarly, the drag coefficient in the atmosphere is tuned to give the best fit of hindcast zonal windstress anomalies over the equatorial waveguide when the atmosphere is forced by observed SST anomalies. Now all that remains is to couple the ocean and the atmosphere models and evaluate the coupled model behaviour. The next section details what happens when this is done. We will show the stability and structure of the ENSO mode that results from the new mean states in LOAM and compare these to those observed.

Table 2.1: Values of constants used in all $LOAM$(T80) and $LOAM$(a)-$LOAM$(c). See text or Thompson (1998) for more explanation of these parameters and Table 2.2 for a list of the mean fields that comprise $LOAM$(a), $LOAM$(b) and $LOAM$(c).

Symbol	Value	Parameter
A	$1.576 \cdot 10^{-5} s^{-1}$	Atmospheric Damping
β	$2.2915 \cdot 10^{-11} m^{-1} s^{-1}$	Meridional gradient of Coriolis force
c_a, c_o	$60, 2.9 m s^{-1}$	Gravity wave speed in atmosphere, ocean
γ	$1.4 m K^{-1} s^{-1}$	Coupling coefficient
T_{ref}, b	$303K, 5400K$	Reference temperatures
$\delta_{Kw,Kt}$	see chap. 2	Ocean efficiency factors
H_0	$150m$	Mean upper layer depth
g'	$5.6cm$	Reduced gravity
a^{-1}	$8.7\ month^{-1}$	Ocean damping
ρ_a, ρ_o	$1.275, 1.026 \cdot 10^{-3} kg m^{-3}$	Density of the atmosphere, ocean
c_d	see chap. 2	Drag coefficient
H_1, H_2	$50, 100m$	Depth of surface, subsurface layer
r_s^{-1}	$2days$	Surface layer damping
WBR	0.7	Western boundary reflection

Table 2.2: Summary table of the background state fields used in the three example models.

	Data sets used			
Model name	SST	Currents	Subsurface parameterisation	Windstress
$LOAM$(T80)	RC	derived from the 1.5 layer ocean forced with RC winds		RC
$LOAM$(a)	SODA	SODA	SODA	NCEP
$LOAM$(b)	NCEP	GODAS	BOM	FSU
$LOAM$(c)	NCEP	GODAS	BOM	NCEP

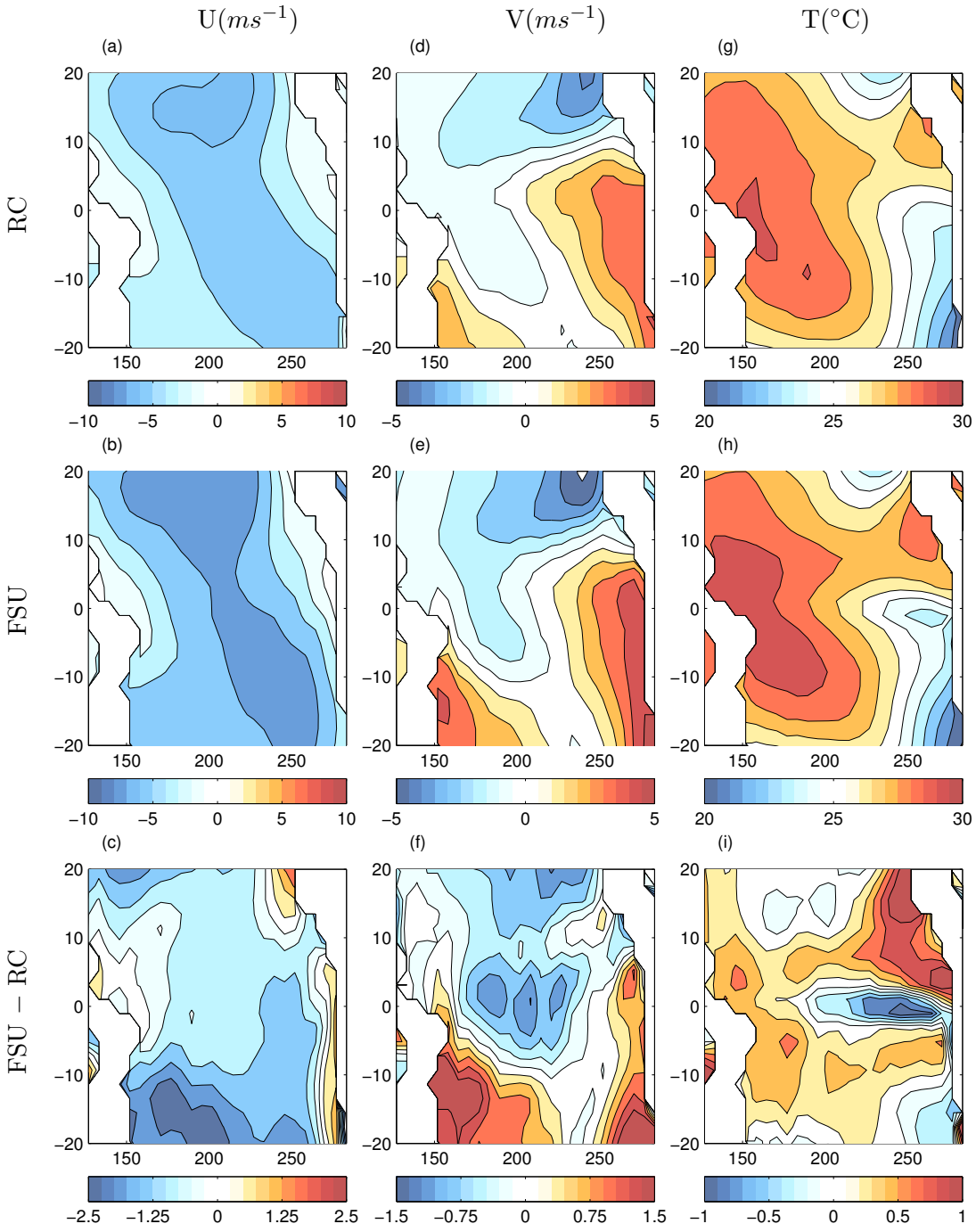

Figure 2.1: Annual mean winds and SST. Annual mean zonal (a) and meridional (d) winds in RC. Annual mean zonal (b) and meridional (e) winds in FSU. The difference, FSU-RC, for zonal, (c), and meridional winds, (f). SST from RC in (g), SODA in (h) and the difference in (i). The fields are those that are entered into LOAM.

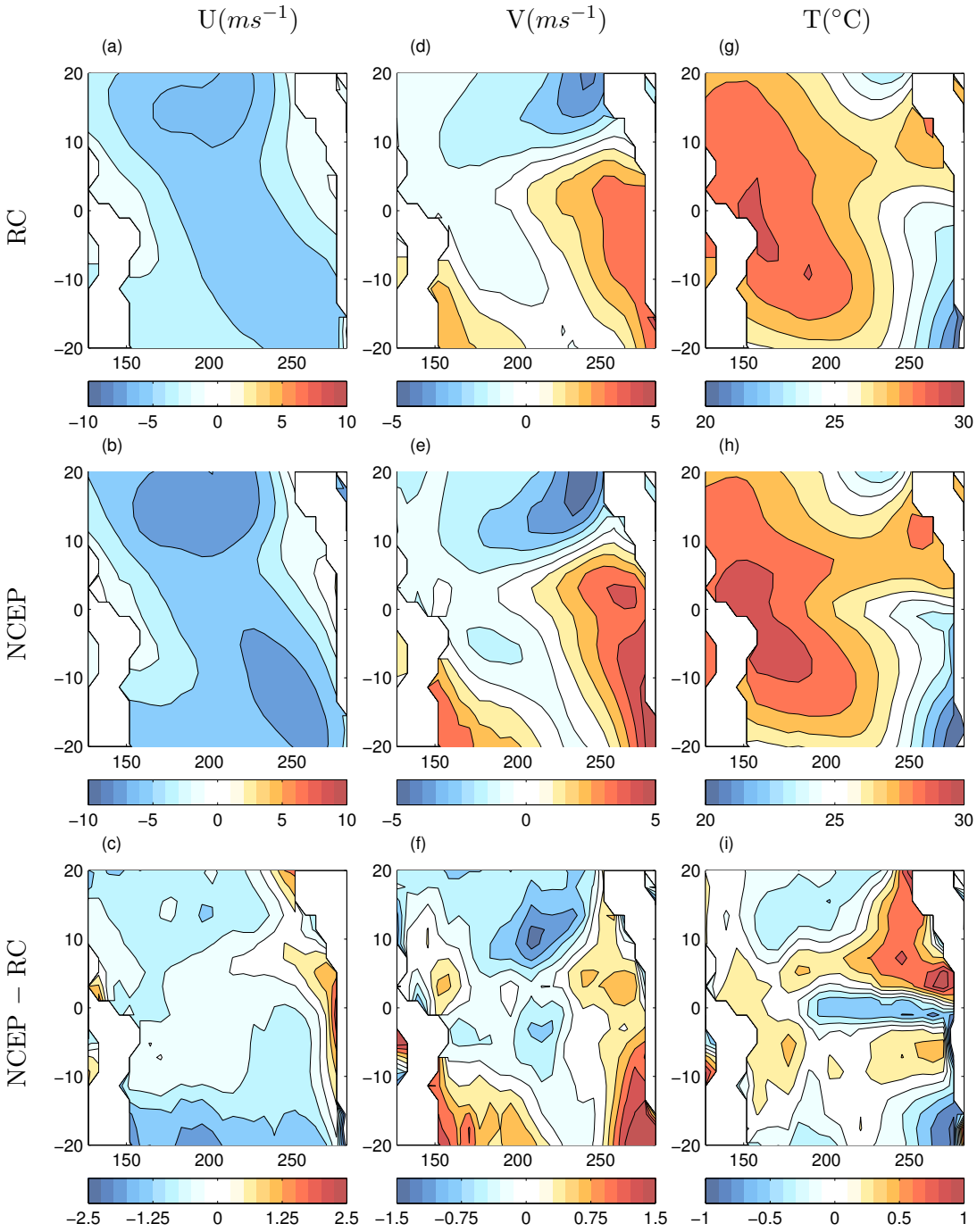

Figure 2.2: Annual mean winds and SST. Annual mean zonal (a) and meridional (d) winds in RC. Annual mean zonal (b) and meridional (e) winds in NCEP. The difference, NCEP-RC, for zonal, (c), and meridional winds, (f). SST from RC in (g), SODA (h) and the difference in (i). The fields are those that are entered into LOAM.

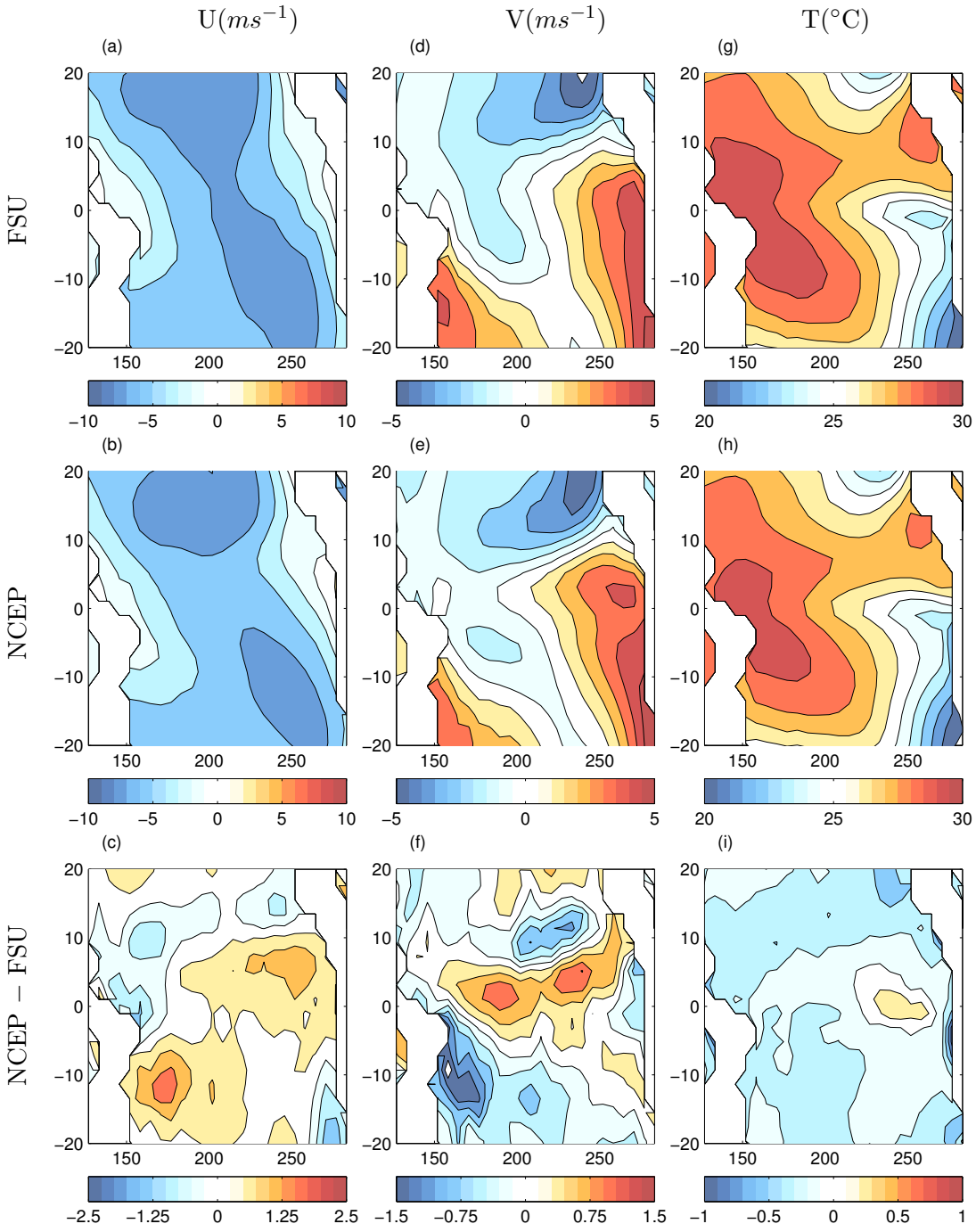

Figure 2.3: Annual mean winds and SST. Annual mean zonal (a) and meridional (d) winds in FSU. Annual mean zonal (b) and meridional (e) winds in NCEP. The difference, NCEP-FSU, for zonal, (c), and meridional winds, (f). SST from SODA in (g), NCEP in (h) and the difference in (i). The fields are those that are entered into LOAM.

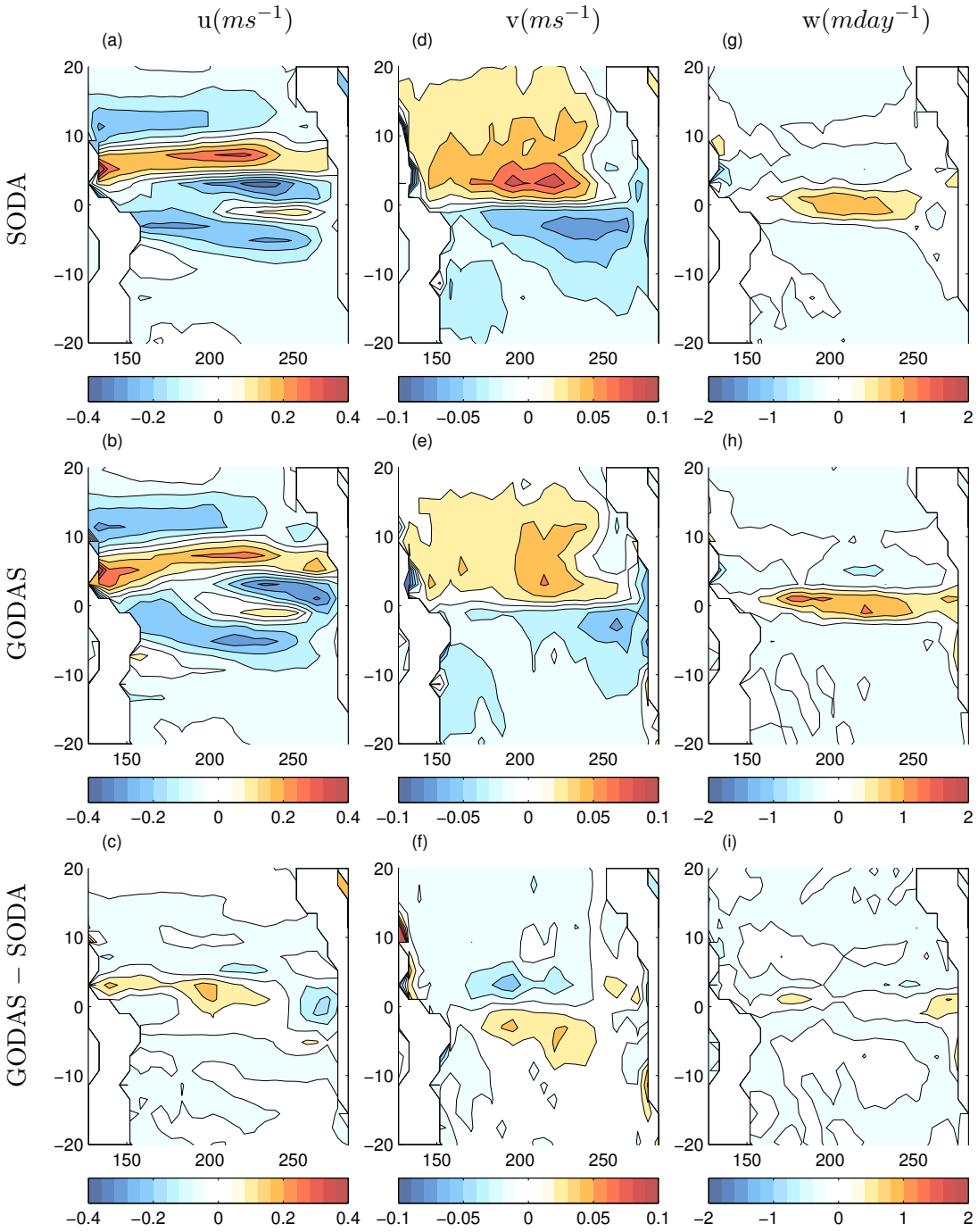

Figure 2.4: Annual mean surface currents from SODA and GODAS. Zonal currents from SODA in (a), GODAS in (b), and the difference GODAS-SODA in (c). Meridional currents from SODA in (d), GODAS in (e), and the difference GODAS-SODA in (f). Upwellling from SODA in (g), GODAS in (h), and the difference GODAS-SODA in (i). The fields are those that are entered into LOAM.

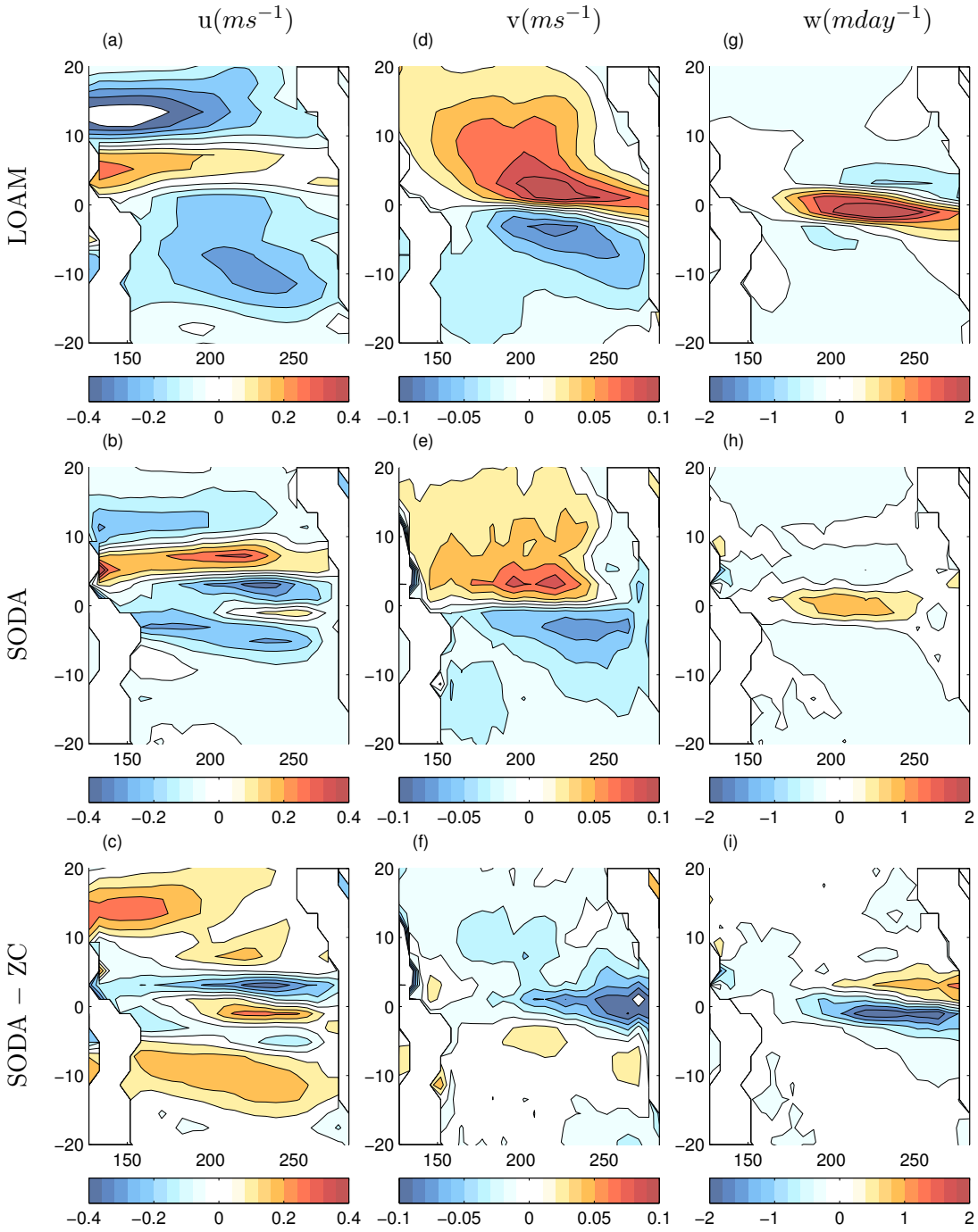

Figure 2.5: Annual mean surface currents from SODA and ZC. Zonal currents from ZC in (a), SODA in (b), and the difference SODA-ZC in (c). Meridional currents from ZC in (d), SODA in (e), and the difference SODA-ZC in (f). Upwellling from ZC in (g), SODA in (h), and the difference SODA-ZC in (i). The fields are those that are entered into LOAM.

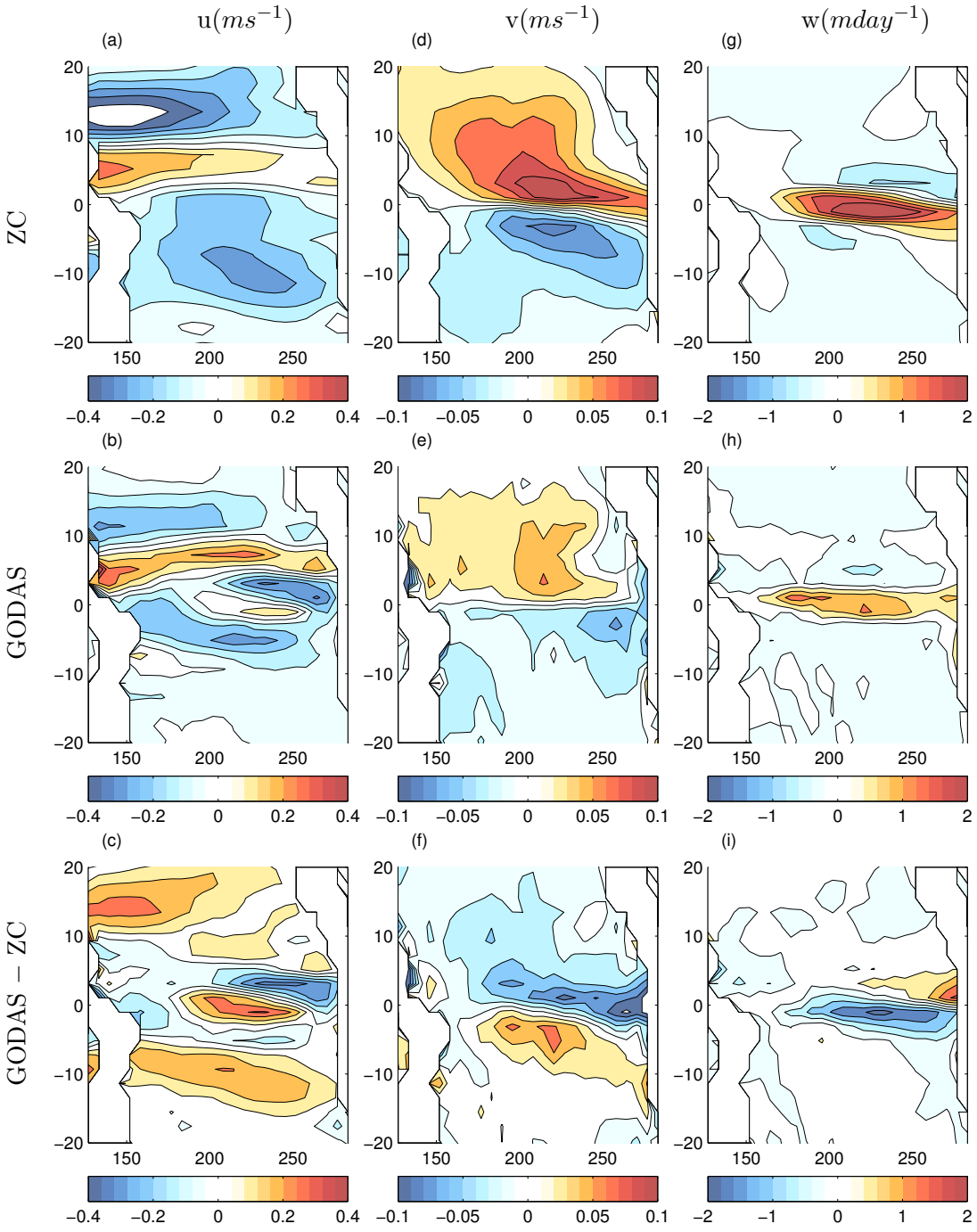

Figure 2.6: Annual mean surface currents from ZC and GODAS. Zonal currents from ZC in (a), GODAS in (b), and the difference GODAS-ZC in (c). Meridional currents from ZC in (d), GODAS in (e), and the difference GODAS-ZC in (f). Upwellling from ZC in (g), GODAS in (h), and the difference GODAS-ZC in (i). The fields are those that are entered into LOAM.

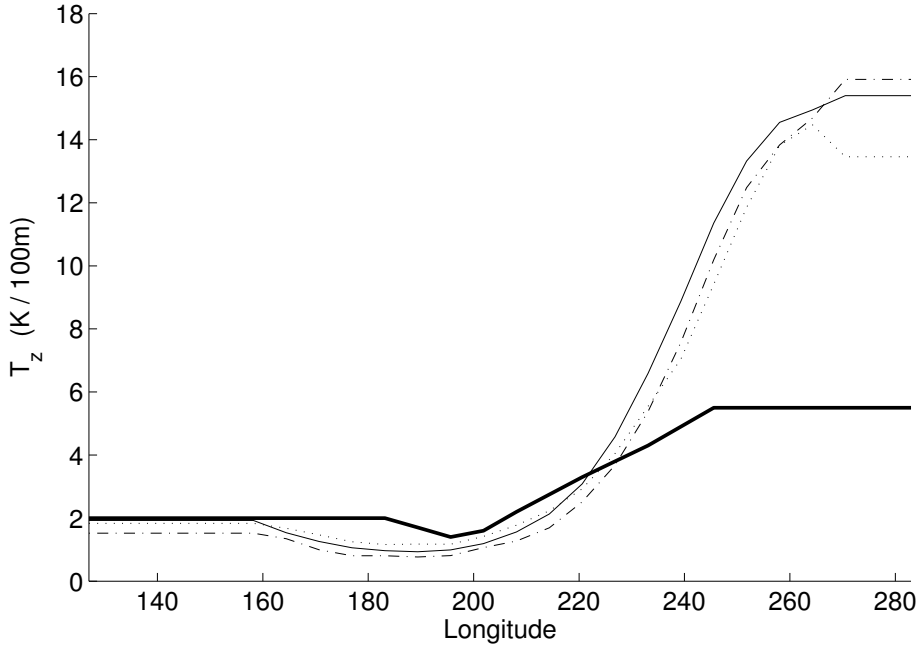

Figure 2.7: $\bar{T}_z$. Bold solid line the ZC original, solid from BOM data, dotted from SODA, dash-dotted from GODAS.

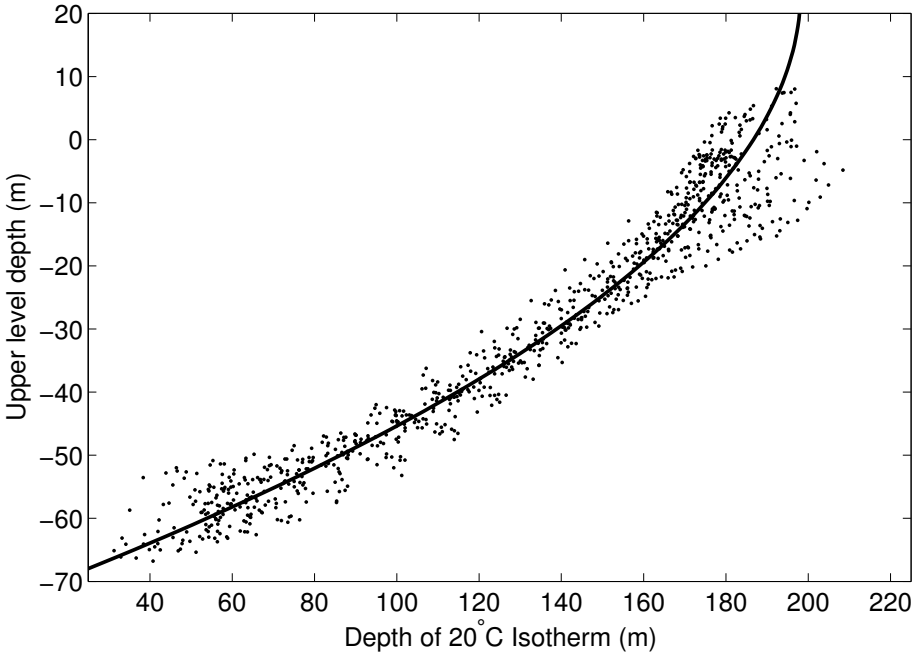

Figure 2.8: Scatter plot of upper level height anomalies, h, against the observed 20°C isotherm depth, h_{20} from SODA. The quadratic fit, $f(h)$, is also plotted.

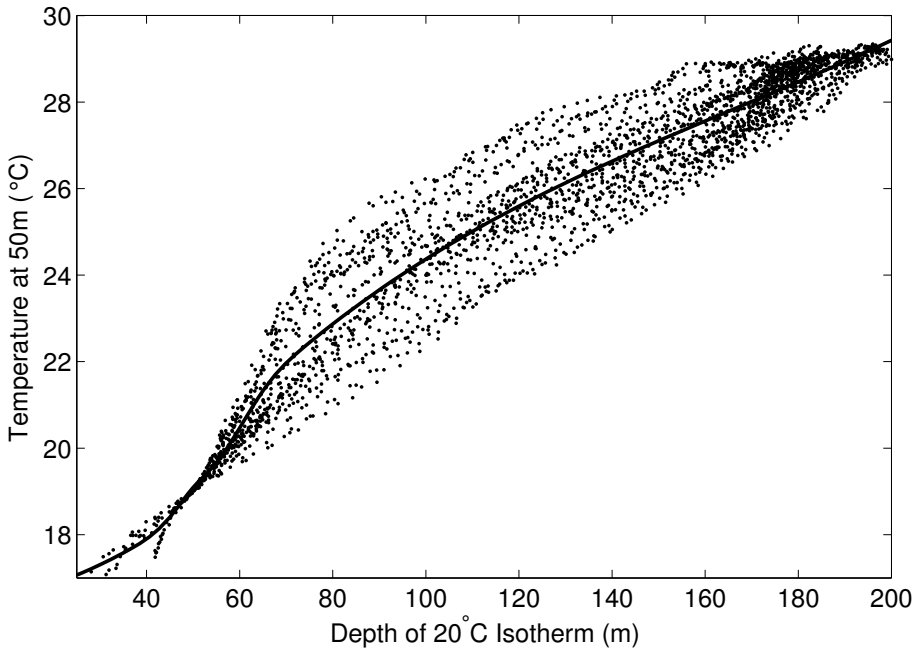

Figure 2.9: Scatter plot of observed 50m temperature,T_{50}, against the 20 °C isotherm depth, h_{20}, for the SODA. The cubic-spline curve fit, $cs(h_{20})$ is also shown.

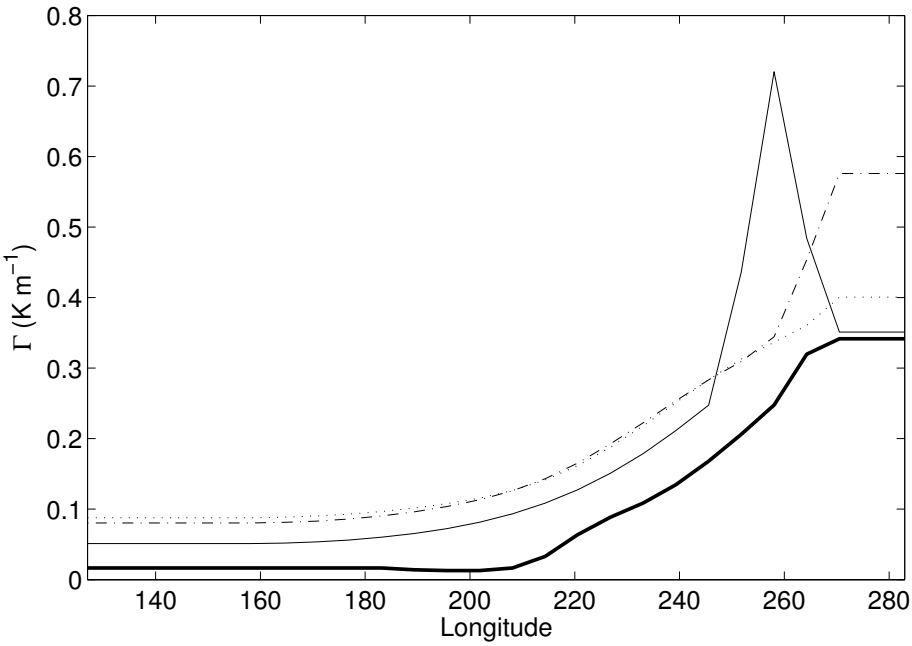

Figure 2.10: $\Gamma(x)$ derived using: BOM subsurface temperature with FSU windstress, solid, and with NCEP windstress, dash-dotted; dotted line is for the SODA subsurface data forced with NCEP wind anomalies. The bold solid line shows the linearisation of the B88 parameterisation.

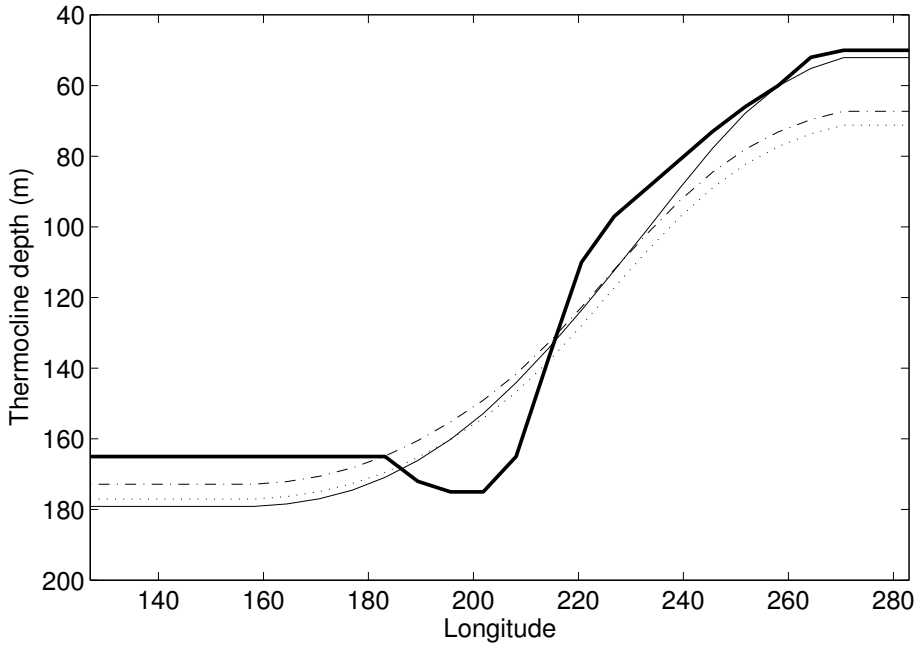

Figure 2.11: Mean thermocline depth, $\bar{h}_{20}$, derived using $f(h)$ and $\bar{h}$ from: the BOM subsurface temperature with FSU windstress, solid line; the BOM subsurface temperature with NCEP windstress, dash-dotted line; and the SODA subsurface data forced with NCEP wind anomalies, dotted line. Bold solid shows the ZC original.

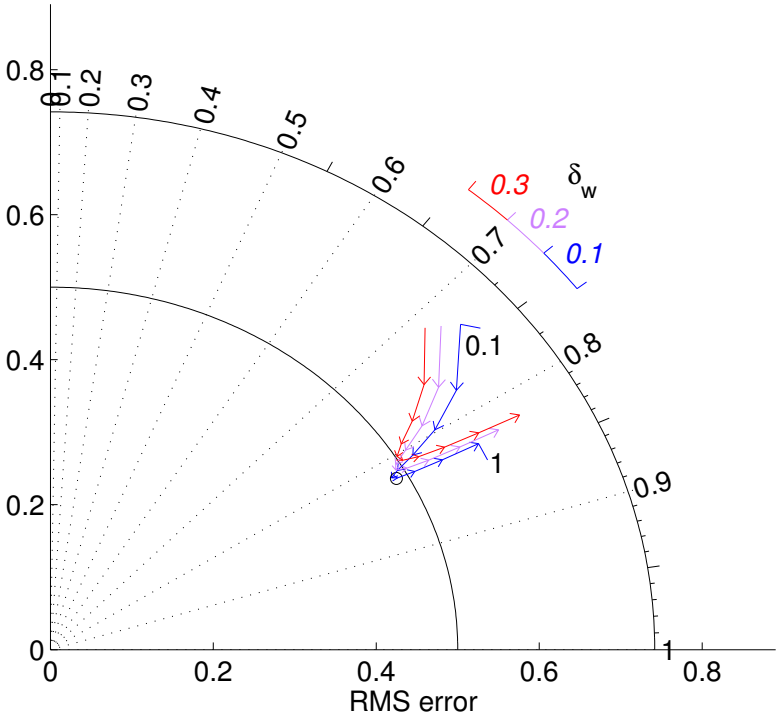

Figure 2.12: Taylor Diagram for tuning the ocean model based on the SODA subsurface parameterisation forced with NCEP windstress anomalies. The fit is between the observed and modelled nino3 index. See text for explanation of Taylor Diagram. The circle represents the model using $\delta_w(x)$ and $\delta_T(x)$.

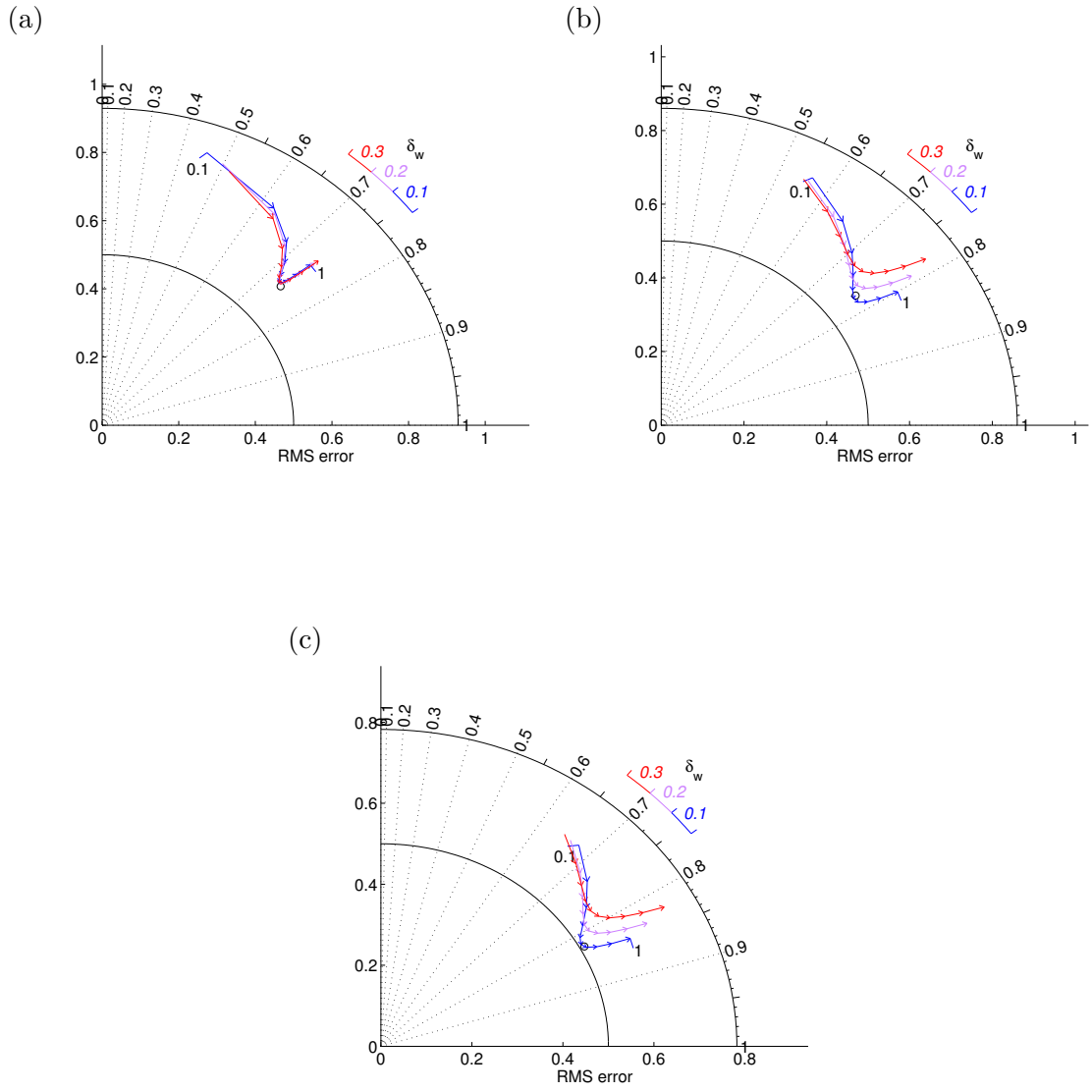

Figure 2.13: Taylor Diagrams for tuning the ocean model based on the SODA subsurface parameterisation forced with NCEP windstress anomalies. See text for explanation of Taylor Diagram. The circle in each panel represents the model using $\delta_w(x)$ and $\delta_T(x)$. Each plot is an average of SST between 5°N-5°S at (a) 260°E, (b) 240°E, (c) 230°E

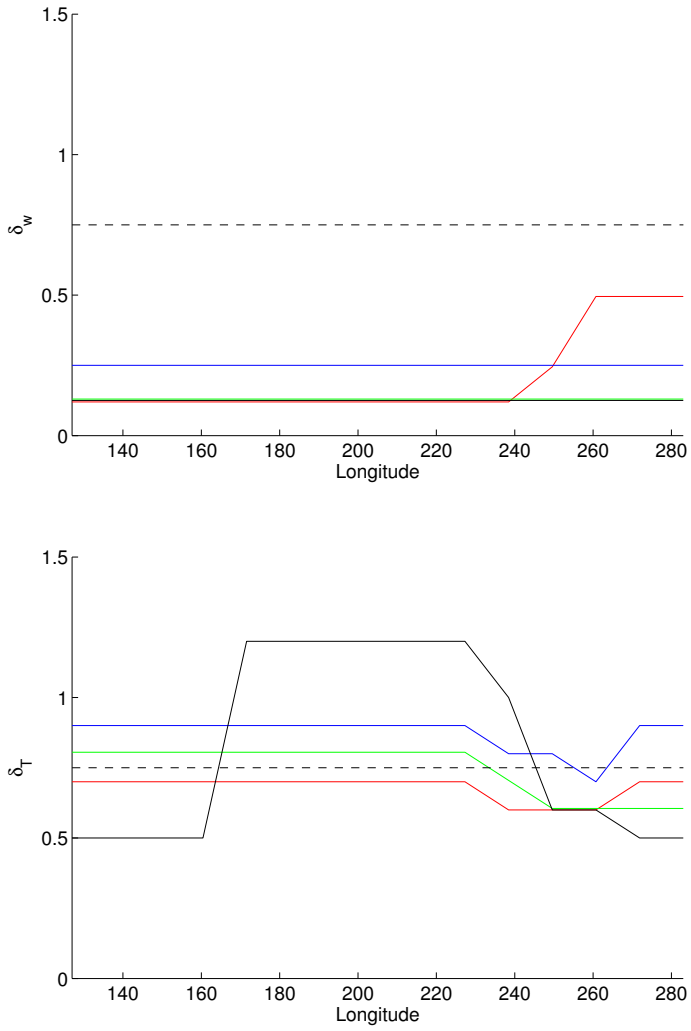

Figure 2.14: δ_w (top), and δ_T (bottom), using ocean background states for $LOAM$(a)(red), $LOAM$(b)(blue), $LOAM$(c)(green). The original uniform value of 0.75 used in the ZCM is shown in the dashed black line. Also shown are the optimal values of δ_w and δ_T when the ocean model using the original ZCM background states and subsurface parameterisations is tuned to give the best hindcast of SST (solid black line). See Table 2.2 for mean states used in $LOAM$(a)-(c)

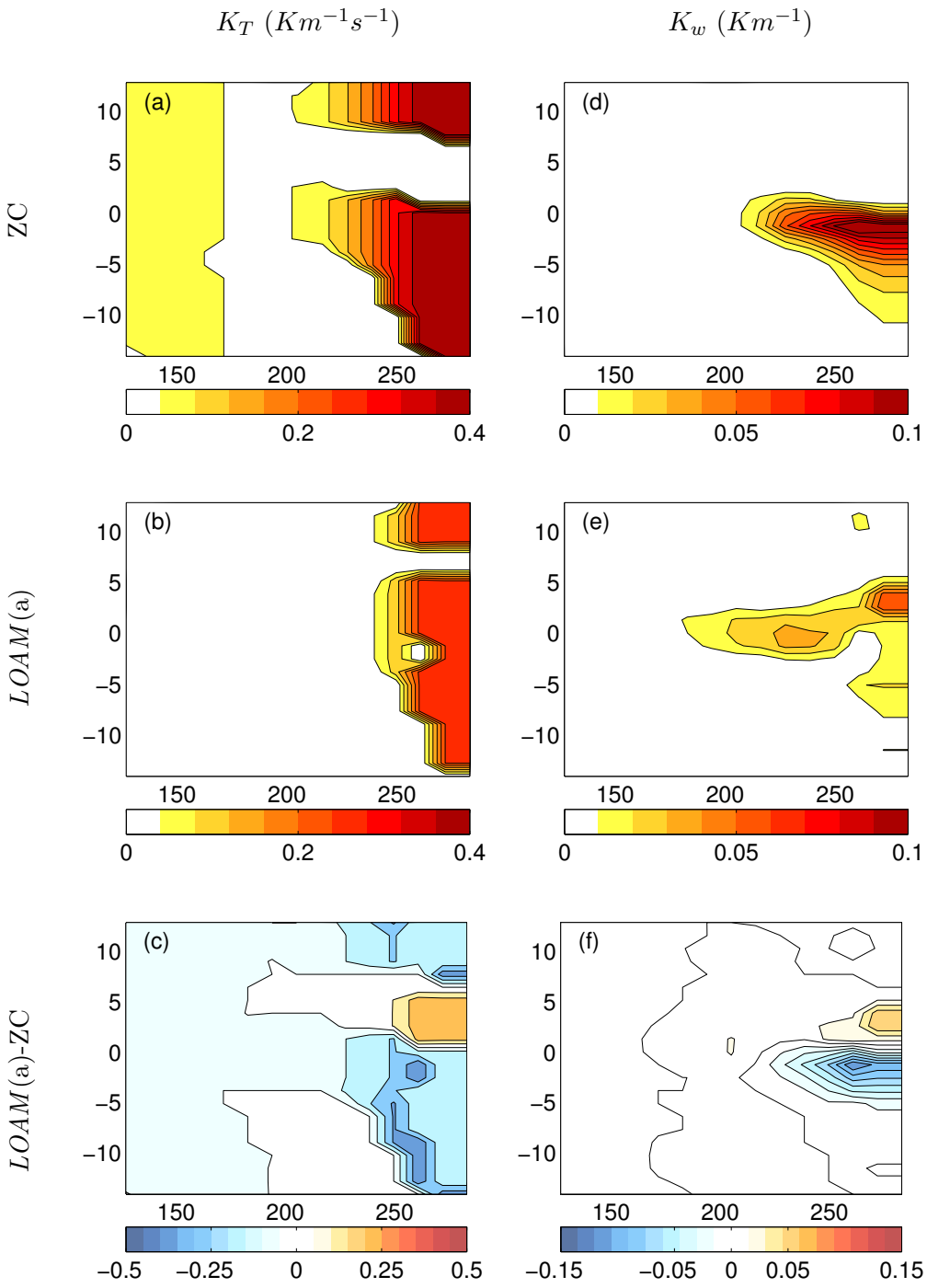

Figure 2.15: Maps of the functions K_w and K_T for the original ZC parameterisation and the new parameterisation $LOAM$(a). (a) K_w for ZC model, (b) K_w for $LOAM$(a), (c) Difference in K_w, $LOAM$(a) - ZC , (d) K_T for ZC model, (e) K_T for $LOAM$(a), (f) Difference in K_T, $LOAM$(a) - ZC.

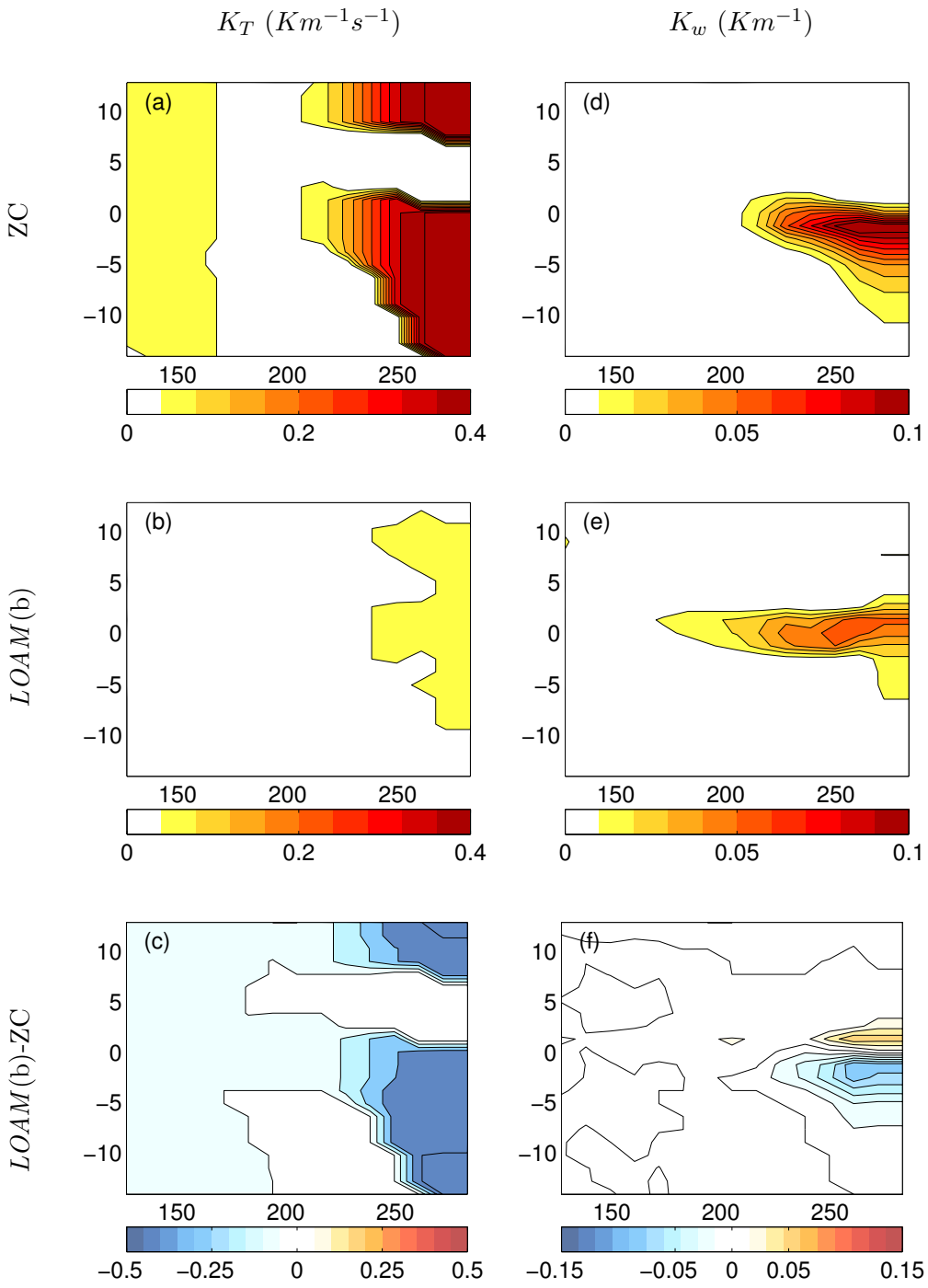

Figure 2.16: Maps of the functions K_w and K_T for the original ZC parameterisation and the new parameterisation $LOAM$(b). (a) K_w for ZC model, (b) K_w for $LOAM$(b), (c) Difference in K_w, $LOAM$(b) - ZC , (d) K_T for ZC model, (e) K_T for $LOAM$(b), (f) Difference in K_T, $LOAM$(b) - ZC.

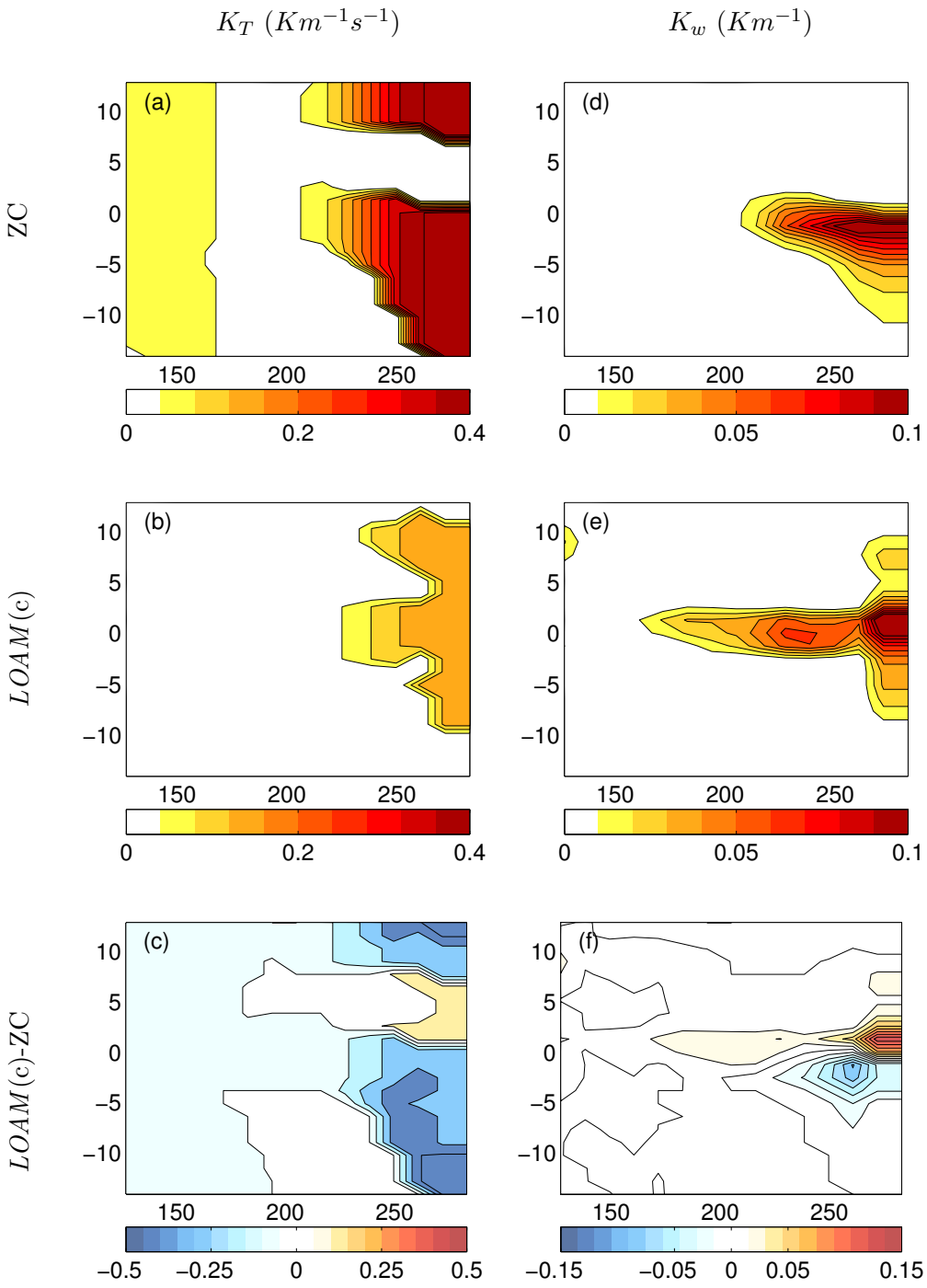

Figure 2.17: Maps of the functions K_w and K_T for the original ZC parameterisation and the new parameterisation $LOAM$(c). (a) K_w for ZC model, (b) K_w for $LOAM$(c), (c) Difference in K_w, $LOAM$(c) - ZC , (d) K_T for ZC model, (e) K_T for $LOAM$(c), (f) Difference in K_T, $LOAM$(c) - ZC.

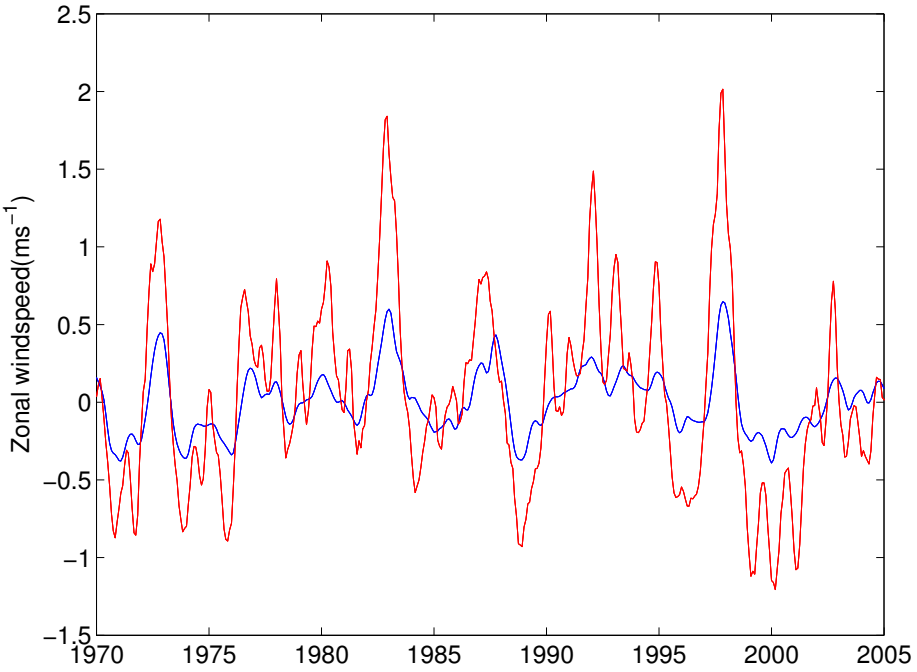

Figure 2.18: The zonal wind speed anomalies averaged over 10°N-10°S, 140°E-240°E, for, NCEP/OI, red line, and for the Gill atmosphere with a linearised convergence feedback forced with NCEP SST anomalies in the blue line.

Chapter 3

New Background State Performance

3.1 Introduction

In this chapter we will show how well the the Linear Ocean Atmosphere Model (LOAM)[1], models the interannual variability due to El Niño-Southern Oscillation (ENSO) when the background states calculated in Chapter 2 are used in the model. As was noted in Chapter 2, the original formulation of the ZCM contains a linearly unstable ENSO mode: hence non-linear processes are important for keeping the amplitude of the mode in check and also for giving the irregularity that is seen in the model output (Mantua and Battisti, 1995). The assumption underlying LOAM is that the dynamics of the couple atmosphere-ocean system in the tropical are due to linear physics. As was shown in the preceding chapter the newly derived background states are significantly different to those used in ZCM and B88M. In this chapter we shall show that LOAM with these new background states supports ENSO as the leading mode of the coupled system and it is stable. Given that the two model components of LOAM have been independently tuned in order to give as accurate a representation of the real ocean and atmosphere as possible, with no assumptions as to the underlying stability of the coupled system, it is reasonable to assume that the stability of the resulting coupled system is close to the stability of the system in nature.

We will begin by describing some of the robust observational features of ENSO. We shall then describe, briefly, how well B88M and *LOAM*(T80), model ENSO. We will finally describe how well LOAM performs with the new background states calculated in Chapter 2.

[1]LOAM is a linearisation of the Battisti (1988, B88M) version of the Zebiak and Cane model (Zebiak and Cane, 1987, ZCM), as modified by Thompson and Battisti (2000)

3.2 Observations

The spatial pattern in the sea surface temperature (SST) that we associate with ENSO is best shown by the first empirical orthogonal functions (EOFs) of the monthly mean SST anomalies in the tropical Pacific. The first EOF is shown in fig. 3.1(a) for the Kaplan SST dataset (Kaplan et al., 1998) [2], and in fig. 3.2(a), for the NCEP/OI data. The SST anomalies have a 3 month running mean filter applied in order to remove the high frequency variability, this procedure is applied to all SST data sets discussed in this chapter. The first EOF explains 30-40 % of the variance in the tropical Pacific (defined as 150°E-280°E, 30°S-30°N) SST anomalies. The second EOF, shown in figs. 3.1(b) and 3.2(b), explains much less of the variance - only 10%, but it is still distinct from higher order EOFs. Whilst EOF 1 is a general warming or cooling of the whole Pacific basin, with the peak in the pattern being located in the east central Pacific, EOF 2 is more of a seesaw pattern along the equator, although there are also significant off equatorial lobes in the pattern.

Temporally, the SST anomalies due to ENSO are best described by averaging the SST over a predefined area such as 5°N-5°S, 210°E-270°E: this gives the nino3 index. Power spectral estimates of the nino3 time series are shown in figs. 3.3 and 3.4 for the Kaplan and NCEP/OI SST respectively. In computing these spectra, and all subsequent spectra shown, a 3 month running mean is applied to nino3 in order to remove high frequency variability. We see that there is a broad peak in the spectral power at periods of around 3-7 years.

The black lines in fig. 3.5 show how the observed variance in nino3 varies through the calendar year. The variance of nino3 for each month is normalised by the total variance of the nino3 index. The peak in the monthly variance is around October to December with a broad minimum extending from April to July. This shows that ENSO activity tends to peak at the end of the calendar year, just after the climatological cold tongue tends to be

[2]NCEP/OI V2 and Kaplan SST V2 data provided by the NOAA/OAR/ESRL PSD, Boulder, Colorado, USA, from their Web site at http://www.cdc.noaa.gov/

at its strongest.

The final robust feature that we see from the observations is that nino3 anomalies are approximately normally distributed (see also Penland and Sardeshmukh, 1995, for more discussion). This is shown by the black lines in the probability density functions of nino3 shown in fig. 3.6. We should note, however, that there is a slight skewness in the distribution, for example in the Kaplan nino3 the skewness = 0.8. Penland and Sardeshmukh (1995) discuss that this skewness is predominantly due to the fact that the magnitude of the warmest warm anomalies is larger than coldest cold anomalies. They show that when the largest warm anomalies are excluded from the distribution, the fit of nino3 anomalies to Gaussian is much closer. Because a system that is governed by stochastically driven linear dynamics will have variables that are normally distributed. Penland and Sardeshmukh (1995) suggest that the dynamics underlying ENSO are linear. Furthermore, as was discussed in Thompson and Battisti (2001) the dynamics that are most important in governing the evolution of ENSO in B88M are linear. Although there are nonlinear processes that do play a lesser role, Thompson and Battisti (2001) show that the nonlinear processes become most important during extreme warm events, the occasions when Penland and Sardeshmukh (1995) suggest that the observed SST is furthest from a Gaussian distribution. This suggests that the assumption that the dynamics of ENSO are linear is valid, except for during extreme warm events.

3.3 ENSO Modes in Observations and Models

Assuming that the dynamics determining the tropical Pacific SST are linear allows one to model the system using linear inverse techniques. Penland and Sardeshmukh (1995) used tropical Indo-Pacific SST data to derive a linear inverse model, and then decompose this model into its eigenmodes. They found that the eigenmode of this linear model that most closely resembles the ENSO cycle has a period of 46 months and a decay rate of 0.22 year^{-1}. Using a similar technique, but different SST data sets, Johnson (1999) found that for the

COADS SST the period of the mode that most resembled ENSO was 4.1 years and the decay rate 0.53 year^{-1}, and for the NCEP/OI SST the period was 3.8 years and the decay rate 0.63 year^{-1}. These results are summarised in Table 3.1. Shown in fig. 3.7 is the SST pattern of the ENSO mode as derived by Penland and Sardeshmukh (1995). Over the course of one mode cycle, which is a period of 3.8 years, the mode evolves from pattern $b \rightarrow a \rightarrow -b \rightarrow -a$. This pattern agrees with the composite view of an ENSO event as shown by Rasmusson and Carpenter (1982). Qualitatively similar patterns are shown in Johnson (1999).

Just as one can decompose a linear inverse model into its eigenmodes, so one can decompose LOAM into its eigenmodes: its Floquet modes. LOAM may be run with a variety of parameters and background states. When the parameter set due to Battisti (1988) and the original ZCM background states is used the resulting model shall be called $LOAM$(B88). In Thompson and Battisti (2000) a new set of parameters which more accurately represent their values in the real ocean were derived: this model, $LOAM$(T80), which also uses the ZCM background states, was discussed in the preceding chapter. Taking $LOAM$(T80), and decomposing the annual average propagator matrix into its Floquet modes, Thompson and Battisti (2000) find that the least damped mode has the pattern shown in fig. 3.8. A very similar pattern results when $LOAM$(B88) is decomposed into its Floquet modes. This pattern is also qualitatively similar to the SST pattern derived by Penland and Sardeshmukh (1995), shown in fig. 3.7, but it is more constrained to the eastern edge of the basin. The modal period for $LOAM$(B88) is 2.8 years and the mode grows by 1.82 year^{-1}. The modal period and decay rate of the ENSO mode in $LOAM$(T80) are 3.8 years and 0.8 year^{-1}, respectively. This mode is damped, but much less damped than any of the estimates from data shown in Table 3.1. Because of its strong resemblance to ENSO, the least damped Floquet mode of LOAM is called the ENSO mode. As we will show, the leading mode of LOAM with the newly calculated background states also shows very similar spatial and temporal structures to those associated with the observed canonical ENSO. We will also

show that the ENSO mode using these background states is stable.

The mode statistics of the ENSO modes of LOAM using the new background states, described in Table 2.2, are summarised in Table 3.1. The decay rates of the new models, which lie between 0.34 and 0.53 year^{-1} are all within the range of estimates deduced from the linear inverse models by Penland and Sardeshmukh (1995) and Johnson (1999). The periods of the ENSO mode in the new models, which range from 3.7 to 4.9 years, are also close to the estimates from the empirical models of between 3.8 and 4.1 years. The spatial pattern of the ENSO modes from the new models are all very similar: an example using the model $LOAM$(a) is shown in fig. 3.9. This mode is similar to the mode from T80 and the observations, although it is not as constrained to the eastern edge of the basin as is the T80 ENSO mode.

Thus we conclude that LOAM with the new background states shows ENSO is the leading Floquet mode of the coupled ocean-atmosphere system and that the mode qualitatively resembles that in the observations. Furthermore the new estimates of the background state using the most up to date observatoins all show that the ENSO mode is stable.

3.4 The Time Evolution of ENSO in Simple Models

As was described in the introductory chapter there has been a steady evolution of the ZCM from its birth. In this section we shall describe how well two versions of the model perform at simulating the observed interannual SST variability: the Battisti version, (Battisti, 1988, B88M) and T80 parameter set used in the linearised model (Thompson and Battisti, 2000), $LOAM$(T80).

Since the ENSO mode in $LOAM$(T80) is stable, it must be externally forced in order to support ENSO variability. In nature the ultimate source of this noise is uncoupled windstress variability that creates random SST perturbations via surface flux anomalies: Thompson and Battisti (2000) took this forcing as a white noise perturbation applied to the SST field. The SST noise is normally distributed about the equator, with a peak standard deviation

of around 0.2°C. The exact amplitude of the noise is chosen to give a nino3 index that has the same variance as the observations.

Both LOAM and B88M contain interannual variability that broadly resembles the observations. Figure 3.10 shows the first two EOFs of SST anomalies from B88M. The first EOF explains 92% of the variance in SST and the second a meagre 4%. EOF 1 of B88M contains far more variance than the observations. The pattern in EOF 1 is very similar to the observations in that there is a broad warming over the whole tropical Pacific, although its peak is farther to the east than is observed. The second EOF does not capture any of the off-equatorial features in the observations [3] In fig. 3.11 the power spectrum of the B88M nino3 index is plotted as the red line. This spectrum is far more peaked at a period of around 4 years than the observations, which are shown in the grey line. This is not surprising since the model has a very regular ENSO cycle with a period of about 4 years. We see, in the red dashed line in fig. 3.5, that there is a seasonal cycle to the variance of nino3 in B88M; however, the amplitude of this cycle is not as large as observed, nor is there the observed broad minimum in the variance. The probability density function of nino3 anomalies, as shown by the red dashed line in fig. 3.6, shows a bimodal distribution (due to the unstable ENSO mode in B88M) that does not agree with the near Gaussian distribution of the observations. The spatial and temporal behaviour of the original ZCM shows very similar features to the B88M.

When $LOAM$(T80) is run with stochastic forcing, necessary to excite the damped linear mode, it produces EOFs as shown in fig. 3.12. The pattern is broadly similar to the B88M. The first EOF explains 83% of the variance and the second 3.5%. As with B88M, the first EOF of LOAM contains more variance than observed and the spatial pattern of the second EOF also fails to capture any of the observed features. The spectrum of nino3, shown in

[3]ZCM is not able to capture any of the off-equatorial variance seen in the second EOF because the model does not include the surface flux anomalies that are due to anomalies in the windspeed, which drive these off equatorial bands of SST anomalies.

fig. 3.13, is less peaked than B88M but still more peaked than the observations which are shown by the grey line. The peak period of around 4 years is very close to the period of the ENSO mode in LOAM. The seasonality of nino3 in T80, as shown by the solid red line in fig. 3.5, is a better fit to the observations than B88M: the amplitude of the seasonal cycle is closer to the observed than B88M; however, the minimum variance occurs later in the year than in either observations or in B88M. The probability density function of nino3 for T80, as shown by the solid red line in fig. 3.6, is very close to Gaussian. Since the model is a stochastically forced linear system, we expect the distribution to be Gaussian, the reason that it is not exactly Gaussian is that the series of nino3 is only short, 100 year sample.

We have shown that two versions of ZCM using the original mean states produce reasonable looking interannual SST variability. As was shown in the previous chapter the original background states contain gross errors especially in the prescribed annual cycle of currents and upwelling. Furthermore the subsurface parameterisations are also significantly different in the new models. In the next section we will show how the interannual variability in LOAM changes when we use the background states derived from the best data currently available, as calculated in the previous chapter.

3.5 LOAM with New Mean States

Having calculated the new background states in the previous chapter it now remains to try them in LOAM. All constants and parameterisations that have not been so far discussed are set to the values for the T80 model summarised in Table 2.1. The background states of the three candidate models used in this section are summarised in Table 2.2. As with $LOAM$(T80), the three candidate models were all forced with white noise applied to the SST field. The peak standard deviation of the applied noise varies between 0.33°C and 0.5°C; this gives a nino3 index that has the same variance as that observed. Table 3.1 summarises how much of the variance the first two EOFs of the three model runs explain. It also summarises the characteristics of the ENSO mode in the new models.

Table 3.1 shows that the ENSO modes in the new models are all more damped than $LOAM$(T80). The fact that the modes are more damped partly explains why the amplitude of the noise needs to be larger in the new runs than in $LOAM$(T80) if we wish to get the observed variance in nino3. $LOAM$(T80) requires noise with a maximum standard deviation of 0.18°C, the new runs use much higher values as summarised in Table 3.1. We should note, however, that as the coupled system is non-normal it is not guaranteed that the amplitude of the noise needed to get the same variance in nino3 is larger for a less dampedENSO mode, as both transient and modal growth are important in a non-normal system.

We can see that using the new models the first EOFs all explain a fraction of the variance of between 50-33% which is closer to the observed 40% than either $LOAM$(T80) or B88M; as can be seen in figs. 3.14-3.16, the spatial pattern of the first EOFs in all the models more closely resemble the observations, shown in figs. 3.1 and 3.2, than do either $LOAM$(T80) or B88M which are shown in figs. 3.10 and 3.12. The peak of the first EOF in all the new models is in the central east Pacific rather than in the far east, where B88M and $LOAM$(T80) put it. This may be explained by the shift in the spatial distribution of K_w and K_T from the old to new parameterisations. As can be seen in figs. 2.15-2.17, the amplitude of both K_w and K_T is smaller in the far east in the new formulations than the old. This makes the ocean less sensitive to h and w_1 anomalies there and thus shifts the peak in variance farther west. The first EOF, however, is more confined to the equator than either the observations or the old models. EOF 2 is much more similar to the observations, it shows the distinctive see-saw pattern seen in the observations, but absent either B88M or T80. The models do not, and indeed can not, capture the off equatorial parts of the observed second EOF as the heat fluxes that cause these patterns in nature are due to anomalies in the windspeed, which are not included in LOAM.

Power spectra for the nino3 from the new models are shown in figs. 3.17-3.18. All are realistic with broad peaks in the spectra in the 3-7 year period band. These peaks are far more spread out than either those in $LOAM$(T80) or B88M. This is most likely due

to the fact that the ENSO mode in all of the new models is more highly damped than in *LOAM*(T80). The less damped the ENSO mode, the more its frequency will tend to dominate the nino3 spectrum, although this is not guaranteed as the system is non-normal.

The seasonal variance of nino3, shown in fig. 3.5 by the blue lines, peaks at the end of the calendar year. However the minimum variance occurs two months later than is observed and also one month later than both *LOAM*(T80) and B88M. The amplitude of the seasonal cycle in the new models is also somewhat larger than in the observations. The probability density functions of nino3, which are shown by the blue lines in fig. 3.6, are of course Gaussian.

3.6 Conclusions

Evidently the new means and parameterisations work in LOAM to produce ENSO modes that are consistent with the observed ENSO mode and, when the models are stochastically forced, they produce interannual variability that is close to that observed. It could even be argued that they allow LOAM to more accurately model the observed variability as both the spatial and temporal characteristics of the new models more closely match the observed than do either *LOAM*(T80) or B88M. All three candidate models feature an ENSO mode that is stable. Because all the constants and parameterisations in the new background states were independently tuned to accurately model the observations with no assumptions made about the resulting stability of the coupled system, these results suggest that the ENSO mode in nature is stable and that the reason that the ENSO mode is unstable in ZCM is due to the background states and parameter differences. It could be argued that assuming lower values of the western boundary reflection and ocean mechanical damping than are used in B88M and ZCM will always result in stable ENSO modes. However, running all three models, *LOAM*(a)-(c), with the western boundary reflection equal to 1.0 and the ocean damping equal to 30 months (as per ZCM, note that all other paramterisations remain the same) still results in ENSO modes that are stable: the decay rates of *LOAM*(a),

$LOAM$(b) and $LOAM$(c) with the original parameter values are increased to 0.80, 0.92 and 0.83 respectively[4]

A stable ENSO mode is in agreement with the observational estimates given by Penland and Sardeshmukh (1995)and Johnson (1999) using linear inverse techniques. However it should be noted that by construction the modes in linear inverse model are all stable. Thus the only way that it is possible to analyse the stability of the system is to linearise the equations about about the mean state; which is what has been done in this study. Since the mean states in this study represent much better estimates of the true state of the tropical Pacific than the means used in the ZCM, the stability of the ENSO mode that results is a better estimate of the true stability than estimates made using the mean states used in the original ZCM. It should be noted that analyses of the output of a number of ENSO models (see for example Chang et al., 1996) show that those models whose underlying ENSO dynamics are stable and linear give much better agreement to the observations than those models which contain unstable, chaotic ENSOs.

LOAM does not appear to be too sensitive to the differences among the new mean states, as it produces very similar results for all of the various combinations of new background states. The spatial patterns of the interannual variability in the models are the least sensitive to the changes in the background state. This lack of sensitivity bodes well for using the model as a tool to examine GCM output because it argues that the minutiae of the parameterisations are not that critical for accurately modelling the character of the tropical Pacific interannual variability. With this in mind we shall describe in the next chapter what happens when the mean calculation procedure and LOAM are used to examine the model output from the paleoCCSM run with modern day and early Holocene forcing.

---

[4]Optimally tuning δ_w and δ_T using the ZCM background states and ZCM subsurface parameterisations gives the values shown by the solid black line in fig 2.14. When these values of δ_w and δ_T are used along with the original ZCM background states in LOAM, the ENSO mode that results is stable: it has a decay rate of 0.27 year^{-1}. This run assumes a western boundary reflection of 0.7 and an ocean damping of 8.7 months. Using western boundary reflection of 1.0, ocean damping of 30 months and a drag coefficient of $2.5x10^{-3}$ (the values of these parameters in ZCM) still results in a stable mode: the decay rate is 0.86 year^{-1}.

Table 3.1: Summary table of the amount of variance explained by the first two EOFs, and ENSO mode properties, for various observational data sets and model runs. See text for explanation. The modal period and decay from observations are estimates from Johnson (1999) using (a) COADS and (b) NCEP/OI, and from Penland and Sardeshmukh (1995) using COADS, (c). The noise standard deviation is the peak standard deviation of the SST noise that is required to stochastically force *LOAM* and give a nino3 index that has the same variance as is observed.

Model	% variance in EOF 1	% variance in EOF 2	mode decay ($year^{-1}$)	mode period ($years$)	noise standard deviation
Kaplan	50	9.2	0.63(a), 0.53(b), 0.22(c)	4.1(a), 3.5(b), 3.8(c)	
NCEP/OI	45	12			
B88M	92	4.2	1.82	2.8	
LOAM(T80)	83	3.5	0.80	3.8	0.20
LOAM(a)	48	6.7	0.53	3.7	0.33
LOAM(b)	42	4.7	0.48	4.2	0.52
LOAM(c)	34	3.8	0.34	4.9	0.42

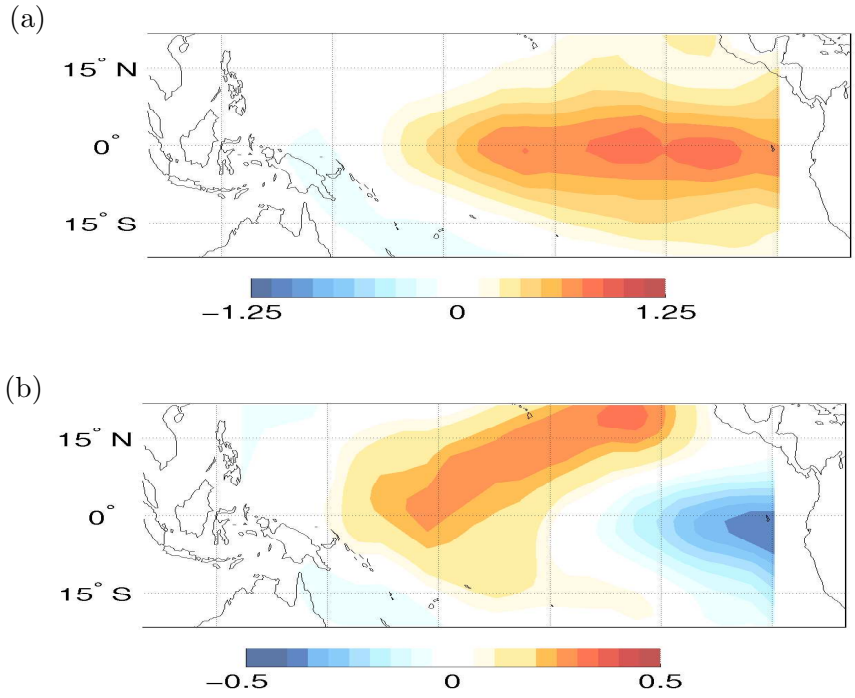

Figure 3.1: EOFs 1, (a), and 2, (b), from the Kaplan SST dataset. Contours are in °C.

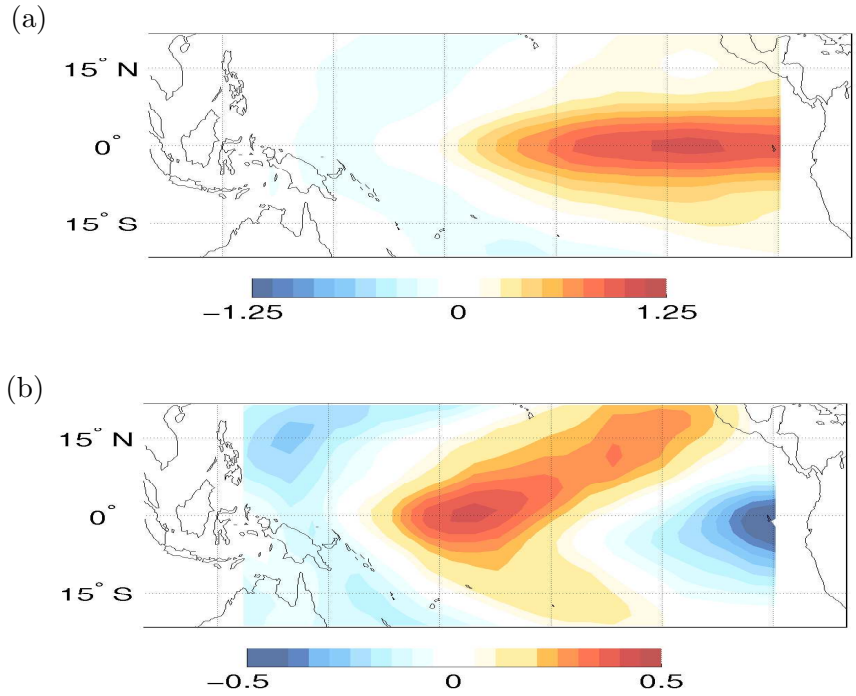

Figure 3.2: EOFs 1, (a), and 2, (b), from the NCEP/OI SST dataset. Contours are in °C.

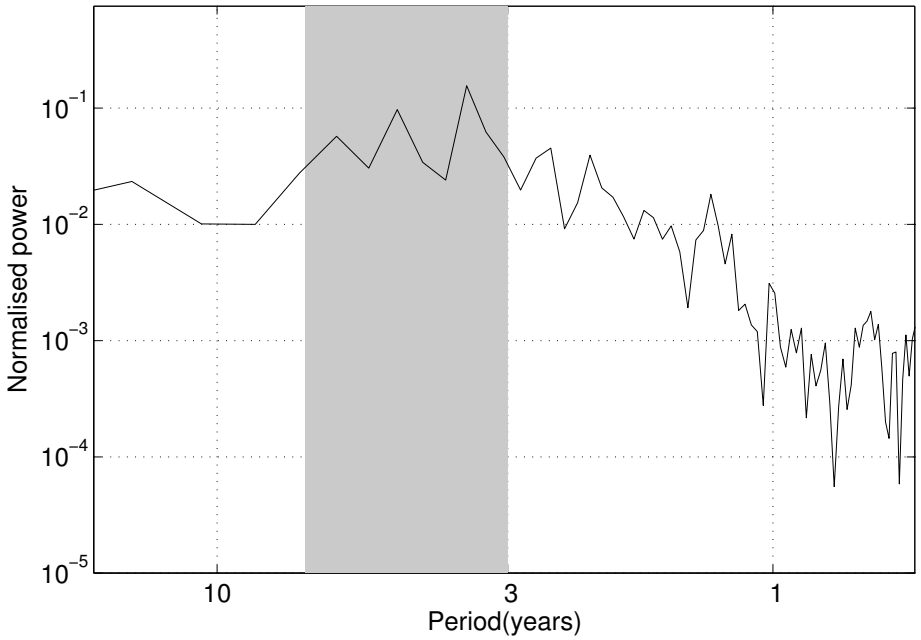

Figure 3.3: Power spectral estimates of nino3 index of the Kaplan SST dataset.

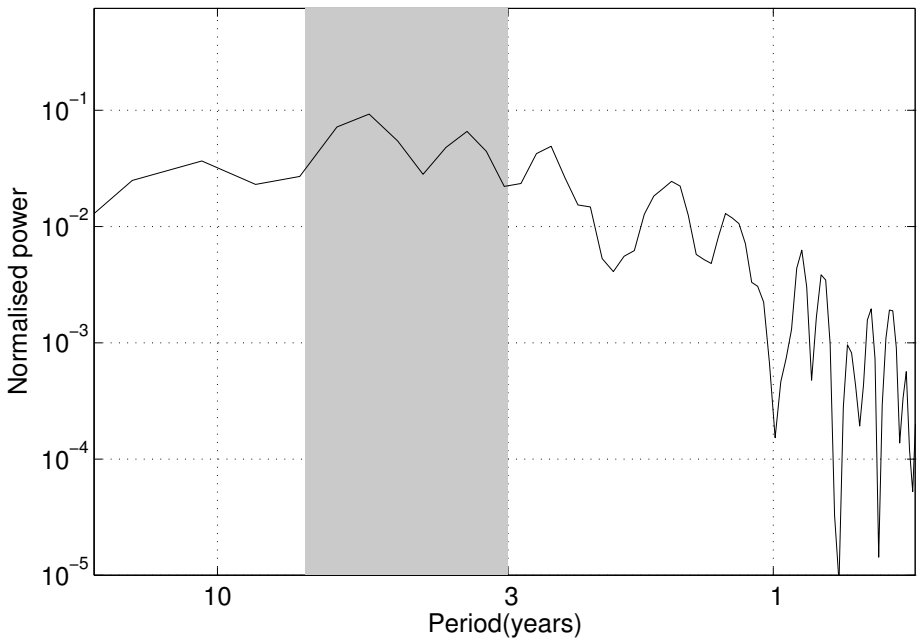

Figure 3.4: Power spectrum of the nino3 index from NCEP/OI SST dataset.

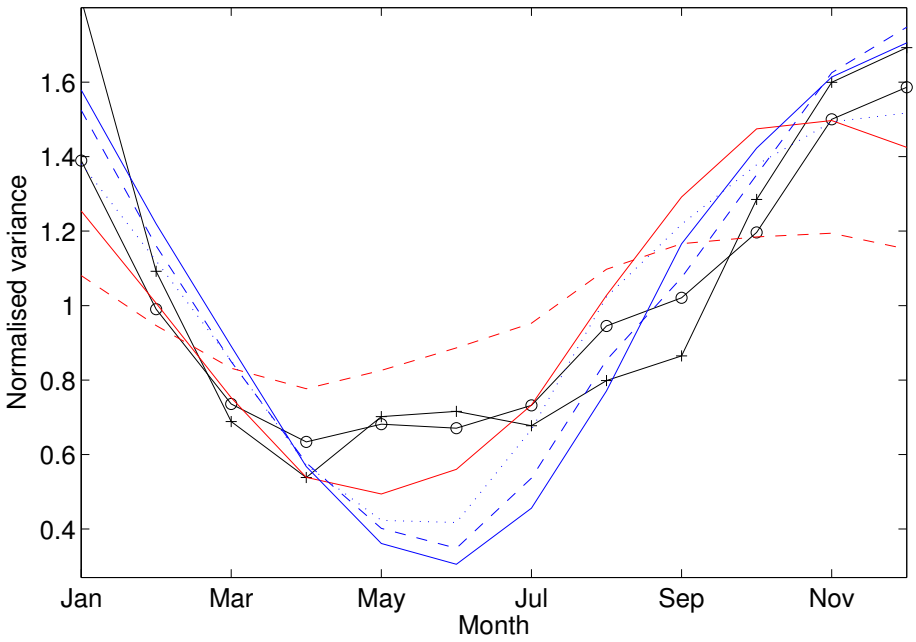

Figure 3.5: Variance of the monthly nino3 index, normalised by total variance. Solid black line with crosses, NCEP/OI data; solid black with circles, Kaplan dataset; red dashed, B88 model; red solid, T80 model; blue solid, $LOAM$(a) model; blue dotted, $LOAM$(b); blue dashed, $LOAM$(c).

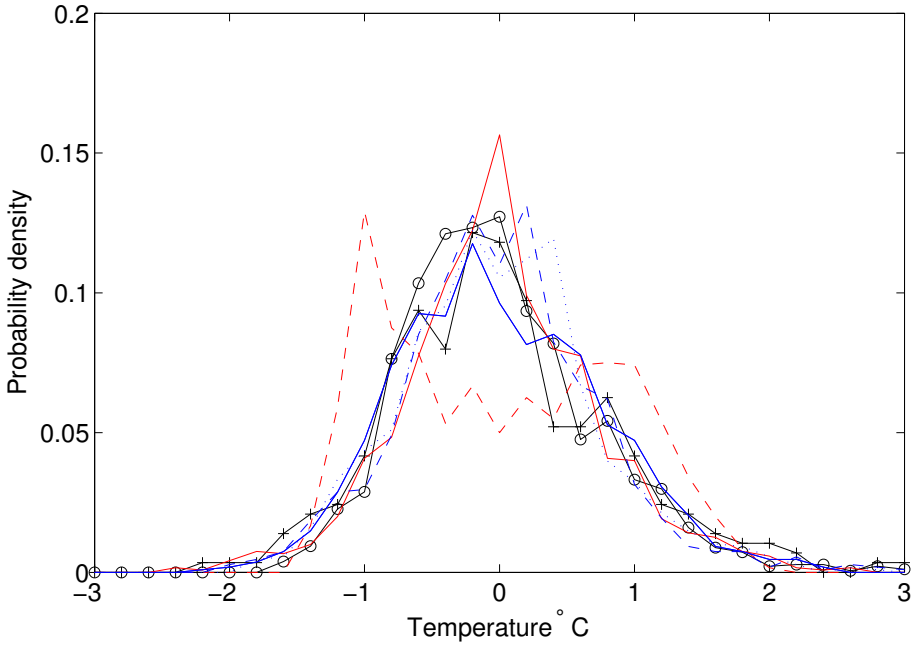

Figure 3.6: Probability density function nino3 SST anomaly. Solid black line with crosses, NCEP/OI data; solid black with circles, Kaplan dataset; red dashed, B88 model; red solid, T80 model; blue solid, $LOAM$(a) model; blue dotted, $LOAM$(b); blue dashed, $LOAM$(c).

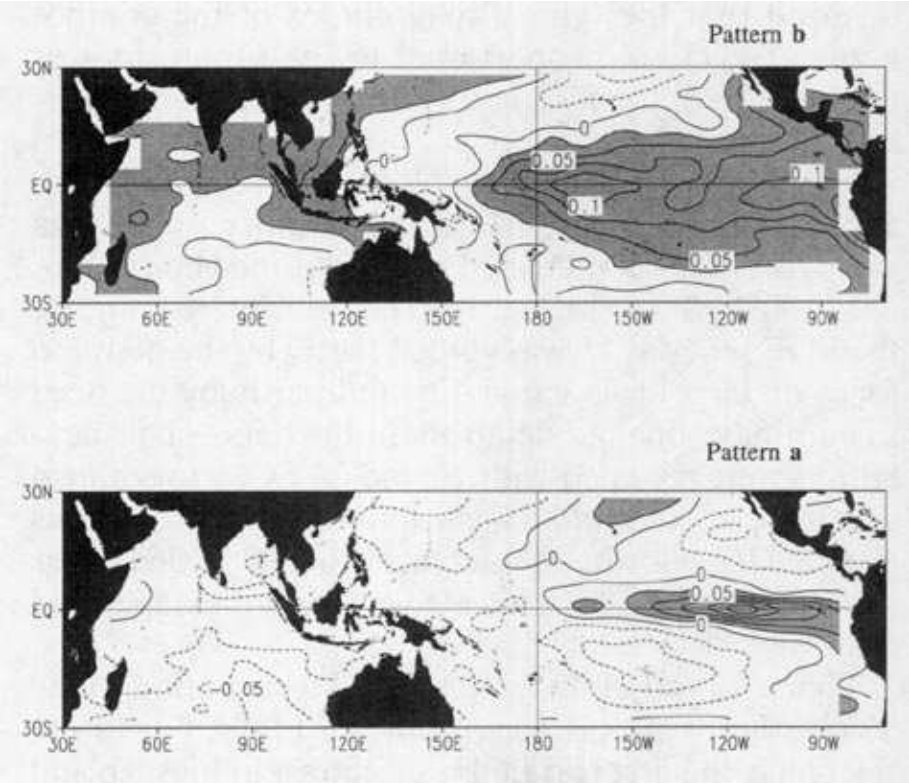

Figure 3.7: The ENSO mode reproduced from Penland and Sardeshmukh (1995). The mode evolves $b \rightarrow a \rightarrow -b \rightarrow -a$ over 3.8 years. The contour interval is arbitrary but the same in each panel.

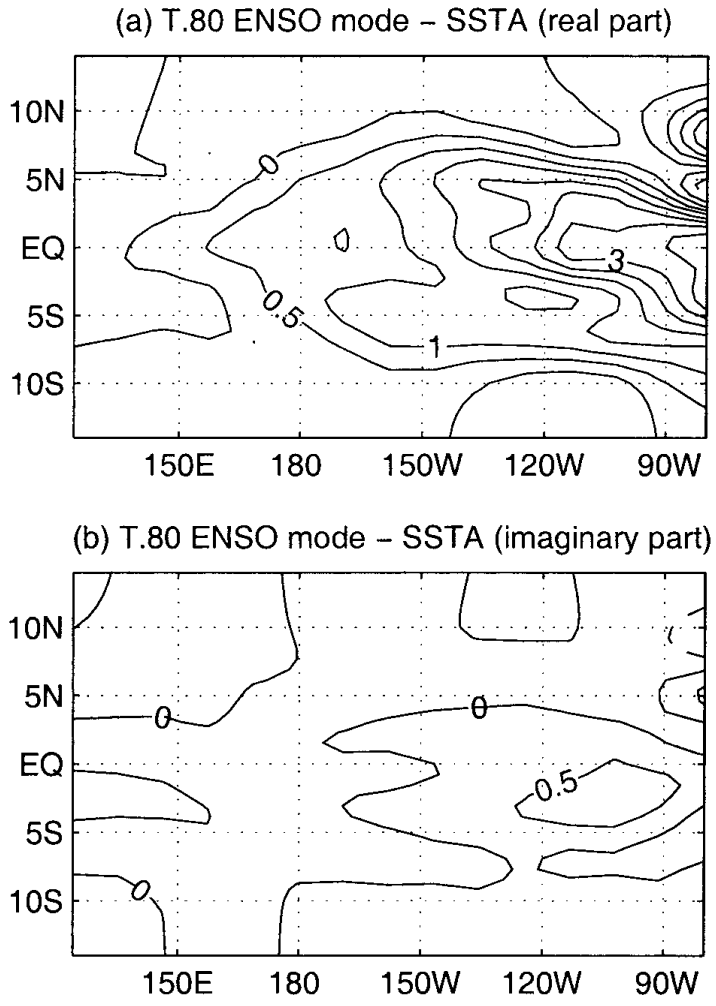

Figure 3.8: The SST part of the ENSO mode reproduced from Thompson and Battisti (2001). The mode evolves $a \rightarrow b \rightarrow -a \rightarrow -b$ over 3.8 years. The contour interval is arbitrary but the same in each panel.

Pattern a

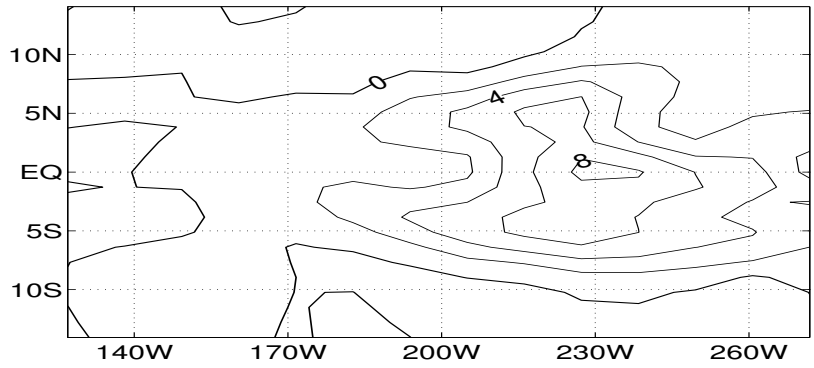

Pattern b

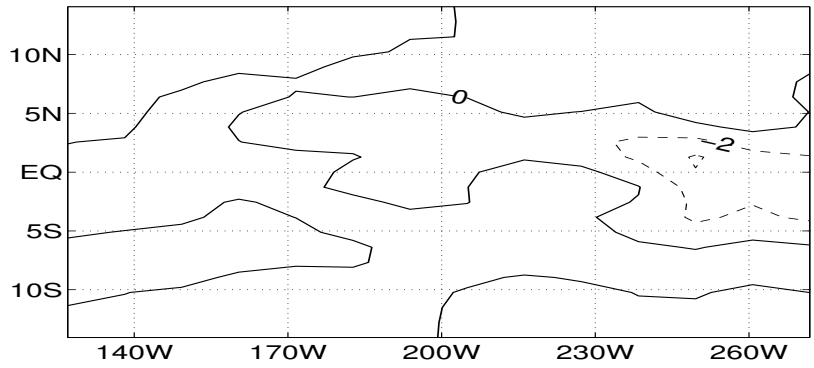

Figure 3.9: The SST part of the ENSO mode from the model $SODA/NCEP$. The mode evolves $a \rightarrow b \rightarrow -a \rightarrow -b$ over 3.7 years. The contour interval is arbitrary but the same in each panel.

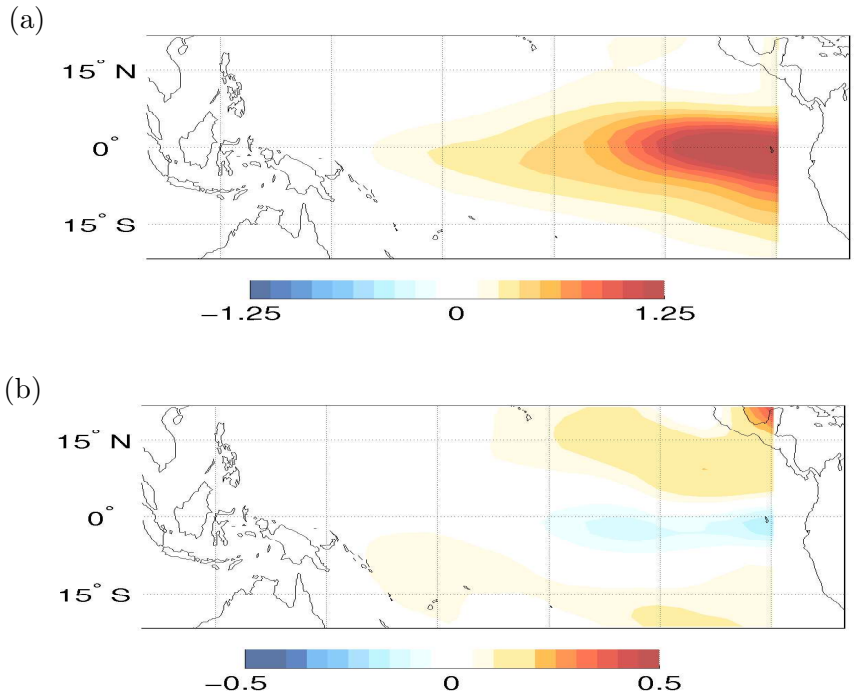

Figure 3.10: EOFs 1, (a), and 2, (b), from 100 years of a B88 model run. Contours are in °C.

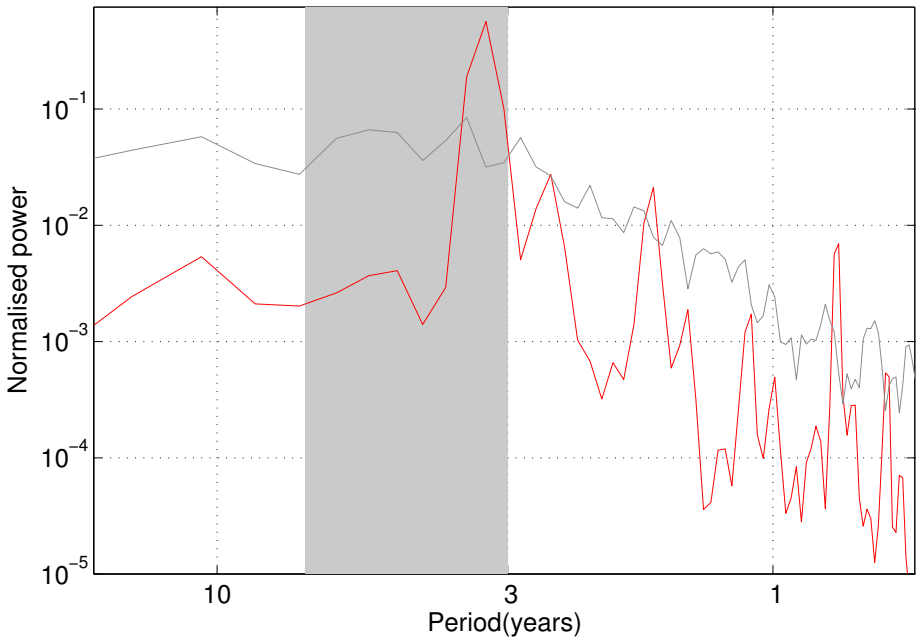

Figure 3.11: Power spectral estimates of nino3 SST. The red line shows estimates from 100 years of a B88 run, the grey line shows estimates from the Kaplan dataset

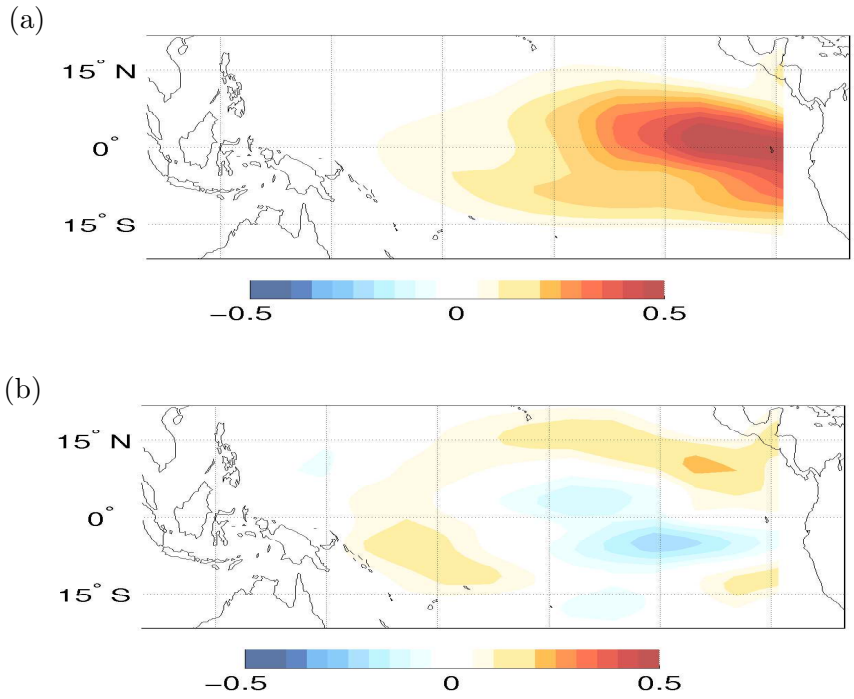

Figure 3.12: EOFs 1, (a), and 2, (b), from 100 years of a stochastically forced T80 model run. Contours are in °C.

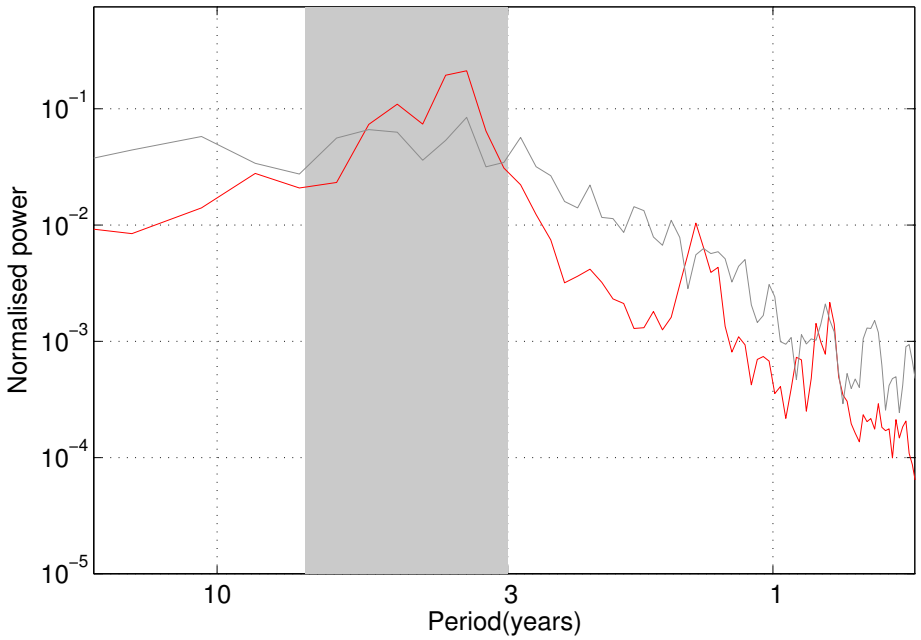

Figure 3.13: Power spectral estimates of nino3 SST. The red line shows estimates from 100 years of a stochastically forced run of T80, the grey line shows estimates from the Kaplan dataset

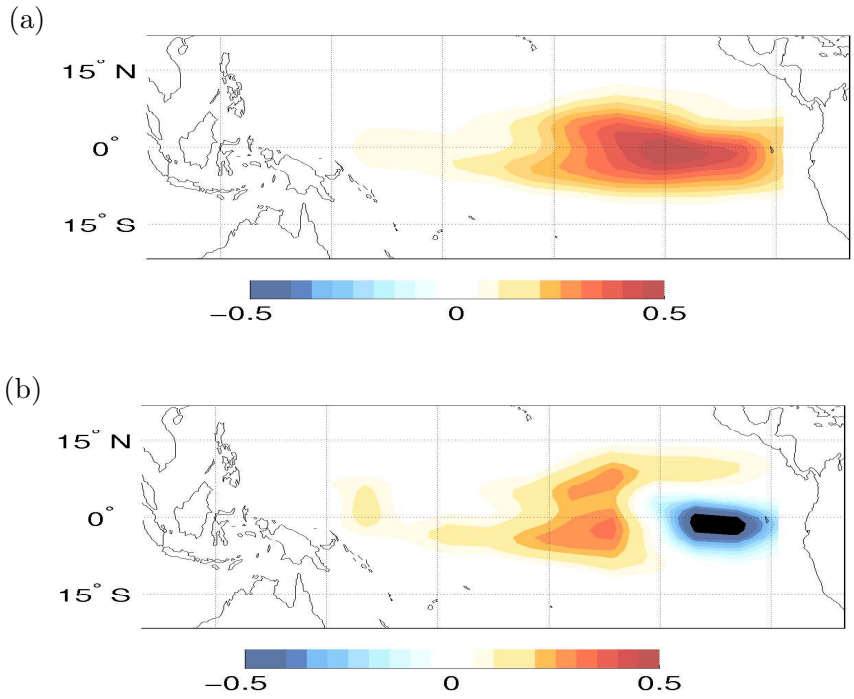

Figure 3.14: EOFs 1, (a), and 2, (b), from 100 years of a *LOAM*(a) run. Contours are in °C.

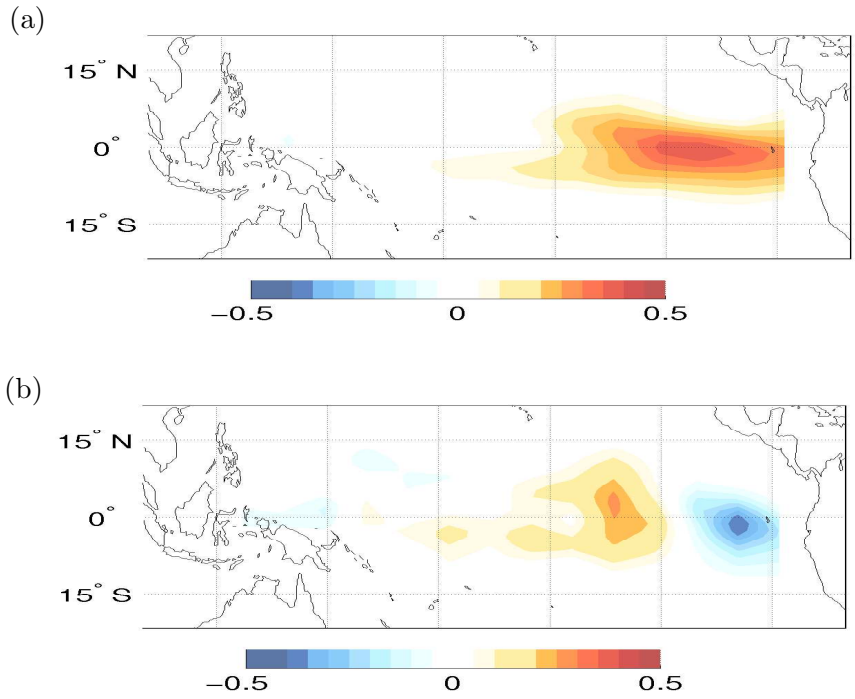

Figure 3.15: EOFs 1, (a), and 2, (b), from 100 years of a *LOAM*(b) run. Contours are in °C.

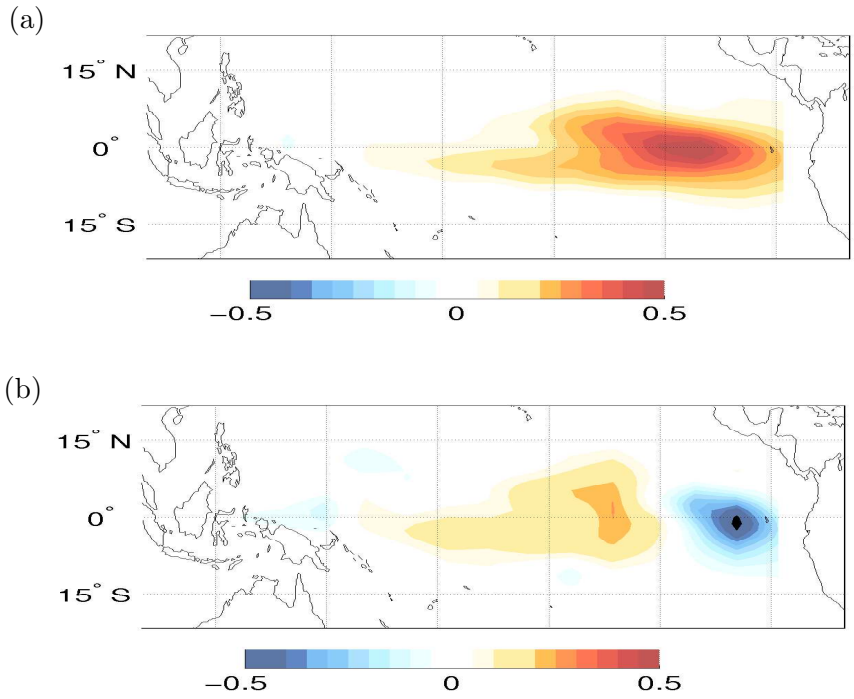

Figure 3.16: EOFs 1, (a), and 2, (b), from 100 years of a $LOAM$(c) model run. Contours are in °C.

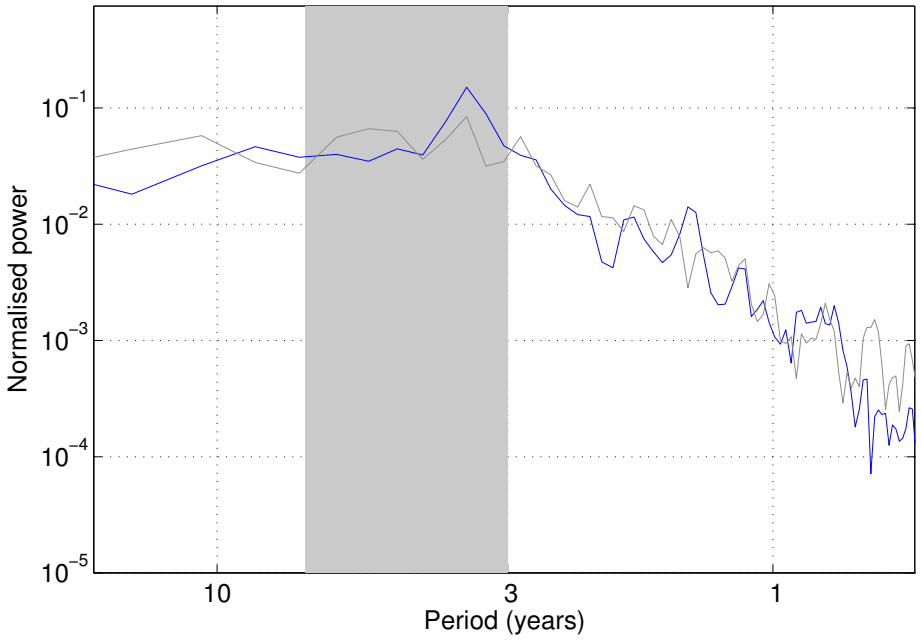

Figure 3.17: Power spectral estimates of nino3 SST. The blue line shows estimates from 100 years of a stochastically forced run of $LOAM$(a), the grey line shows estimates from the Kaplan dataset

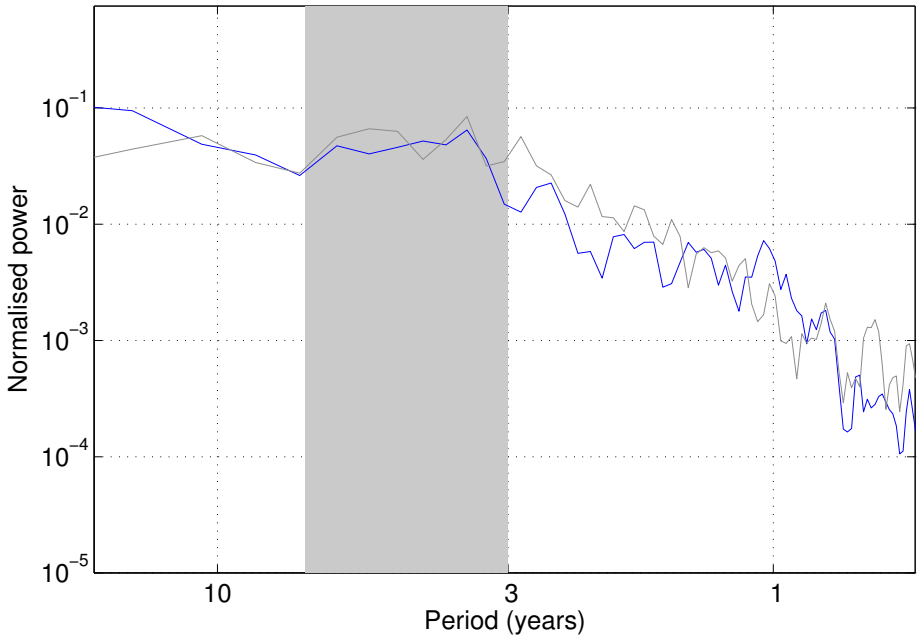

Figure 3.18: Power spectral estimates of nino3 SST. The blue line shows estimates from 100 years of a stochastically forced run of $LOAM$(b), the grey line shows estimates from the Kaplan dataset

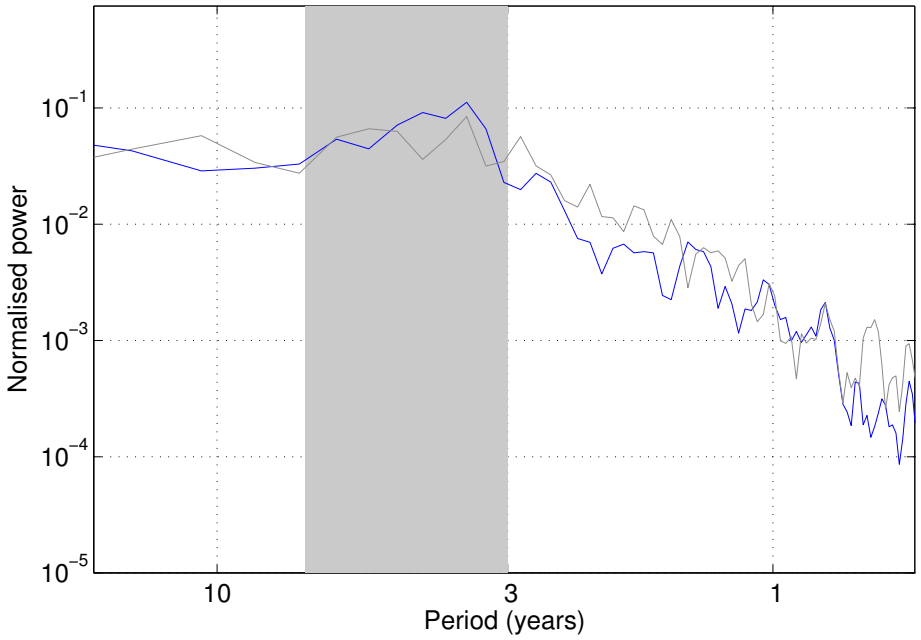

Figure 3.19: Power spectral estimates of nino3 SST. The blue line shows estimates from 100 years of a stochastically forced run of $LOAM$(c), the grey line shows estimates from the Kaplan dataset

Chapter 4

An Analysis of ENSO in Present Day and 8.5ka runs of paleoCCSM

4.1 Introduction

We recall from the opening chapter that the paleoCCSM runs of Otto-Bliesner et al. (2003) showed a reduction of 20% in the variance of the model's nino3 index when the model was run with 8.5ka forcing compared to today. Otto-Bliesner et al. (2003) conclude that the reason for this is that the stronger cold tongue during the early Holocene autumn causes the easterly Trades to be strengthened during that season, thus westerly wind anomalies due to growing ENSO events are inhibited. This is the same mechanism as proposed by Clement et al. (2000). It was also observed in the model that during the early Holocene the mean temperature of the tropical Pacific dropped and that the vertical temperature gradient across the thermocline weakened, especially in the far west.

Having shown, in the preceding chapter, that by using the method outlined in Chapter 2 we can produce a set of background states that allow LOAM to accurately model the present day ENSO, we shall now apply the technique to output from the paleoCCSM. Doing this will allow us to use LOAM to diagnose what causes the reduction in the SST variance observed in paleoCCSM. First, we will describe features of the modelled tropical Pacific mean state and interannual variability at 8.5ka and the present, and compare these to observations. Then, having calculated new background states for LOAM from the paleoCCSM output, we will use LOAM to show that the observed 20% reduction in the variance of the paleoCCSM nino3 at 8.5ka can be explained by changes in the climatological mean state alone: a change in the amplitude of the noise is not necessary to explain the decrease in the variance of nino3. Finally we shall assess which mean state changes are responsible for this reduction.

4.2 paleoCCSM at 8.5ka and the Present

We shall start by comparing the annual mean climate in the present day run of paleoCCSM, $CCSMp$, with observations. A much fuller discussion of the comparison between the present day of paleoCCSM and the observations may be found in Otto-Bliesner and Brady (2001). Figure 4.1 shows that the major features in the SST and surface winds are broadly similar between paleoCCSM and the observations. However, as we can see in fig. 4.1(a)-(c), the cold tongue in the paleoCCSM extends farther to the west than does the observed cold tongue and, south of the equator, the warmer water extends farther to the east than in the observations. We can see in fig. 4.1(d)-(f), that on the equator the easterly Trades in the paleoCCSM are weaker than those observed and, as is shown in fig. 4.1(g)-(i), the meridional winds are more southerly in the paleoCCSM than they are in observations. Figure 4.2 shows the ocean currents averaged over the top 50m of the ocean. We see in fig. 4.2(a)-(c) that the major difference between paleoCCSM and the observations is that, in the annual mean, the zonal current on the equator is not eastward in the paleoCCSM as it is in observations. We also see in fig. 4.2(g)-(i) that in the paleoCCSM the equatorial upwelling west of 240°E is weaker than observed. This weaker upwelling is consistent with the weaker Trades in the paleoCCSM. The variance of the paleoCCSM nino3 index is $0.52(^{\circ}\mathrm{C})^2$, which compares well with the nino3 variance from the Kaplan dataset of $0.50(^{\circ}\mathrm{C})^2$. Figure 4.3 shows the probability density function of the nino3 SST anomaly for the Kaplan SST data set, in the black line with circles, and for two paleoCCSM runs with present day forcing (red solid line) and 8.5ka forcing (red dashed line). We can see that the paleoCCSM modelled nino3 follows a Gaussian distribution. This allows us to justify the use of the linear ocean atmosphere model (LOAM), in the analysis of the paleoCCSM output.

The first EOF of monthly mean SST anomalies from $CCSMp$ is shown in fig. 4.4. The SST anomalies used in fig. 4.4 have been smoothed with a three month running mean and indeed all SST datasets used in this chapter are smoothed with a three month running mean

in order to remove high frequency variability. The EOF in fig. 4.4 can be compared to the observations in figs. 3.1 and 3.2. Note that the second EOF in the $CCSMp$ data is not distinct from higher order EOFs, unlike the second EOF from the observations. The first EOF of SST in $CCSMp$ is similar to the observations, the major difference being that the paleoCCSM EOF is more constrained to the equator and it extends too far to the west. Power spectral estimates of the nino3 from $CCSMp$ are shown in the red line in fig. 4.5. For reference a grey line shows the spectral estimates from the Kaplan SST data set. The $CCSMp$ spectrum is very similar to the observed.

From this discussion it is apparent that ENSO variability, and many aspects of the mean state in $CCSMp$ agree with observations. Given that the model reproduces the present day ENSO it is, therefore, worthwhile examining how the model's ENSO changes with early Holocene climate forcing.

We shall now compare the mean state in the present day paleoCCSM run, $CCSMp$, and the run with 8.5ka forcing, $CCSM8.5$. In fig. 4.6 (a)-(c) we see that the annual mean SST is broadly similar between both models, with a cold tongue in the east, and warm pool in the west. However, at 8.5ka the SST is everywhere cooler, especially just to the east of the data line. This means that the zonal SST gradient in the west central Pacific is stronger at 8.5ka than during the present. The stronger zonal SST gradient is associated with stronger easterly Trades in this region, as shown in fig. 4.6 (d)-(f).

Stronger Trades at 8.5ka would lead one to expect there to be stronger oceanic upwelling on the equator and we see, in fig. 4.7(g)-(i), that at 8.5ka there is stronger equatorial upwelling collocated with the strengthening of the Trades. This stronger upwelling will tend to cool the surface and indeed there is cooled SST where there is strengthened upwelling. However, the strengthened upwelling is in a narrow band right on the equator, whereas the change in SST is a much broader pattern meridionally. The broad extent of the cooling may be explained by the reduction in the net surface radiative flux at 8.5ka (shown in fig. 4.8), which is accomplished by the changes in atmospheric circulation (the net change in the

annual average insolation at the top of the atmosphere is zero). Everywhere in the tropical Pacific the net surface radiative flux is less at 8.5ka, especially around 10°N where the ITCZ is located. The area of maximum cooling of SST on the equator between 170°W-230°W is due to more than just the reduced radiative flux: it is also due to a strengthening of the wind speed that can be seen in fig. 4.9. This stronger windspeed cools the surface by changing the balance of terms in the latent heat flux.

In fig. 4.10 we see that along the equator the temperature is cooler at all depths except for within the thermocline west of about 200°E, where it is warmer. An average over the box 2.5°N-2.5°S, 205°E-245°E, chosen to coincide with the biggest change in upwelling, shows how the thermocline structure there changes. This is shown in the rightmost panels of fig. 4.10. At 8.5ka the vertical temperature gradient at the depth of the 20°C isotherm, whose depth is shown by the blue($CCSM8.5$) and red($CCSMp$) lines, is weaker at 8.5ka than at present. This is due to the cooling of the ocean between 100-150m being less the cooling at the surface. The depth of the 20°C isotherm is shallower at 8.5ka than at present, this is due to the general cooling of the ocean. The vertical temperature gradient at 50m, $\overline{T_z}$, is weaker in this area at 8.5ka than at present.

What the change in the subsurface temperature means for the two functions K_T and K_w, which are defined in eqns. 2.2 and 2.4, is shown in fig. 4.11(a)-(b). K_T, which indicates how the SST tendency in the linearised ZCM is affected by movements in the thermocline, is generally larger at 8.5 ka than at present, especially in the far east Pacific. This means that the SST tendency is more affected by thermocline displacements at 8.5ka than at present. Recalling from eqn 2.12 that Γ, and therefore K_T, is a function of the gradients of $f(h)$ and $cs(h_{20})$, we see in fig. 4.11(c)-(d) that the in the far east the change in the gradients of $f(h)$ and $cs(h_{20})$ are both of the same sense, and both act to increase the sensitivity of T_{50} to changes in the layer depth, h. K_w, shown in fig. 4.11(b), which indicates how upwelling anomalies affect SST in the linearised ZCM, is generally smaller west of about 240°W at 8.5ka than today. This reflects the weakening of vertical temperature gradient across the

thermocline, as shown in fig. 4.10.

The spatial patterns of the interannual variability are shown in figs. 4.4 and 4.12 as the first EOF of the monthly mean SST anomalies. Compared to each other we see that the two patterns are generally similar except that at 8.5ka the maximum in the pattern is shifted farther east than in the present. Recall that the second EOF from $CCSMp$ is not a distinct pattern: nor is that from $CCSM8.5$. The shift to the east of the peak in the variance of the first EOF of $CCSM8.5$ is consistent with the the enhancement of K_T and K_w in the far east at that time.

The power spectra of the nino3 index, shown as the red lines in figs. 4.5 and 4.13 for $CCSMp$ and $CCSM8.5$ respectively, show that the there is no obvious difference in the model's spectral characteristics at 8.5ka and today. Furthermore the spectra are similar to the observed spectrum, which is shown as the grey lines in both figures.

Table 4.1 shows that the variance of the nino3 index from paleoCCSM at 8.5ka is 81% of that at the present. In terms of absolute size, the variance during the present is $0.52°C^2$, at 8.5ka it is $0.42°C^2$. For reference the present day nino3 variance according to the Kaplan dataset is $0.50°C^2$. The reduction of the variance in paleoCCSM is not as large as the estimate of Tudhope et al. (2001), who estimate a reduction to 20% of the present variance, but it is a statistically significant reduction.

We see that there are number of differences in both the mean state and the interannual variability between the two model runs $CCSMp$ and $CCSM8.5$. We will now show how LOAM behaves when the background states derived from the two runs of paleoCCSM are used.

4.3 ENSO modes in LOAM and paleoCCSM

As is outlined in Penland and Sardeshmukh (1995) it is possible to create an empirical linear model of the tropical Pacific SST using a number of PCs of the observed anomalous monthly mean SST there. The estimates of the ENSO mode period and decay shown in

the top row of Table 3.1 were derived from eigenmode decompositions of such models. One can follow the same procedure with output from paleoCCSM to derive an empirical linear model of the tropical Pacific and then decompose that model into its eigenmodes.

Shown in Table 4.1 are estimates of the ENSO mode period and decay rates from linear models empirically derived from the first 10 PCs of SST and the first 5 PCs of h_{20} from $CCSMp$ and $CCSM8.5$.

In $CCSMp$ the period and decay of the ENSO mode are 3.3 years and .52 year^{-1} respectively, which is in agreement with the range of estimates of the mode statistics from the present day observations, shown in Table 3.1. The pattern of the SST part of the mode in $CCSMp$, shown in fig. 4.14, also agrees with the observational estimate in fig. 3.7, although as with the first EOF of SST from $CCSMp$ the mode is a little too confined to the equator and extends too far to the west.

The period of the mode from $CCSM8.5$ is 3.8 years which is longer than the period of the mode in $CCSMp$. This is reasonable to expect since the first EOF of SST from $CCSM8.5$ has its peak located farther east than $CCSMp$, as we can see in figs 4.4 and 4.12, thus it takes longer for reflected wave feedbacks to take effect in $CCSM8.5$ than $CCSMp$, and so the mode period is longer. The shift to the east in the peak variance of the ENSO can also be seen in the empirical modes shown in figs. 4.14 and 4.15. The peak in the mode is located farther east at 8.5ka than at present.

When background states are derived from the runs $CCSMp$ and $CCSM8.5$ and incorporated into LOAM, we can decompose LOAM into its eigenmodes. The background states are calculated following the procedure outlined in Chapter 2. Recall that the parameters δ_w and δ_T in K_T and K_w, were tuned to minimise the error in modelled SST along the equator when the ocean was forced with the present day windstress anomalies and the resulting SST calculated. δ_w and δ_T in this set of experiments were tuned using data from $CCSMp$ and these values used for all experiments. Since the choice of δ_w and δ_T is somewhat subjective it was decided that in order to remove this source of subjectivity from the model analysis

the same values should be used in all runs. The atmosphere model was also tuned in the manner outlined in Chapter 2. The drag coefficient used is $2.26 \cdot 10^{-3}$ which is 1.8 times the generally accepted value of $1.25 \cdot 10^{-3}$.

The modes that are calculated from LOAM using background states from $CCSMp$ and $CCSM8.5$ are shown in figs. 4.16 and 4.17, respectively. The peak in the mode using background states from $CCSM8.5$ is located farther to the east than that derived using $CCSMp$ background states. This is consistent with modes derived from the empirical models of the paleoCCSM data. The periods of the ENSO modes in the two LOAM runs are both shorter than those derived from the empirical linear model. The mode using $CCSMp$ background states has a period of 2.2 years and that using$CCSM8.5$ background states has a period of 2.9 years, which compare with 3.3 and 3.9 years. We should note that although the two modes in LOAM have shorter periods than either the observational estimates or the estimates from the linear mode decomposition of the paleoCCSM output the mode in LOAM using $CCSM8.5$ background states does have a longer period than the LOAM mode using $CCSMp$ background states, which is consistent with the empirical modes. This lengthening of the mode period at 8.5ka appears as a consistent feature in the analysis of the principal modes in the paleoCCSM data and, as was previously stated, this is consistent with the eastward shift in the peak of the mode at 8.5ka.

Having shown that LOAM contains ENSO modes that qualitatively resemble the modes empirically derived from paleoCCSM, we shall now stochastically force the two versions of LOAM.

4.4 Analysis of the CCSM runs using LOAM

In order to run LOAM we must specify a stochastic forcing. This forcing is white noise, normally distributed about the equator acting as a perturbation to the SST field. The amplitude of the noise was chosen such that the variance of the nino3 index in a run of LOAM using background states from $CCSMp$ is the same as the variance of nino3 in

$CCSMp$. This same amplitude of noise was used in all subsequent runs of LOAM. Using the same amplitude of noise means that any change in the SST variance that we observe is due to the changes in the background state of the model being analysed. We will first show results from the two runs $LOAMp$ and $LOAM8.5$, which are the runs of LOAM using background states from the $CCSMp$ and $CCSM8.5$ respectively.

Figures 4.18 and 4.19 show the EOFs for the runs $LOAMp$ and $LOAM8.5$. The first EOF of each LOAM run compares well with its paleoCCSM counterpart (figs. 4.4 and 4.12 respectively). The extension of the pattern into the west central Pacific is shown, as is the tight constraint to the equator. The shift to the east of the maximum in the first EOF of $CCSM8.5$ is also apparent in $LOAM8.5$. The power spectra of the two LOAM runs are shown in fig. 4.20 for $LOAMp$ and fig. 4.21 for $LOAM8.5$. In each figure the blue line shows spectral estimates for the LOAM nino3, the light red line shows estimates from the paleoCCSM run from which the LOAM background states were derived and, finally, the grey line shows spectral estimates of the Kaplan nino3. Both LOAM runs show more peaked spectra than the spectra from the paleoCCSM runs from which they are derived. It is also worth noting that $LOAM8.5$ has a peak at a longer period than $LOAMp$. This is consistent with the longer period of the ENSO mode in $LOAM8.5$ than in $LOAMp$.

As is shown in Table 4.1, the variance of nino3 in $LOAM8.5$ is 0.79 times that of $LOAMp$. This agrees well with observed reduction of 0.81 seen between $CCSMp$ and $CCSM8.5$. Recall that no change in the noise amplitude was made between $LOAMp$ and $LOAM8.5$, so this reduction is solely due to the changes in the background state.

So we see that LOAM captures reasonably well the temporal and spatial characteristics of the interannual variability in paleoCCSM. Given that LOAM with paleoCCSM background states does a good job of reproducing the ENSO in paleoCCSM, we will now use the model to probe which background states give rise to the observed changes in the interannual variability.

4.5 Diagnosis of the Important Background States using LOAM

As a way of diagnosing the cause of the observed change in the behaviour of ENSO during the early Holocene in paleoCCSM, we shall systematically change the background states in $LOAMp$ replacing them with different background states from the set used in $LOAM8.5$. Although doing this is not entirely physically consistent, it will give us an idea of what mean state processes are important in causing the reduced ENSO variability. We shall start with changing ocean background states and then change those background states that are used in the atmosphere. Results for the experiments are recorded in Table 4.1 and unless otherwise stated, the means will be added to $LOAMp$ from $LOAM8.5$.

4.5.1 Ocean means

The first experiment, $LOAMp + ocn$, replaces all the ocean background states of $LOAMp$ with those from $LOAM8.5$. The background states changed are: $u_1, v_1, w_1, \Gamma, \overline{T_z}$, SST and windspeed. Note that the windspeed and SST in the atmosphere model remain the same as $LOAMp$. Table 4.1 shows that the ENSO mode becomes less stable, the decay rate becomes 0.81 year^{-1} from 0.7 year^{-1} and the period increases from 2.2 years to 2.9 years. The variance of the nino3 from the stochastic run of this model increases by a factor of 1.35. This increase shows that oceanic processes alone are not responsible for the observed reduction in SST variance at 8.5ka, however ocean processes do appear to be responsible for lengthening the mode period.

In order to test the importance of the subsurface parameterisations Γ and $\overline{T_z}$, the run $LOAMp + \Gamma + \overline{T_z}$ replaces only the two subsurface parameterisations Γ and $\overline{T_z}$ with values from $LOAM8.5$. This leads to a far more unstable ENSO mode, that has a decay of 0.92 year^{-1}, up from 0.7 year^{-1}, it also has a longer period of 2.9 years up from 2.2 years. The nino3 variance goes up by a factor of 2.47. This suggests that it is the changes in the subsurface parameterisations that are the most important in lengthening the period and

destabilising the ENSO mode.

We recall from fig. 4.11 that the sense of the change in K_w and K_T from the present to 8.5ka was not the same: K_w became smaller at 8.5ka, due to the more diffuse thermocline, and K_T larger, due to the mean raising of the thermocline. The two runs $LOAMp + \Gamma$ and $LOAMp + \overline{T_z}$, will show the relative importance of these two terms in changing the ENSO mode. $LOAMp + \Gamma$ replaces only Γ with its $LOAM8.5$ value: this changes K_T. We see in this experiment a significant decrease in the stability of the ENSO mode: the decay rate goes from 0.7 to 0.93 year^{-1} and the variance in a stochastic run goes up by a factor of 2.8. The period of the ENSO mode is also increased significantly from 2.2 to 2.9 years. $LOAMp + \overline{T_z}$ replaces $\overline{T_z}$ with its $LOAM8.5$ value in order to change K_w This increases the stability of the ENSO mode slightly. The decrease in the variance of nino3, however, is not significant. Thus the increase in the mode period appears to be due to the change in Γ, since changing $\overline{T_z}$ has no noticeable effect on the mode. Recall that the change in Γ was due to both an increase in the sensitivity of T_{50} to changes in the depth of h_{20} and an increase in the sensitivity of h_{20} to h.

The last experiment in the ocean suite is $LOAMp + curr$. This replaces only the ocean currents u_1, v_1, w_1, in $LOAMp$ with their $LOAM8.5$ counterparts: this will show us how important the currents are in producing the observed change in $LOAM + ocn$. $LOAMp + curr$ shows an increase in the stability in the stability of the ENSO mode, as the decay rate goes from 0.7 to 0.67 year^{-1}, and a shortening in its period, a decrease from 2.15 to 2 years, thus the currents do not play a role in making the mode less stable nor do they cause the mode period to lengthen. We should note, however, that the variance of nino3 increases. Although we may expect that a more stable ENSO mode would display less SST variance as discussed in Thompson (1998), due to the non-normality of the coupled system, the decay of the ENSO mode does not tell the whole story: mode-mode interactions are also important. Furthermore, the variance in a noise driven damped oscillator increases as the period decreases. As the ENSO mode period decreases in $LOAMp + curr$ this could explain

why this model's nino3 variance increases. Note that the change in the mode properties of $LOAM + ocn$ are closer to those in $LOAM + \Gamma + \overline{T_z}$ than $LOAM + curr$. In particular $LOAM + curr$ does not capture the lenghtening of the period that is observed in $LOAM8.5$ and $LOAM + ocn$, thus the changes in $\overline{T_z}$ and Γ are more important in explaining the change in the ENSO mode than are the changes in the currents.

The conclusion from this series of experiments is that the ocean background states from 8.5ka tend to make the ENSO mode less stable and to lengthen the mode period. In particular it is the parameterisation Γ alone which makes the biggest difference in destabilising the ENSO mode and lengthening its period.

4.5.2 Atmosphere Means

Replacing the atmosphere background states, SST and windspeed, in $LOAMp$ with their 8.5ka counterparts, to give experiment $LOAMp+atm$, results in a more stable ENSO mode, as shown in Table 4.1. Note that in this experiment the SST and windspeed in the ocean are not the same as those in the atmosphere. When run with stochastic forcing the variance of nino3 drops by 0.52, compared to $LOAMp$. This leads one to believe that the observed reduction in nino3 variance observed in paleoCCSM is due to an increase in the stability of the ENSO mode caused by a change in the atmospheric background state, since the ocean background states from $LOAM8.5$ made the mode less stable. Because there are only two background states in the atmosphere, it is easy to test which is the more important.

First, we will introduce the linearised equation that governs the atmosphere. All the terms in the Gill atmosphere (Gill, 1980) are already linearised except for the convergence feedback term which can be linearised, following Battisti and Hirst (1989), as

$$ {c_a}^2 \frac{\partial U}{\partial x} + {c_a}^2 \frac{\partial V}{\partial y} + A\phi = K_Q T + K_c \left(\frac{\partial U}{\partial x} + \frac{\partial V}{\partial y}\right) , \tag{4.1} $$

where

$$K_C(x,y) = -\alpha_s {c_a}^2 H(-\frac{\partial \overline{U}}{\partial x} - \frac{\partial \overline{V}}{\partial y}) \tag{4.2}$$

and

$$K_Q(x,y) = \gamma {c_a}^2 (2\beta/c_a)^{1/2} \left[\frac{T_{ref}}{\overline{T}(x,y)}\right]^2 exp\left[b(\frac{1}{T_{ref}} - \frac{1}{\overline{T}(x,y)})\right] . \tag{4.3}$$

c_a is the characteristic wind velocity, $A = 1.567 \cdot 10^{-5} s^{-1}$ the damping, $\gamma = 1.4 m K^{-1} s^{-1}$, $T_{ref} = 303K$ and $\overline{T}$ is the mean temperature that we shall specify. U, V are the atmospheric winds, where those with overbars denote background states that we specify. $H(x)$ is the Heaviside function, defined in eqn. 2.3 and $\alpha = 0.75$ is an efficiency factor.

$LOAMp + T_{atm}$ uses only the SST, the term $\overline{T}(x,y)$ in eqn. 4.3, from $LOAM8.5$. This increases the stability of the ENSO mode, the modal decay goes from 0.7 to 0.62 year^{-1} but the modal period is not significantly changed. The variance of the nino3 index in $LOAM + T_{atm}$ is reduced to 0.49 of that in $LOAMp$. In $LOAM8.5$ $\overline{T}(x,y)$ is everywhere less than in $LOAMp$: this reduces the magnitude of K_Q which reduces the size of heating anomalies in the atmosphere for a given SST anomaly. This then gives rise to smaller windstress anomalies, and in this way the coupling between the atmosphere and ocean is reduced, thus the ENSO mode is stabilised. Figure 4.22 demonstrates what happens to windstress anomalies when the mean SST in the atmosphere is changed. The linearised atmosphere model is computed for the present day atmosphere, in fig. 4.22(a), and the 8.5ka atmosphere fig. 4.22(b). Both atmospheres are then forced by the same timeseries of SST anomalies and the resultant windspeed anomalies calculated. Shown is the variance of the zonal wind for these timeseries: this represents the mean squared amplitude of the zonal windspeed anomalies. As can be seen in fig. 4.22 (c) the variance of the windspeed over the troipcal Pacific waveguide is reduced by around 5% at 8.5ka compared to the present day run. This is in line with our intuition: a 1°C in the SST will lead to approximately a 6% reduction in the saturated vapour pressure, which would lead us to expect a reduction in the windstress variance of a similar size, which is, on average, what we see. Since we see a

reduction in the variance of the nino3 index of 0.62 for this change in the SST, we might ask is this large reduction in the stability of the coupled mode in line with the small reduction in the windstress variance. In order to verify this, we can run the coupled model with a reduced coupling coefficient to mimic the effect of the reduced windstress variance. If we take the $LOAMp$ set of parameters and background states and reduce the coupling coefficient by 6%, we find that the decay rate of the ENSO mode is increased to 0.64 year^{-1}. This compares to decay rates of 0.7 year^{-1} for $LOAMp$ and 0.62 year^{-1} for $LOAMp+T_{atm}$. Reducing the coupling coefficient reduces the variance of the nino3 index to 0.63 of the control variance, which compares to a reduction of 0.63 for $LOAMp+T_{atm}$. These changes are very similar to those from the run $LOAMp+T_{atm}$. So the reduction in the SST gives a reduction in the variance of the windspeed in line with our expectations, and the increase in the stability of the ENSO mode is close to what we would expect given the change in the coupling strength that we see.

$LOAMp+\tau_{atm}$ replaces only the windspeed in the atmosphere with the 8.5ka. This tests the importance of the convergence feedback term, K_C, to changes in the background state windspeed. A small decrease in the stability of the ENSO mode is shown, 0.7 to 0.71 years^{-1}, but the decrease in the variance of nino3 is not significant.

It has been suggested, e.g. Clement et al. (2000), that the cause of the reduction in ENSO activity during the early Holocene is the change in the seasonal cycle of SST. Since the experiment $LOAMp+T_{atm}$ shows that SST in the atmosphere is the most important stabiliser of the ENSO mode, it is worth testing whether it is the change in seasonality of SST that is the cause of this. Two experiments, $LOAMp+mean(T_{atm})$ and $LOAMp+cyc(T_{atm})$ were run to test this. $LOAMp+mean(T_{atm})$ uses $LOAMp$ background states for all fields except the SST in the atmosphere. This SST is derived by calculating the seasonal cycle of the SST from $LOAMp$ and adding this to the annual mean SST from $LOAM8.5$, thus the seasonal cycle in this experiment is the same as in $LOAMp$ but the annual mean SST is as in $LOAM8.5k$. $LOAMp+cyc(T_{atm})$ is a similar experiment but in this case the

seasonal cycle comes from $LOAM8.5$ and the annual mean SST from $LOAMp$. We see in Table 4.1 that changing the seasonal cycle of SST to that from 8.5ka, in experiment $LOAMp + cyc(T_{atm})$, does not reduce the variance of nino3 rather it increases it, although this change in the variance is not statistically significant. $LOAMp + mean(T_{atm})$ shows a reduction in the variance of nino3 of 0.47, and a drop of the decay rate of the ENSO mode from 0.7 to 0.61 year^{-1}. This shows that it is the annual mean cooling of tropical Pacific SST that causes the increases in the stability of the ENSO mode: the change in the seasonality is unimportant. This agrees with Wang and An (2002) who have noted that, when considering the climate shift in the 1970's, seasonal cycle changes are not nearly as important as annual mean background state changes in altering the properties of ENSO.

4.5.3 A Final Test

In order to verify that Γ in the ocean and the SST in the atmosphere are the most important background states in changing the stability of the ENSO mode, we run two further experiments: the first experiment, called $LOAM8.5+\Gamma$, uses all the $LOAM8.5$ mean states except for Γ, which is from $LOAMp$; the second, called $LOAM8.5+T_{atm}$, uses the SST from $LOAMp$ in the atmosphere and $LOAM8.5$ background states everywhere else. Since Γ from $LOAM8.5$ had a destabilising effect on the ENSO mode in $LOAMp$, we should expect that Γ from $LOAMp$ will stabilise the ENSO mode in $LOAM8.5$. Table 4.1 shows that this is indeed the case: the mode decay goes from 0.74 in $LOAM8.5$ to 0.59 in $LOAM8.5+\Gamma$. Note also that the mode period drops from 2.9 years to 2.0 years, which verifies the importance of Γin setting the period of the mode.

Since the SST in the atmosphere from 8.5ka stabilised the ENSO mode in $LOAMp$, we expect that the SST from $LOAMp$ will destabilise the ENSO mode in $LOAM8.5$, which is indeed what we see. The ENSO mode decay rate in $LOAM8.5+T_{atm}$ is 0.84 year^{-1}, which compares to the decay rate of 0.74 year^{-1} in $LOAM8.5$. In both experiments the change in the variance of nino3 is in the sense that we expect: in $LOAM8.5+\Gamma$ the variance decreases

and in $LOAM8.5 + T_{atm}$ the variance increases in comparison to $LOAM8.5$.

These two experiments verify that the results from the experiments adding mean states to $LOAMp$. This adds weight to the result that the SST from 8.5ka acts to stabilise the ENSO mode but that Γ from 8.5ka acts to lengthen the mode and destabilise it.

4.6 Discussion

LOAM well represents the leading mode of the interannual variability in paleoCCSM both temporally and structurally. In the present day runs the mode in LOAM and paleoCCSM also agree with the observed ENSO mode. LOAM captures the observed reduction in the variance of nino3 between the present and 8.5ka runs of paleoCCSM, when background states from these runs are used. No change in the amplitude of the white noise forcing is needed to explain the reduction in the variance of nino3. Replacing piecemeal the various background states from $CCMS8.5$ to $CCSMp$, and vice versa, we can demonstrate that at 8.5ka, although the ocean part of the system becomes less stable and gives a longer period mode, the atmosphere becomes less responsive to SST anomalies due to the cooled mean SST at 8.5ka: this causes smaller wind anomalies. In the case of paleoCCSM it appears that the ENSO variance decreases in the early Holocene because the ENSO mode is stabilised, the stabilisation being caused by a competition between an atmosphere that is less responsive and an ocean that is more responsive in which the atmospheric effect wins out.

Although this piece by piece approach to replacing mean states is not entirely physically consistent, it has allowed to us to gain an understanding into how the coupled system seems to work in paleoCCSM. Furthermore, if one looks at how the variance in nino3 changes for the two experiments $LOAMp + \Gamma$ and $LOAMp + T_{ate}$ we see changes by factors of 2.8 and 0.49 respectively. These are huge changes, so it is hard to argue that they are not dominant.

Given the success in modelling the paleoCCSM and diagnosing its ENSO changes we should ask how applicable is the paleoCCSM to the real world. The foremost criticism

of the paleoCCSM is that it does not show a reduction in nino3 variance that is as large as observed by Tudhope et al. (2001). Furthermore, the seasonal cycle in the present day tropical Pacific as simulated by paleoCCSM is not good (Otto-Bliesner and Brady, 2001), and it can also be argued that the model's ENSO is not a good reproduction of reality, although it is among the best simulated ENSOs when compared to other GCMs. That being said, what we have learnt from the model, is that we need to show caution when analysing how mean states changes affect ENSO.

We should also recall from Chapter 1 that the only consistent paleodata for the early Holocene showed that there was a warming of around 1°C in the far west Pacific, compared to today[1]. The far west Pacific is far away from the area where cooling is important in causing a reduction in ENSO variance in CCSM. There are no observations that say what the temperature was in the central Pacific in the early Holocene, so no data can verify whether the model is right or wrong.

As a further test of the use of LOAM to analyse output from paleoCCSM, a short analysis of the output from a run using boundary conditions from the last galcial maximum (LGM) (Otto-Bliesner et al., 2003, a run we shall call $CCSM\ lgm$) was undertaken. Shown in Table 4.2 are the changes in variance and mode statistics for a number of runs of LOAM using the LGM background states. The run $LOAM\ lgm$ uses the full set of background states and subsurface parameterisations from the LGM and we see that the variance of the nino3 index is increased in this run in line with the increase seen between $CCSMp$ and $CCSM\ lgm$. As can be seen in fig 4.23, the annual mean SST is much reduced during the LGM, this will reduce the response of the atmosphere, and would lead us to expect a reduction in the variance of nino3 during the LGM. The experiment $CCSMp + lgm_{atm}$, which uses the present day ocean and LGM atmosphere shows this is indeed the case. The ENSO mode decay rate is decreased from 0.70 year^{-1} to 0.43 year^{-1} and the variance of

[1]see fig. 1.1 for the location of the Gagan et al. (1998) and Stott et al. (2004) data

nino3 is decreaed to 0.16 of that in $CCSMp$. Recall however that the variance of nino3 in $CCSMlgm$ is increased. This is due to changes in the ocean, which becomes much more responsive to windstress anomalies during the LGM. Figure 4.24, which shows the ocean temperature averged between 2.5°N-2.5°S, shows that the equatorial ocean is significantly cooler during the LGM run than during the present day run and also that the mean depth of the thermocline is raised during the LGM. Experiment $LOAMp + lgm_{ocn}$ uses the mean states for the present in the atmosphere and the mean states for the LGM in the ocean. The ENSO mode in this experiment is unstable. Thus the increase in the variance of nino3 during the LGM in paleoCCSM may again be explained by a competition between the increaesed responsiveness of the ocean and a decreased responsiveness of the atmosphere during the LGM. Unlike during the early Holocene when the change in the atmosphere dominates the change in the ocean, during the LGM the increased responsiveness of the ocean wins out.

Table 4.1: The variance of various paleoCCSM runs as a fraction of the variance in the paleoCCSM present day run. Where the linear model, LOAM, is used the modal period and annual decay rate is given. Shading indicates a decrease in variance from the control run. See text for explanation of abbreviations

Model	variance / (variance of $CCSMp$)	mode period (years)	mode decay (year^{-1})
$CCSMp$	1.00	3.27	0.55
$CCSM8.5$	0.81	3.78	0.56
$LOAMp$	1.00	2.15	0.7
$LOAM8.5$	0.79	2.92	0.74
$LOAMp + ocn$	1.35	2.87	0.81
$LOAMp + \Gamma + \overline{T_z}$	2.42	2.94	0.92
$LOAMp + \overline{T_z}$	0.87	2.2	0.69
$LOAMp + \Gamma$	2.83	2.89	0.93
$LOAMp + curr$	1.38	2.00	0.67
$LOAMp + ate$	0.51	2.27	0.63
$LOAMp + T_{atm}$	0.49	2.3	0.62
$LOAMp + \tau_{atm}$	1.12	2.11	0.71
$LOAMp + cyc(T_{atm})$	1.06	2.13	0.70
$LOAMp + mean(T_{atm})$	0.47	2.31	0.61
$LOAM8.5 + T_{atm}$	1.53	2.80	0.84
$LOAM8.5 + \Gamma$	0.57	2.00	0.59

Table 4.2: The variance of various paleoCCSM runs as a fraction of the variance in the paleoCCSM present day run. Where the linear model, LOAM, is used the modal period and annual decay rate is given. Shading indicates a decrease in variance from the control run. See text for explanation of abbreviations

Model	variance / (variance of $CCSMp$)	mode period (years)	mode decay (year^{-1})
$CCSMp$	1.00	3.27	0.55
$CCSM\ lgm$	1.14	3.30	0.56
$LOAMp$	1.00	2.15	0.7
$LOAM\ lgm$	1.12	3.39	0.80
$LOAMp + lgm_{ocn}$	N/A	2.88	1.45
$LOAMp + lgm_{atm}$	0.16	2.66	0.43

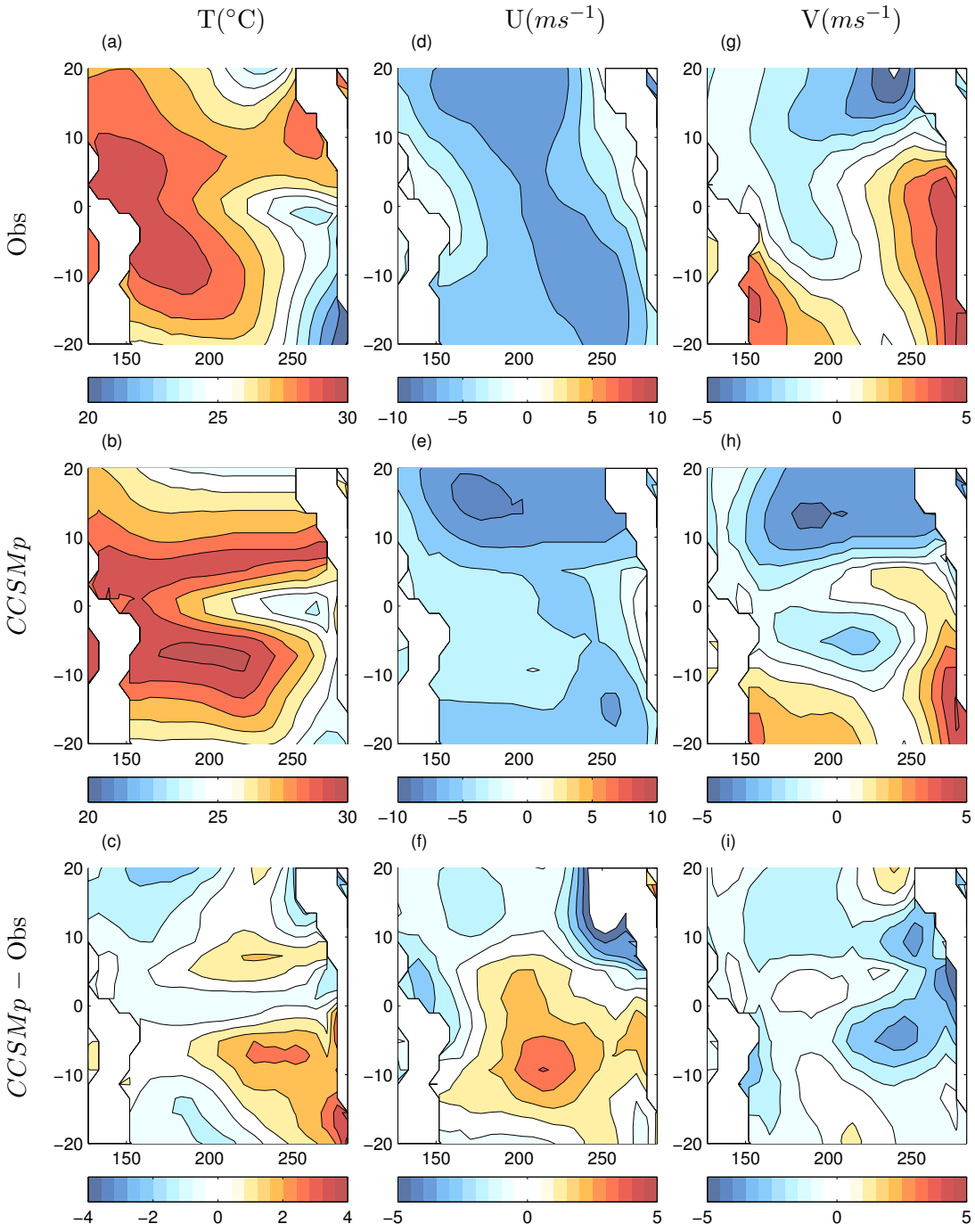

Figure 4.1: Annual mean SST from observations in (a), $CCSMp$ in (b), and the difference in (c). Annual mean zonal wind from observations in (d), $CCSMp$ in (e), and the difference in (f). Annual mean meridional wind from observations in (g), $CCSMp$ in (h), and the difference in (i). The fields are those that are entered into LOAM.

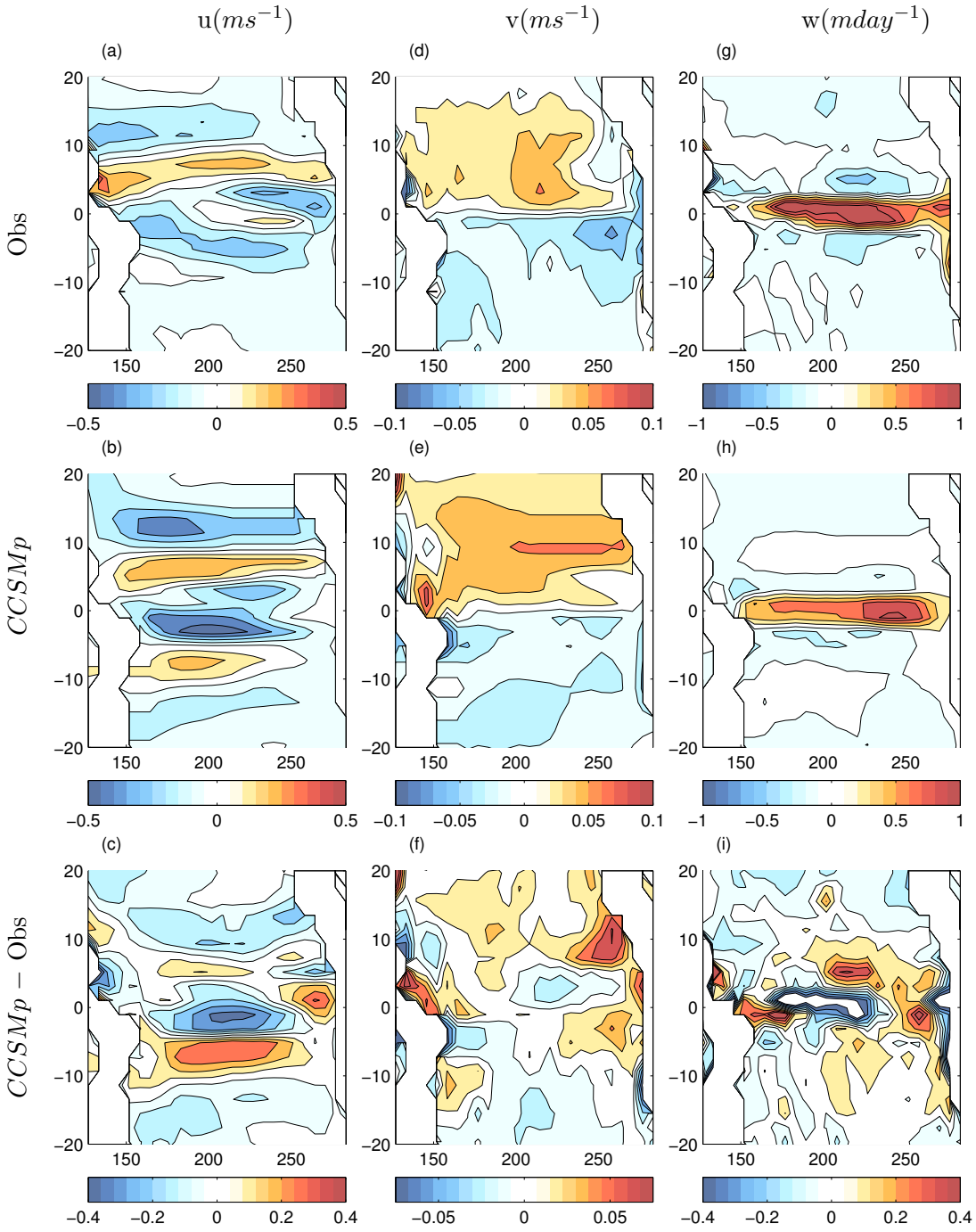

Figure 4.2: Annual mean zonal currents from observations in (a), $CCSMp$ in (b), and the difference in (c). Annual mean meridional current from observations in (d), $CCSMp$ in (e), and the difference in (f). Annual mean upwelling from observations in (g), $CCSMp$ in (h), and the difference in (i). The fields are those that are entered into LOAM.

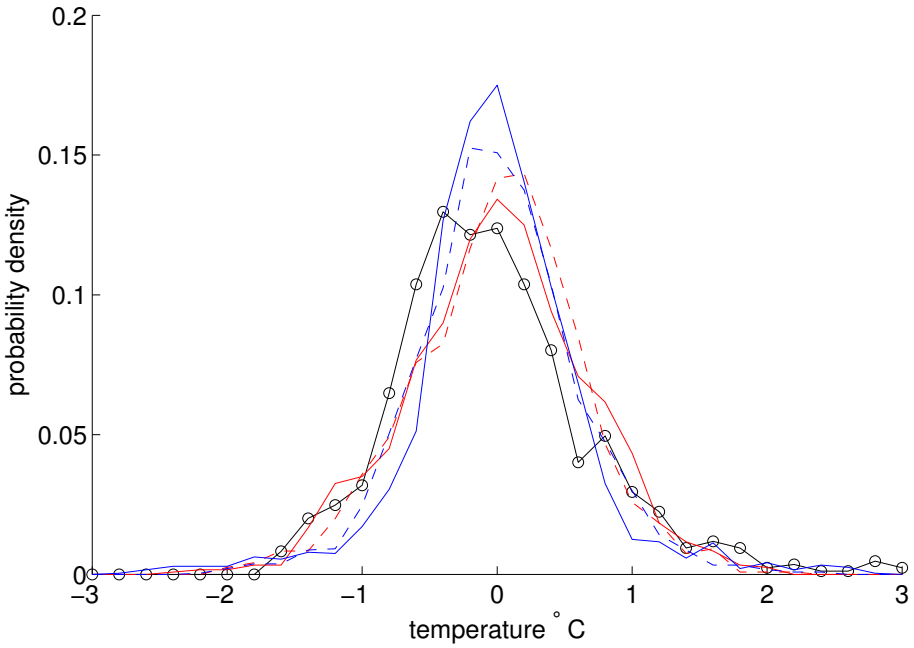

Figure 4.3: Probability density function of the nino3 SST. Solid black with circles shows the nino3 from the Kaplan dataset, the red solid, $CCSMp$; the red dashed, $CCSM8.5$; the blue solid, $LOAMp$; the blue dashed, $LOAM8.5$.

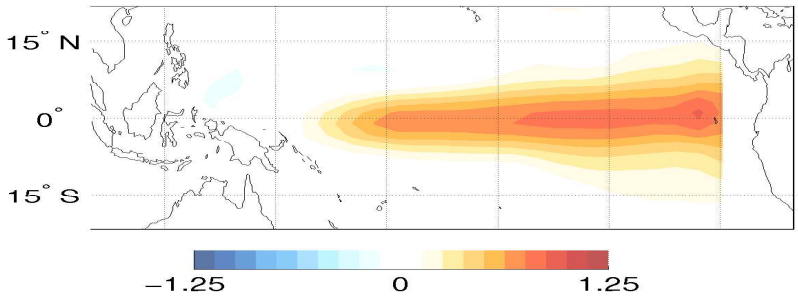

Figure 4.4: EOF 1 for SST anomalies from $CCSMp$. Contours are in °C.

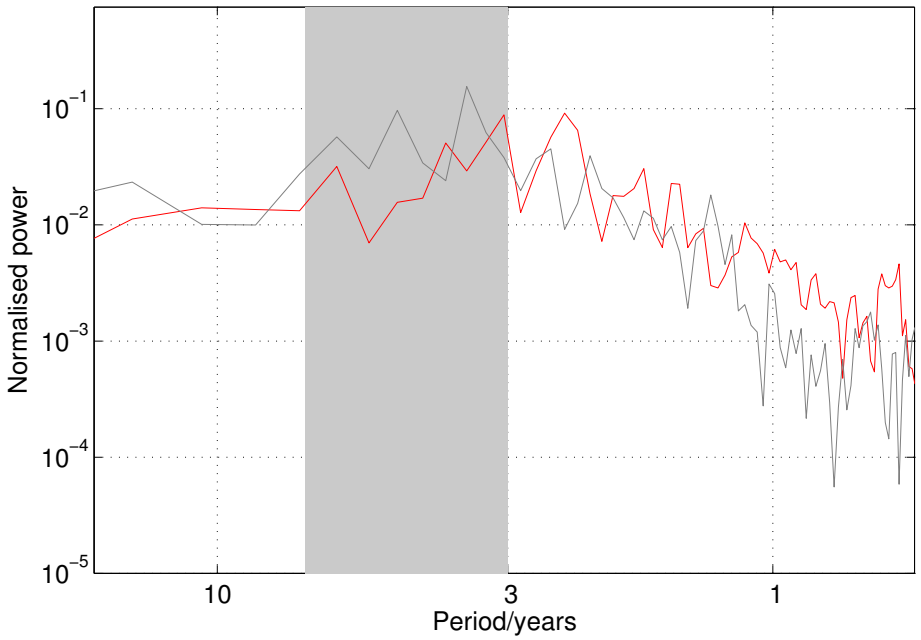

Figure 4.5: Power spectrum of the nino3 index for $CCSMp$. The red line is power spectral estimates from $CCSMp$ and the grey line from the Kaplan dataset

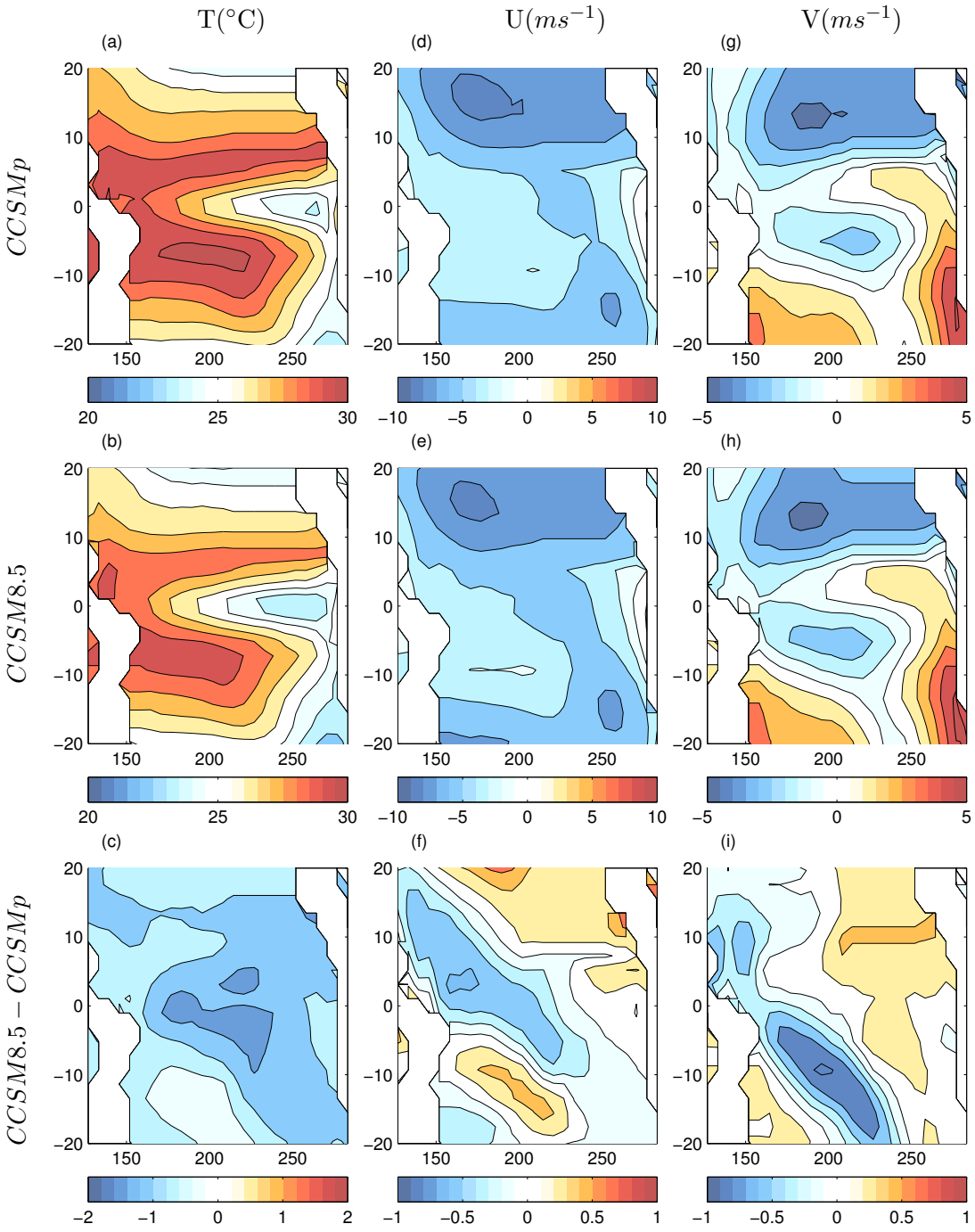

Figure 4.6: Annual mean SST from $CCSMp$ in (a), $CCSM8.5$ in (b), and the difference in (c). Annual mean zonal wind from $CCSMp$ in (d), $CCSM8.5$ in (e), and the difference in (f). Annual mean meridional wind from $CCSMp$ in (g), $CCSM8.5$ in (h), and the difference in (i). The fields are those that are entered into LOAM.

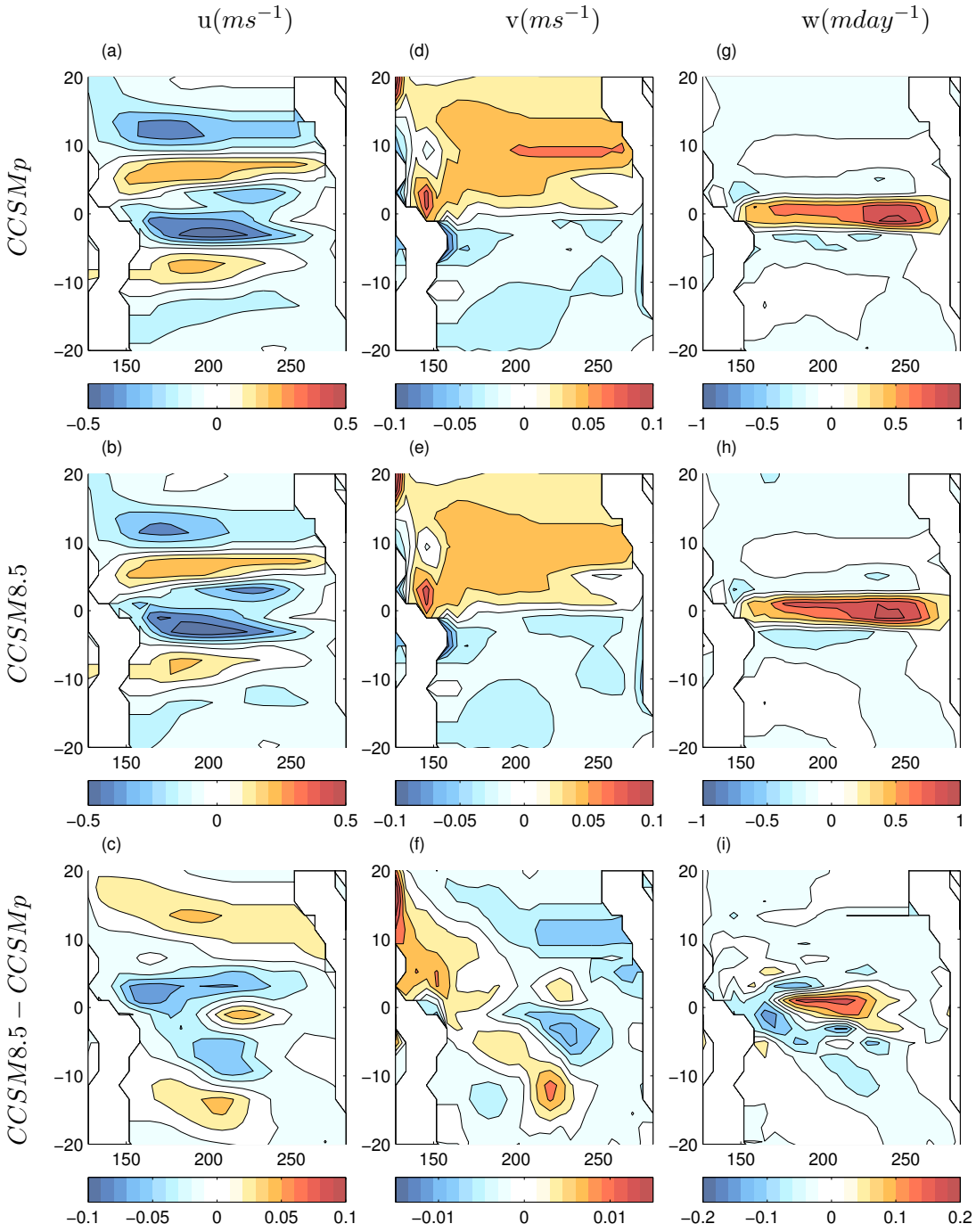

Figure 4.7: Annual mean zonal current from $CCSMp$ in (a), $CCSM8.5$ in (b), and the difference in (c). Annual mean meridional current from $CCSMp$ in (d), $CCSM8.5$ in (e), and the difference in (f). Annual mean upwelling from $CCSMp$ in (g), $CCSM8.5$ in (h), and the difference in (i). The fields are those that are entered into LOAM.

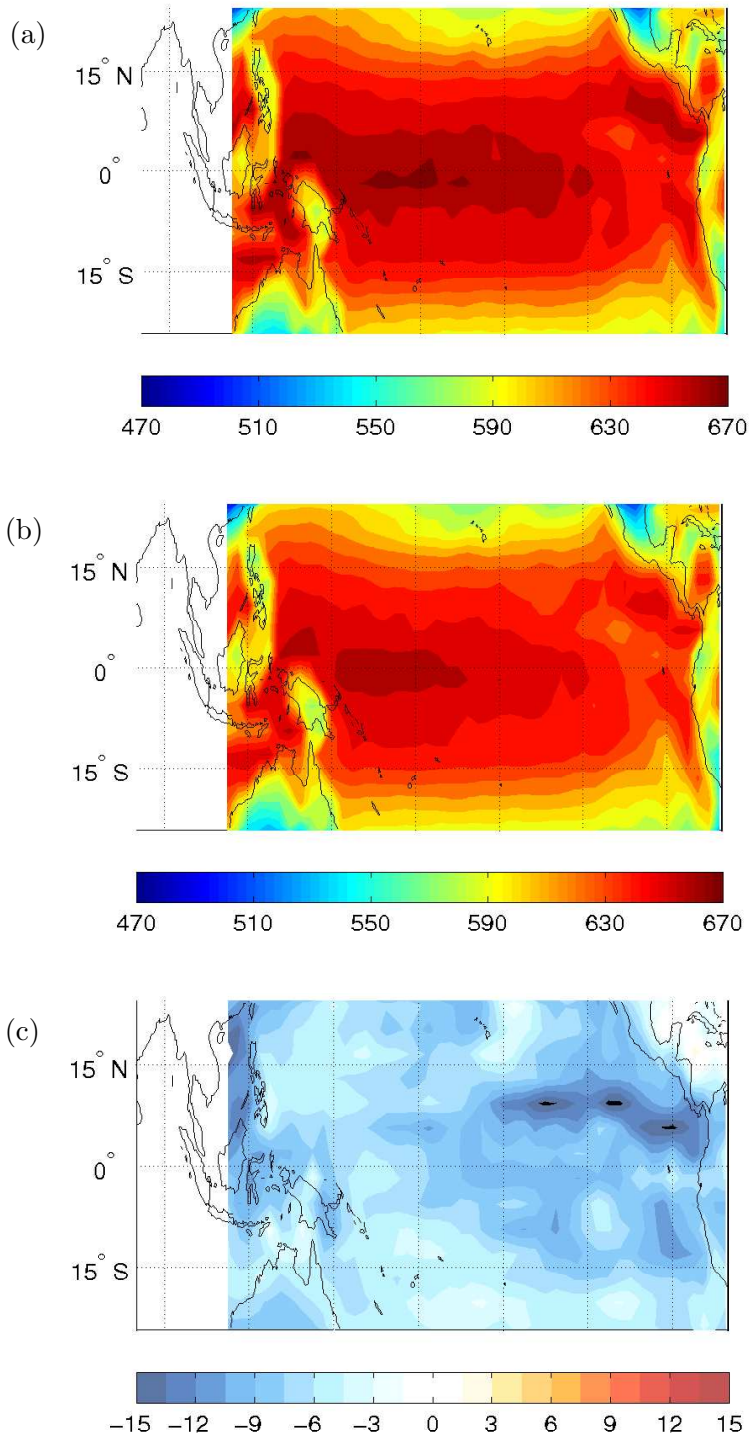

Figure 4.8: Annual mean net surface radiative flux (Wm^2), over the tropical Pacific, from (a) present day and (b) 8.5ka runs of paleoCCSM. (c) shows the difference between the 8.5ka and present day runs.

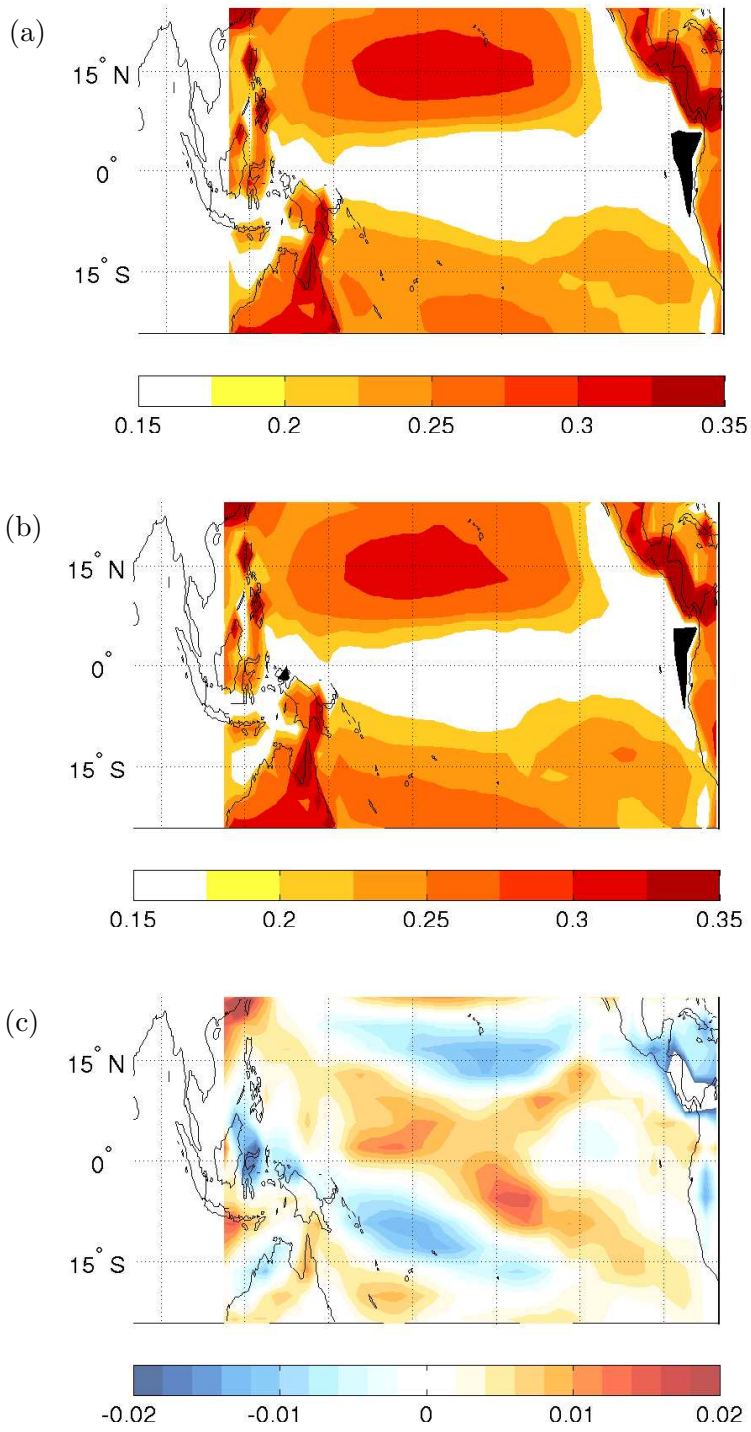

Figure 4.9: Annual mean u_* (ms^{-1}), the friction velocity, over the tropical Pacific, from (a) present day and (b) 8.5ka runs of paleoCCSM. (c) shows the difference between the 8.5ka and present day runs.

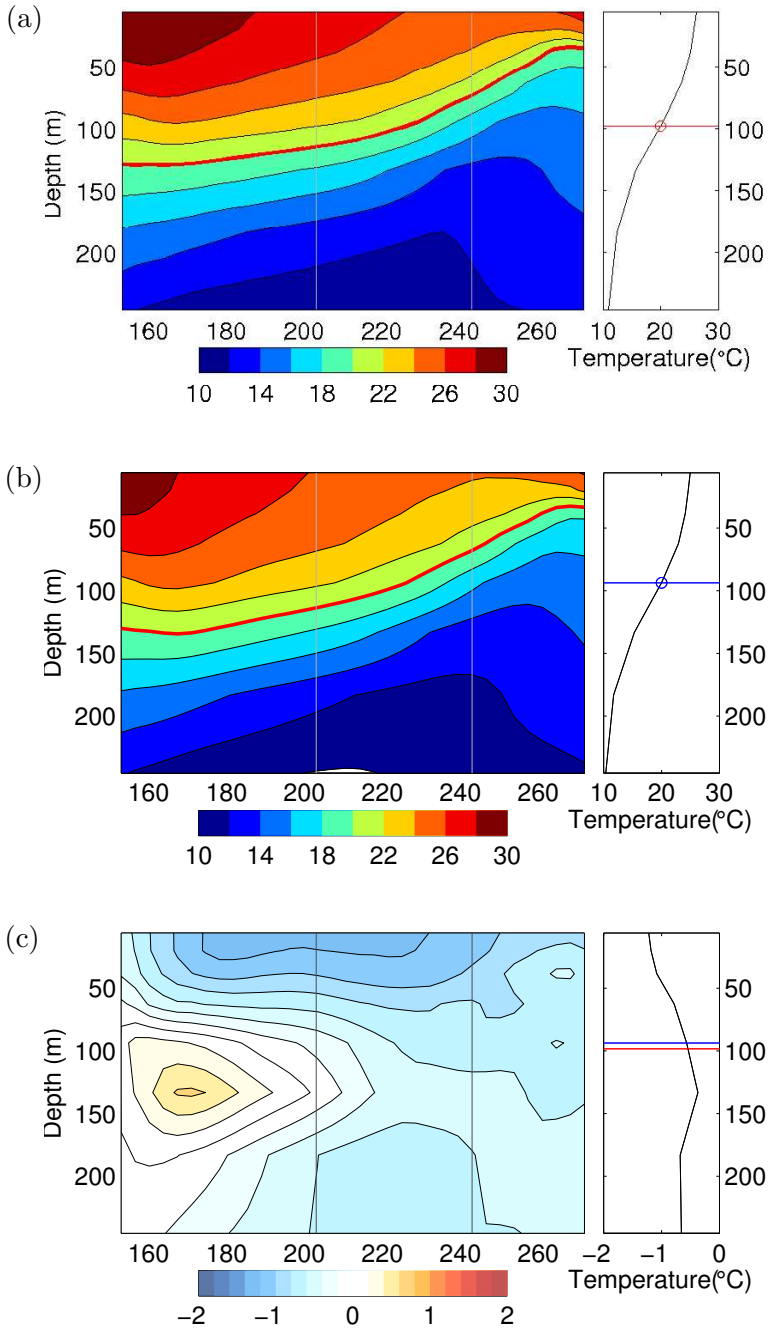

Figure 4.10: Temperature averaged over 2.5°N-2.5°S. Left panels show depth plotted against longitude. Grey lines in left panel indicate the longitudinal extent of the averages shown in right panels which are the temperature averaged over 2.5°N-2.5°S and 205°E-245°E. This average is plotted against depth in the right panels with blue (red) lines showing height of 20°C isotherm in averaged region at 8.5ka (present). (a) shows an average for $CCSMp$, (b) for $CCSM8.5$, (c) shows difference $CCSM8.5 - CCSMp$.

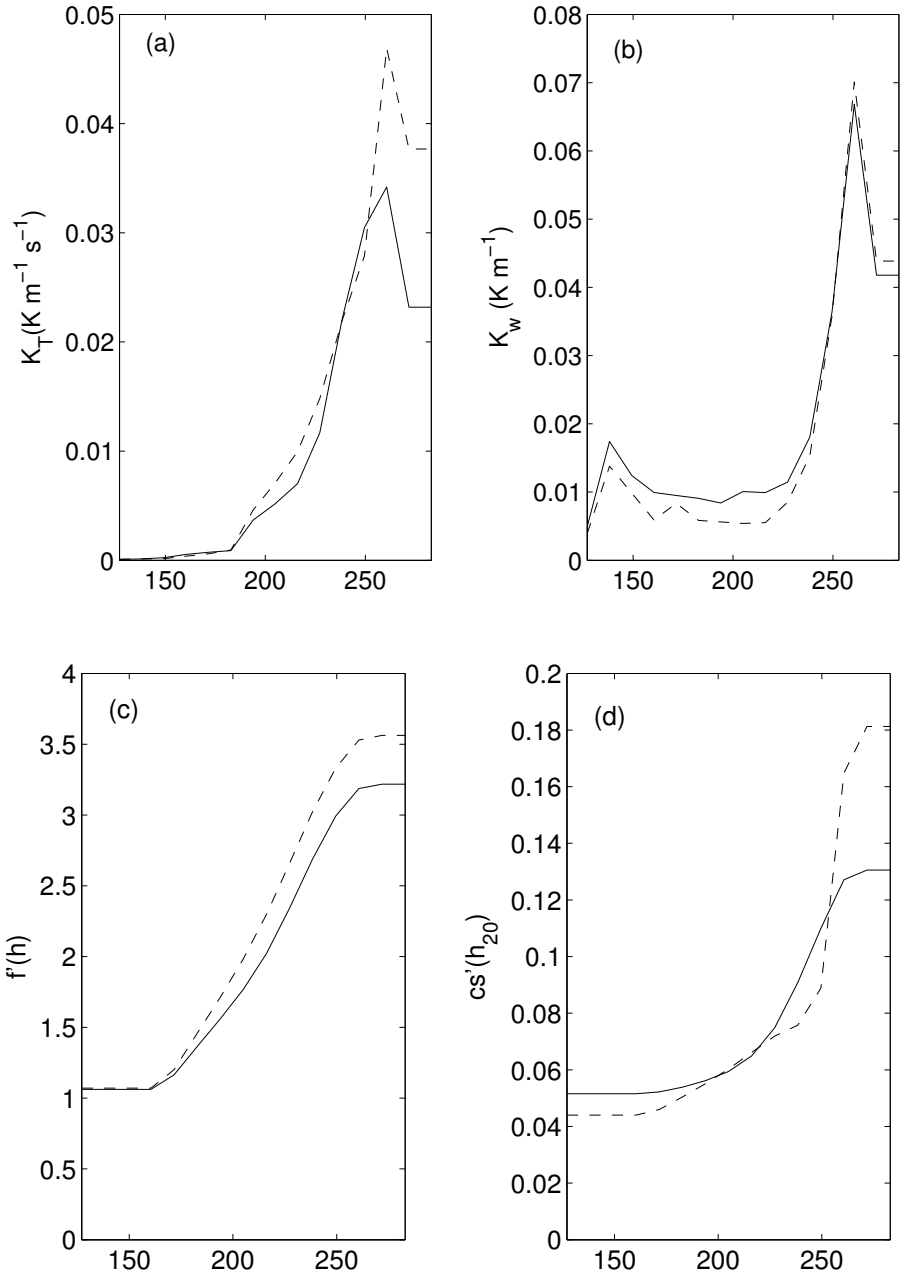

Figure 4.11: K_w and K_T averaged over 5°N-5°S. (a) K_T, solid line for $CCSMp$, dashed for $CCSM8.5$. (b) K_w along the equator, solid line for $CCSMp$, dashed for $CCSM8.5$. (c) $\frac{\partial f}{\partial h}$, solid line for $CCSMp$, dashed for $CCSM8.5$. (d) $\frac{\partial cs}{\partial h_{20}}$ along the equator, solid line for $CCSMp$, dashed for $CCSM8.5$.

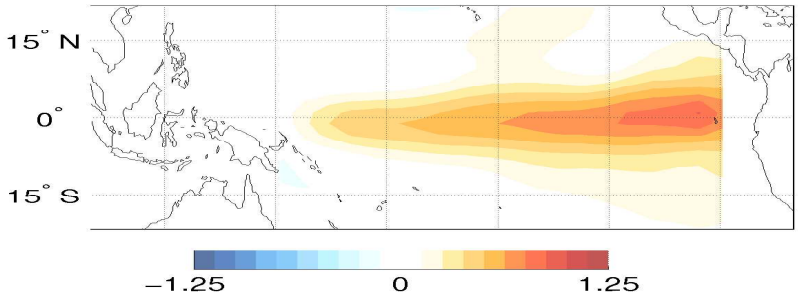

Figure 4.12: EOF 1 for SST anomalies from $CCSM8.5$. Contours are in °C.

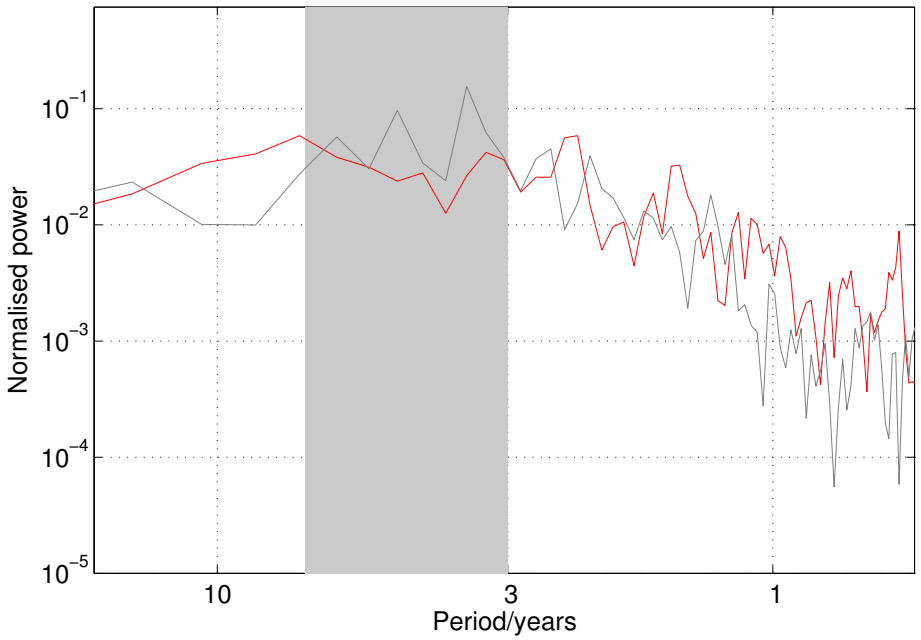

Figure 4.13: Power spectrum of the nino3 index from $CCSM8.5$. The red line is power spectral estimates from $CCSM8.5$, the grey line from the Kaplan dataset.

Pattern a

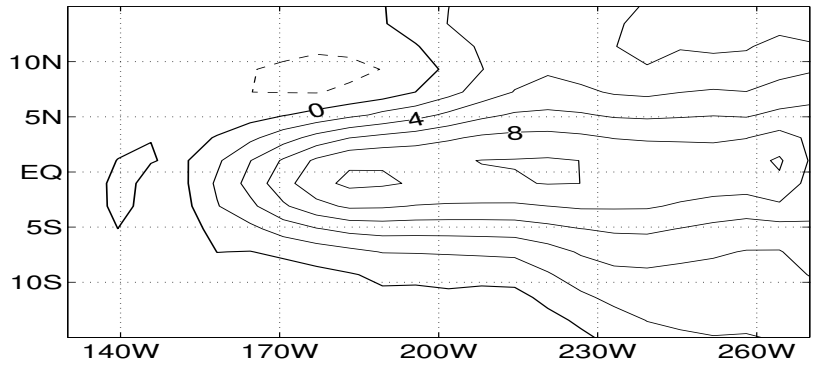

Pattern b

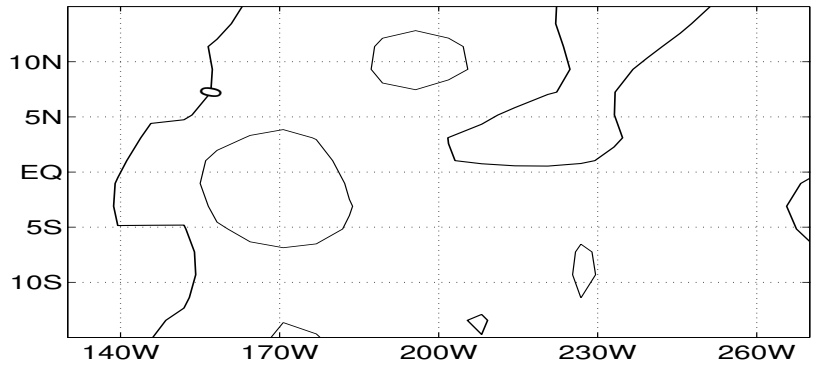

Figure 4.14: The SST part of the ENSO mode from $CCSMp$ The mode evolves $a \rightarrow b \rightarrow -a \rightarrow -b$ over 3.3 years. The contour interval is arbitrary but the same in each panel.

Pattern a

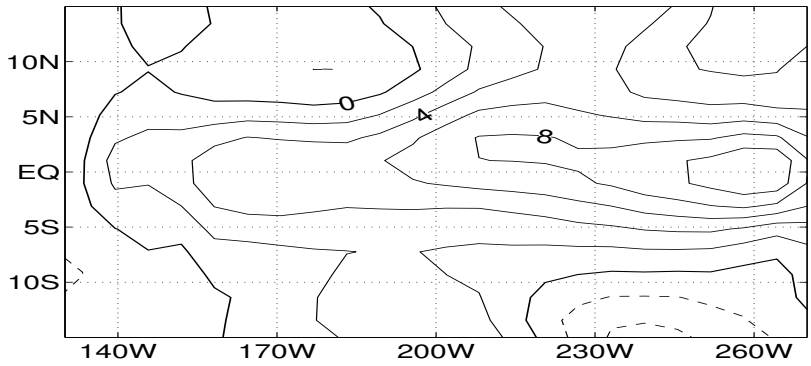

Pattern b

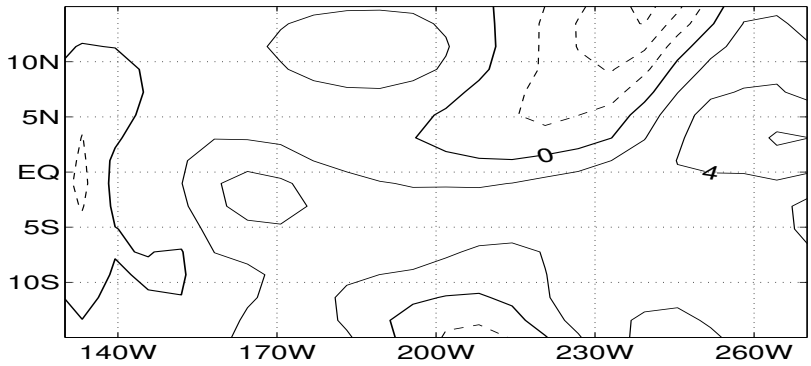

Figure 4.15: The SST part of the ENSO mode from $CCSM8.5$. The mode evolves $a \rightarrow b \rightarrow -a \rightarrow -b$ over 3.8 years. The contour interval is arbitrary but the same in each panel.

Pattern a

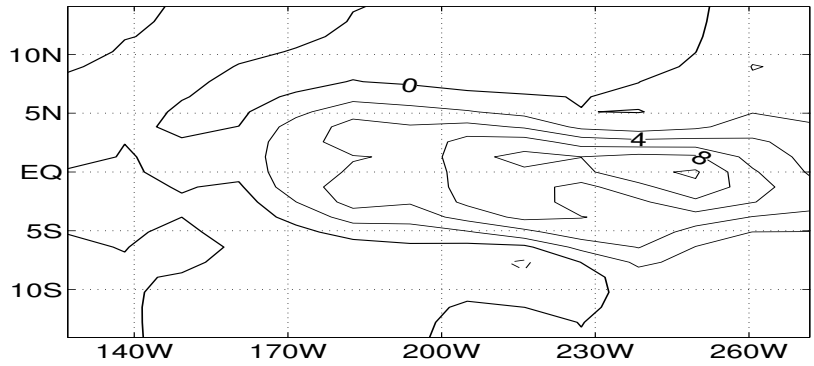

Pattern b

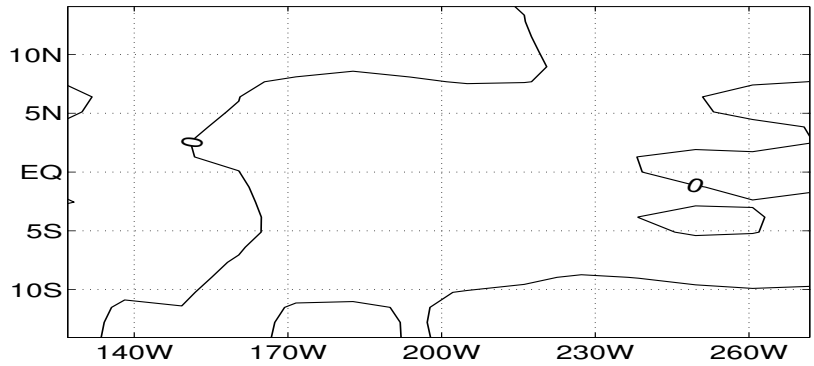

Figure 4.16: The SST part of the ENSO mode from *LOAMp*. The mode evolves $a \rightarrow b \rightarrow -a \rightarrow -b$ over 2.2 years. The contour interval is arbitrary but the same in each panel.

Pattern a

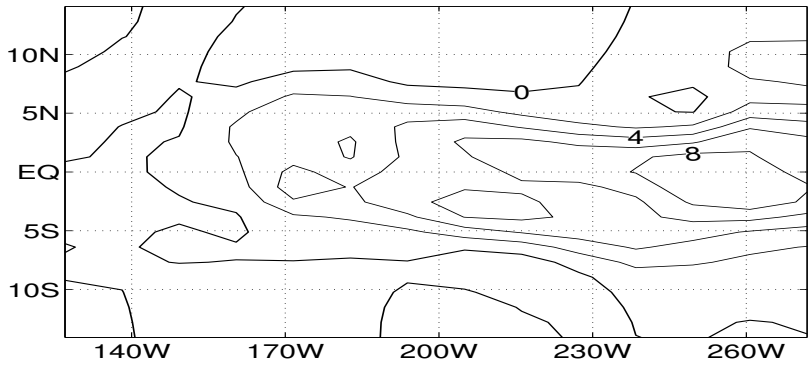

Pattern b

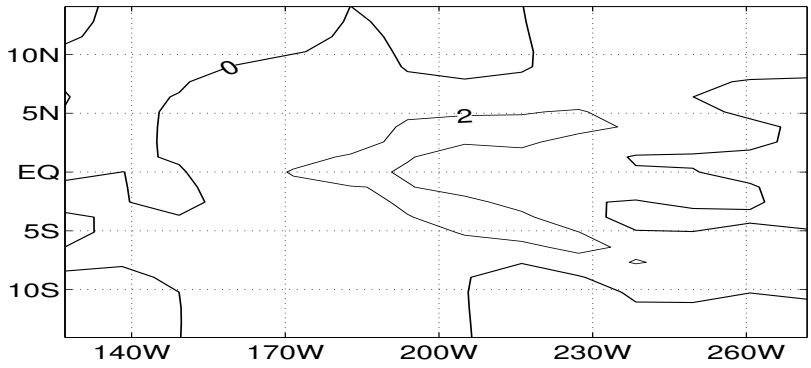

Figure 4.17: The SST part of the ENSO mode from *LOAM*8.5. The mode evolves $a \rightarrow b \rightarrow -a \rightarrow -b$ over 2.9 years. The contour interval is arbitrary but the same in each panel.

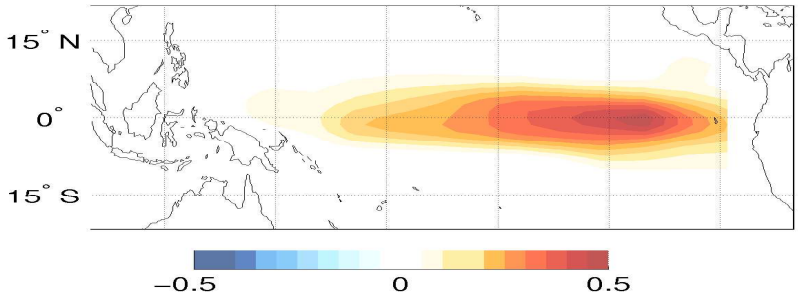

Figure 4.18: EOF 1 for SST anomalies from $LOAMp$. Contours are in °C.

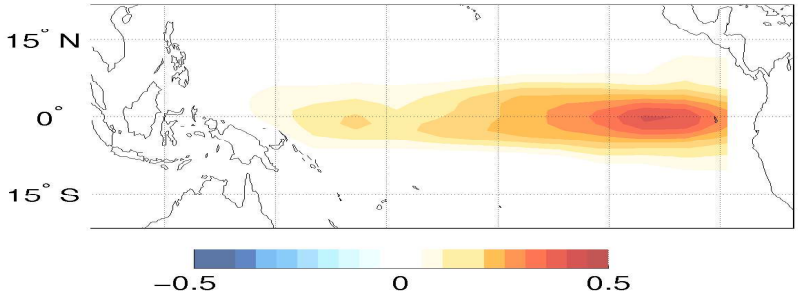

Figure 4.19: EOF 1 for SST anomalies from $LOAM8.5$. Contours are in °C.

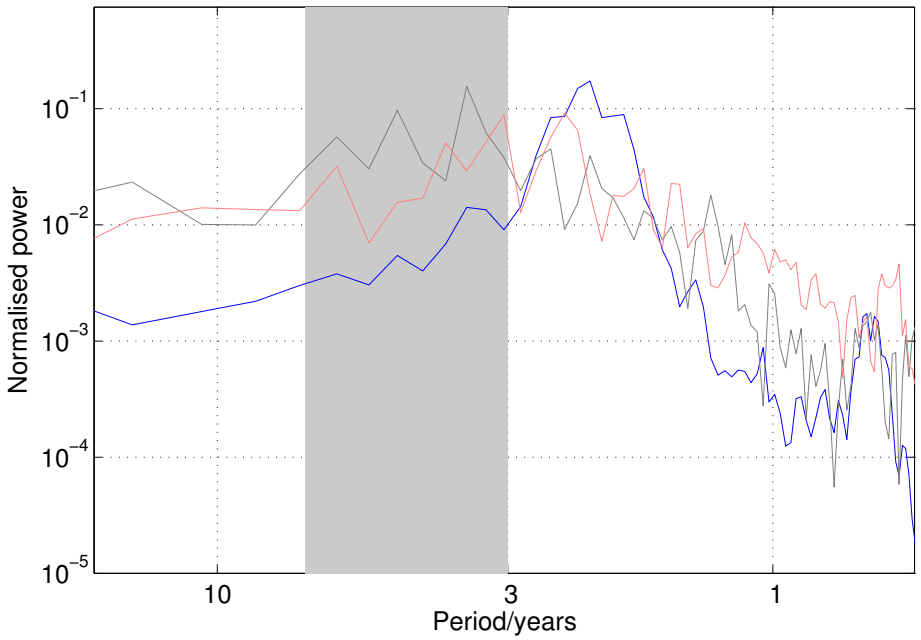

Figure 4.20: Power spectral estimates of the nino3 index. The blue line is for $LOAMp$, the light red line for $CCSMp$ and the grey line from Kaplan SST.

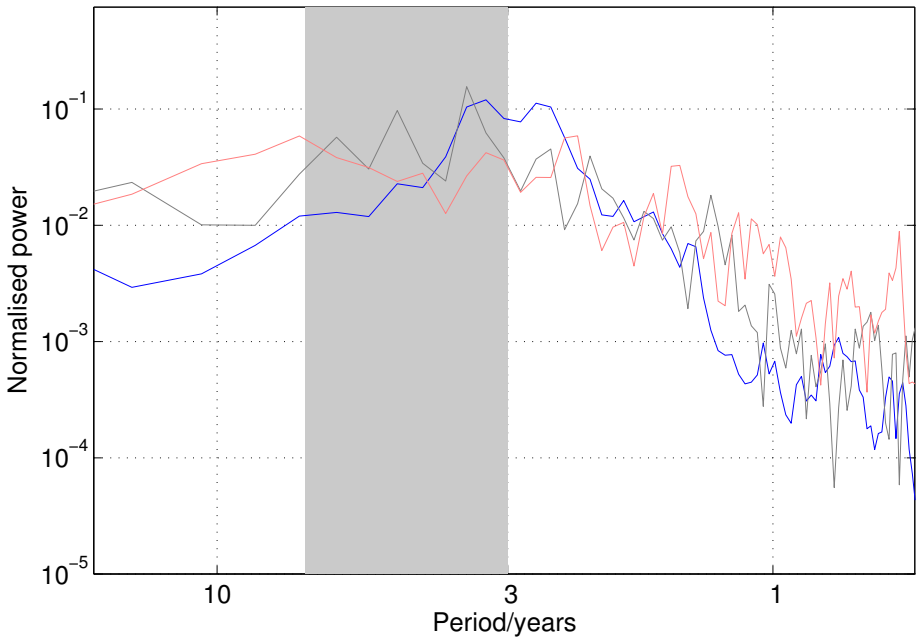

Figure 4.21: Power spectral estimates of the nino3 index. The blue line is for $LOAM8.5$, the light red line for $CCSM8.5$ and the grey line from Kaplan SST.

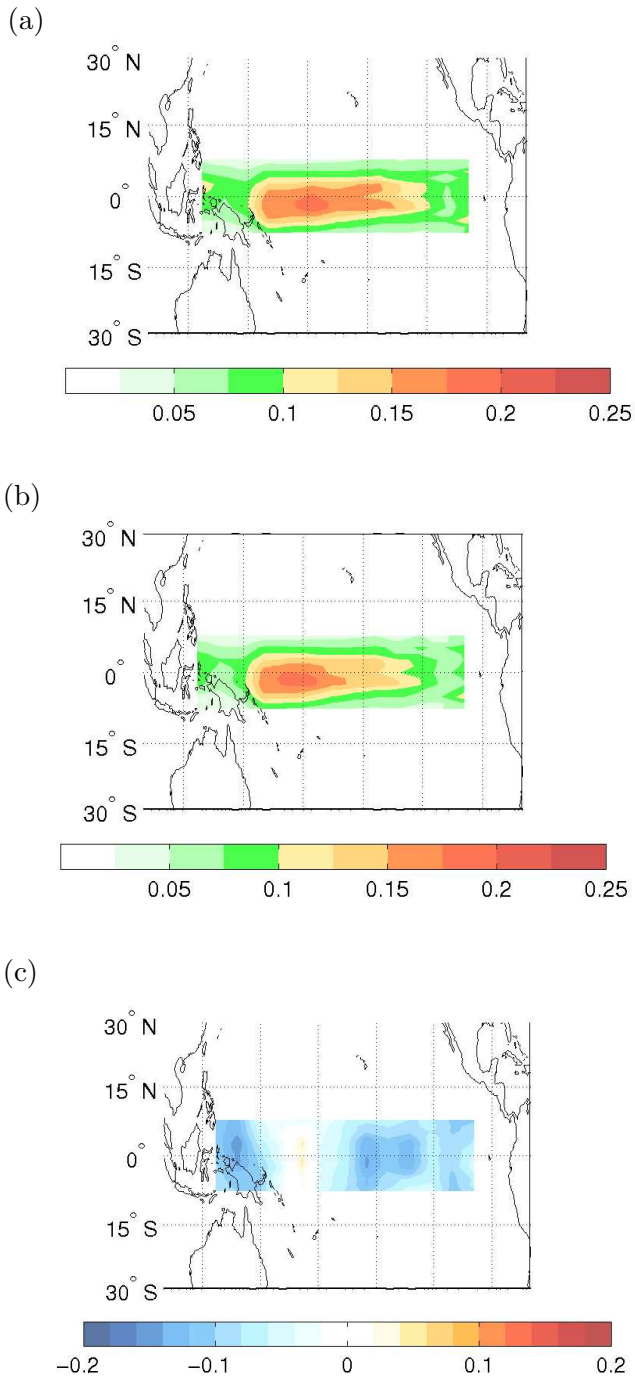

Figure 4.22: Variance in zonal wind $((ms^{-1})^2)$ for the linearised Gill atmosphere forced by SST anomalies from the present day paleoCCSM run. (a) shows the atmosphere from $LOAMp$ and (b) from $LOAM8.5$. (c) shows the difference between the variance in (a) and (b) as a fraction of the variance shown in (a)

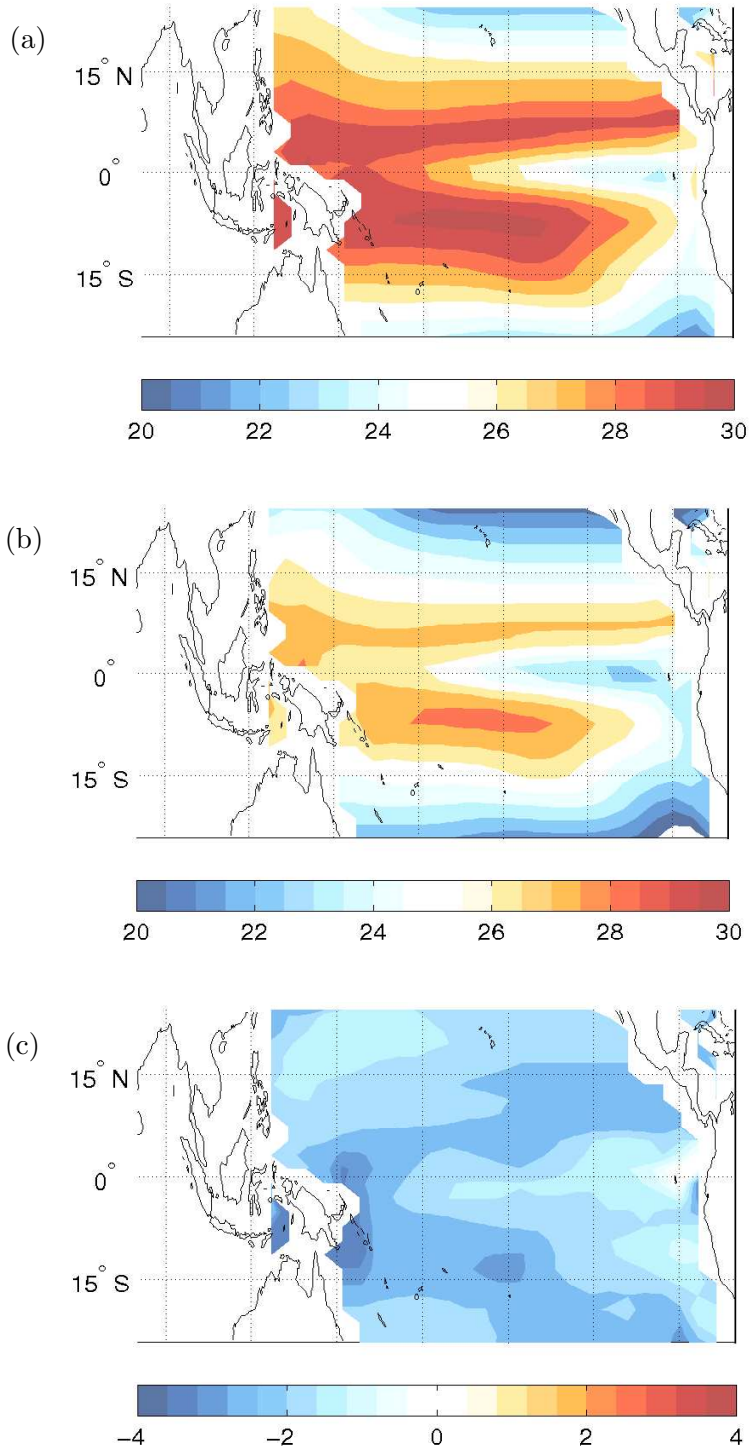

Figure 4.23: Annual mean net SST (°C), over the tropical Pacific, from (a) present day and (b) LGM runs of paleoCCSM. (c) shows the difference between the LGM and present day runs.

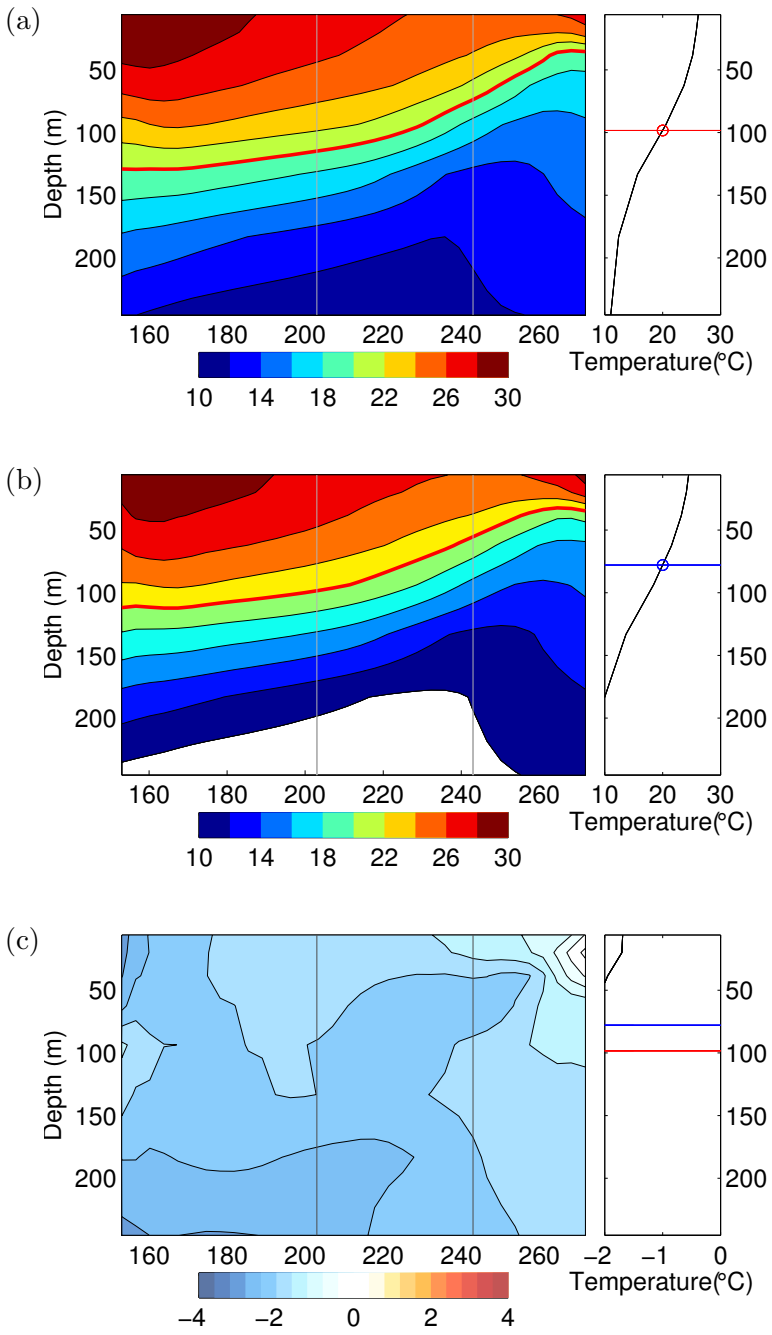

Figure 4.24: Temperature averaged over 2.5°N-2.5°S. Left panels show depth plotted against longitude. Grey lines in left panel indicate the longitudinal extent of the averages shown in right panels which are the temperature averaged over 2.5°N-2.5°S and 205°E-245°E. This average is plotted against depth in the right panels with blue (red) lines showing height of 20°C isotherm in averaged region at LGM (present). (a) shows an average for $CCSMp$, (b) for $CCSMlgm$, (c) shows difference $CCSMlgm - CCSMp$.

Chapter 5

Conclusions

5.1 Summary

We have shown, in Chapter 4, that it is possible to explain the observed reduction in the variance of the nino3 index from the present to 8.5ka in the paleoCCSM in terms of the annual mean cooling of the tropical Pacific SST. The cooler SST at 8.5ka, compared to the present, reduces the windstress response to SST in the model and thus reduces the coupling strength between the atmosphere and ocean. This then leads to a more stable ENSO mode. The change in the temperature beneath the ocean surface is shown to decrease the stability of the coupled system and also alters the spatial pattern of the model's ENSO: the peak in the SST variance due to ENSO is shifted farther to the east at 8.5ka than at present. This shift in the peak of the ENSO mode is seen to have the effect of increasing the period of the ENSO mode. In stochastic runs of LOAM, no change in the amplitude of the noise forcing is required in order to get the same variance in nino3 at present and 8.5ka as in paleoCCSM: the mean state changes alone are sufficient to explain the reduction in nino3 variance at 8.5ka. Also shown in Chapter 4 was that any change in the seasonal cycle of the SST at 8.5ka was not important in stabilising the ENSO mode. This is counter to the widely held hypothesis of Clement et al. (2000), that the seasonal cycle of the SST and wind at 8.5ka is the cause of the reduced variance due to ENSO. That the mechanism of Clement et al. (2000) is not present in paleoCCSM, and as is shown in Appendix A, that it is not even consistent within the original ZCM, means that extreme caution should be used when citing it as being responsible for the reduction in ENSO in the early Holocene.

We have shown in Chapter 3 that when the new system for calculating realistic back-

ground states and subsurface parameterisation is used with observed data, the ENSO mode that results in LOAM is stable and has a period that closely matches estimates of the ENSO mode period from empirical models.

As was shown in Chapter 2 there are significant differences in all of the background states between the newly calculated states and those that were originally used in the ZCM. Since the new background states represent a truer representation of the mean state than the original background states, and the other parameters that need to be specified in LOAM were chosen to make the simplified atmosphere and ocean components of LOAM the best representation of the real atmosphere and ocean possible, with no assumptions about the resulting behaviour of the coupled model, the resulting coupled mode stability is as true a reflection of the stability of the true ENSO mode as can be modelled by LOAM. Since the ENSO mode in LOAM resembles the empirically calculated mode in its spatial and temporal characteristics, it is fair to assume that the ENSO mode in LOAM is modelling the ENSO mode in nature. The fact that this mode is stable lends weight to the hypothesis that the true ENSO mode is a linearly stable mode of the coupled system and that it is the noise that gives the observed irregularity. This is further reinforced by the fact when the values of the western boundary reflection and ocean damping that gave an unstable ENSO mode in the ZCM are used in LOAM with the new background states, the resulting ENSO mode is still stable.

5.2 Criticisms

The most obvious criticism of the present study is that although we have explained the reduction of the ENSO variability in CCSM, does the CCSM actually do a good job of modelling the real system? Zelle et al. (2005) have questioned both how well paleoCCSM models ENSO at present and how well the model reacts to changes in climate forcing. They show that the pattern of the windstress anomalies in the CCSM are too tightly constrained meridionally and that this tends to artificially increase the stability (and also reduce the

period) of the CCSM ENSO. They then hypothesise that this artificially high stability causes the CCSM to be too insensitive to mean state changes. This insensitivity to mean state changes could explain the modest reduction in the variance of nino3 at 8.5ka compared to the estimates of Tudhope et al. (2001).

A possible source of the reduced variance of ENSO in nature is a reduction in the stochastic forcing. However, since LOAM accurately captured the reduction in the variance of nino3 from CCSM without changing the amplitude of the noise forcing, there is no need to call upon changes in the stochastic forcing as a possible explanation for the reduced ENSO variance in the CCSM. Nonetheless, it is possible that at 8.5ka the uncorrelated wind noise that is thought to excite the real ENSO was either weaker or its spatial pattern was less favourable for exciting the ENSO mode. One known source of stochastic forcing for ENSO is the Seasonal Footprinting Mechanism (S.F.M., Vimont et al., 2003), which is shown to explain about 30% of the variance in nino3 at present. When we repeat the analysis of Vimont et al. (2003) using the CCSM ouput we find that although the SFM is present in the CCSM it is not as important as it is proposed to be in nature. Using output from the present day run we find that the one year lagged correlation between the NPO index of Vimont et al. (2003) and the cold tongue index (CTI, the average of the SST between 180-270°W, 6°N-6°S) is 0.25, this compares to 0.59 from the observations. Furthermore, we find that there is no change in the SFM at 8.5ka in the CCSM: the one year lagged correlation between the NPO and CTI at 8.5ka is 0.28. Thus although changes to the stochastic forcing could be important in nature it is not important in the CCSM.

One last criticism of the present study is that the piecemeal alteration of the background states is not physically consistent. Although this is indeed the case, the method used in this study allows us to gain insight into which background state changes are the most important in causing a change in the behaviour of ENSO. Having come up with suitable null hypotheses it is then possible to devise self-consistent experiments for GCMs to test the applicability of these hypotheses.

5.3 Discussion

One common problem in paleoclimate research is the lack of communication between the theoreticians and the observationalists. The common call from the theoreticians is that the observers never look in the right place: from the observers it is that the theoreticians fail to explain where the right place to look is and what the right variable to look for is. In order to confirm or refute the present hypothesis, paleo-evidence for an annual mean cooling of the SST over the whole tropical Pacific, especially in the equatorial wave guide, is needed. At present there are data that demonstrate that the SST was possibly cooler in the far east Pacific (Koutavas and Lynch-Stieglitz, 2003), although there is still much discussion concerning the interpretation of these data. In the far west Pacific there is agreement between the two records (Gagan et al., 1998; Stott et al., 2004) that the SST was warmer there during the early Holocene. These two records, however, are sited in the far west, farther west than is important in affecting the air-sea coupling that we propose as important in reducing the ENSO variability. Thus the presently available data do not allow us to confirm the veracity of the present hypothesis.

A further issue in the interpretation of proxy data of ENSO is whether we can assume that the spatial structure of ENSO should remain the same in different climates. We recall that the 8.5ka CCSM run showed a markedly different spatial structure in its ENSO than the present day run, thus we might expect that in nature the spatial pattern of ENSO was also different. Thus we need to exercise caution when taking point data sources from around the Pacific and trying to fit them into a picture that does not allow for a change in the spatial structure of ENSO.

In terms of more general implications of the present work, the outlined method for incorporating mean state conditions into the ZCM is a very useful tool for examining ENSO in any model. Because ENSO plays such an important role in the global climate system and has large human impacts around the globe, for example in Australia, North East Brazil

and Indonesia (Power, 1991; Rao and Hada, 1990), knowledge of how the phenomenon may change in the future is of crucial importance. With most global climate models showing significant climate change in the future due to the increasing greenhouse gas concentrations, it would be well to know what the effect of this changed climate on ENSO will be. To date there is almost no consensus amongst climate models as to what the future holds for ENSO. Merryfield (2006) showed that in a subset of fifteen of the IPCC models, the sense of the change of the modelled ENSO when the models were run with doubled CO_2, was evenly split: five models gave less ENSO variability, three gave more and the remaining seven showed no change. However, since even the fifteen best models from the IPCC set chosen by Merryfield (2006), fail to capture the observed characteristics of ENSO one may question how well they might model any change in ENSO. Using the method outlined in this thesis to assimilate model mean states into LOAM we can eliminate the realism of the model ENSO as a source of uncertainty. We know that the ZCM captures the physics that underlie ENSO at present, and we have shown that it can also accurately model changes in ENSO variability caused by a mean state change. Thus, if we assimilate mean states from the various IPCC model runs into LOAM, we know that any change in ENSO is solely due to the change in the background states not due to a fundamental change in the physics that underlie the modelled ENSO. In this way we have a tool with which we can consistently analyse how ENSO will react to altered mean states that result from increased greenhouse gas forcing. This does presuppose that the change in the modelled mean state is accurate. This is a valid assumption since amongst the IPCC models there is at least agreement on the sense of the change in the mean state, even if not the amplitude; this is more than can be said of the modelled changes in ENSO, which do not even agree on the sense of any change.

Bibliography

Baker, P., C. Rigsby, G. Seltzer, S. Fritz, T. Lowenstein, N. Bacher, and C. Veliz, 2001: Tropical climate changes at millennial and orbital timescales on the bolivian altiplano. *Nature*, **409**, 698–701.

Battisti, D., 1988: Dynamics and thermodynamics of a warming event in a coupled tropical atmosphere ocean model. *Journal of the Atmospheric Sciences*, **45**(20), 2889 – 2919.

Battisti, D. and A. Hirst, 1989: Interannual variability in a tropical atmosphere ocean model - influence of the basic state, ocean geometry and nonlinearity. *Journal of the Atmospheric Sciences*, **46**(12), 1687 – 1712.

Behringer, D. and Y. Xue, 2004: Evaluation of the global ocean data assimilation system at NCEP: The Pacific Ocean. In *Eighth Symposium on Integrated Observing and Assimilation Systems for Atmosphere, Oceans, and Land Surface*. AMS 84th Annual Meeting, Washington State Convention and Trade Center, Seattle, Washington.

Berger, A., 1978: Long-term variations of daily insolation and quaternary climatic changes. *J. Atmos. Sci.*, **35(12)**, 2362–2367.

Bourassa, M. A., S. R. Smith, and J. J. O'Brien, 2001: A new FSU winds and flux climatology. In *11th Conference on Interations of the Sea and Atmosphere, San Diego, CA, Amer. Meteor. Soc.*

Broecker, W. and T. Stocker, 2006: The Holocene CO2 rise: anthropogenic or natural? *EOS Transactions of the American Geophysical Union*, **87**(3), 27–29.

Brown, J., M. Collins, and A. Tudhope, 2006: Coupled model simulations of mid-Holocene ENSO and comparisons with coral oxygen isotope records. *Advances in Geosciences*, **6**(1), 29 – 33.

Bush, A., 1999: Assessing the impact of mid-holocene insolation on the atmosphere-ocean system. *Geophy. Res. Lett.*, **26**, 99–102.

Bush, A., 2001: Simulating climates of the Last Glacial Maximum and of the mid-Holocene: wind changes, atmosphere-ocean interactions and the tropical thermocline. In *The Oceans and Rapid Climate Change: Past, Present and Future*, D. Seidov, B. J. Haupt, M. M., editor. Geophysical Monograph Series, 294.

Bush, M., B. Hansen, D. Rodbell, G. Seltzer, K. Young, B. Leon, M. Abbott, M. Silman, and W. Gosling, 2005: A 17000-year history of andean climate and vegetation change from laguna de chochos, peru. *Journal Of Quaternary Science*, **20**(7-8), 703 – 714.

Carton, J., G. Chepurin, and X. Cao, 2000b: A simple ocean data assimilation analysis of the global upper ocean 1950-1995, part 2: results. *J. Phys. Oceanogr.*, **30**, 311–326.

Carton, J., G. Chepurin, X. Cao, and B. Giese, 2000a: A simple ocean data assimilation analysis of the global upper ocean 1950-1995, part 1: methodology. *J. Phys. Oceanogr.*, **30**, 294–309.

Chang, P., J. L., L. H., and M. FLugel, 1996: Chaotic dynamics versus stochastic processes in El Niño-Southern Oscillation in coupled ocean-atmosphere models. *Physica D*, **98**(6-7), 301–320.

Clement, A., R. Seager, and M. Cane, 2000: Suppression of el ni-o during the mid-holocene by changes in the earth's orbit. *Paleoceanography*, **15**, 731–737.

Colinvaux, P. and E. Schofield, 1976a: Historical ecology in the Galapagos Islands. I. a Holocene pollen record from El Junco Lake, Isla San Cristobal. *J. of Ecology*, **64**, 986–1012.

Colinvaux, P. and E. Schofield, 1976b: Historical ecology in the galapagos islands. ii. holocene spore record from el junco lake, isla san cristobal. *J. of Ecology*, **64**, 1013–1026.

Devilliers, S., B. Nelson, and A. Chivas, 1995: Biological-controls on coral Sr/Ca and delta-O-18 reconstructions of sea-surface temperatures. *Science*, **269**(5228), 1247 – 1249.

DeVries, T.J., L. O. and A. Diaz, 1997: Determining the early history of ENSO. *Science*, **276**, 965–966.

Dykoski, C., R. Edwards, H. Cheng, D. Yuan, Y. Cai, M. Zhang, Y. Lin, J. Qing, Z. An, and J. Revenaugh, 2005: A high-resolution, absolute-dated Holocene and deglacial Asian monsoon record from Dongge Cave, China. *Earth and Planetary Science Letters*, **233**(1-2), 71 – 86.

Gagan, M., L. Ayliffe, D. Hopley, J. Cali, G. Mortimer, J. Chapell, M. McCulloch, and M. Head, 1998: Temperature and surface-ocean water balance of the mid-Holocene tropical western Pacific. *Science*, **279**, 1014–1018.

Gill, A., 1980: Some simple solutions for heat-induced Tropical circulation. *Quarterly Journal of the Royal Meteorological Society*, **106**(449), 447 – 462.

Goddard, L. and S. Philander, 2000: The Energetics of El Niño and La Niña. *Journal of Climate*, **13**(1), 1496–1516.

Johnson, S., 1999: *Markov Model Studies of the El Niño-Southern Oscillation*. PhD thesis, University of Washington, 143.

Jolly, D., I. Prentice, R. Bonnefille, A. Ballouche, M. Bengo, P. Brenac, G. Buchet, D. Burney, J. Cazet, R. Cheddadi, T. Edorh, H. Elenga, S. Elmoutaki, J. Guiot, F. Laarif, H. Lamb, A. Lezine, J. Maley, M. Mbenza, O. Peyron, M. Reille, and I. Reynaud-Farrera, 1998: Biome reconstruction from pollen and plant macrofossil data for Africa and the Arabian peninsula at 0 and 6000 years. *Journal Of Biogeography*, **25**(6), 1007 – 1027.

Kalnay, E., M. Kanamitsu, R. Kistler, W. Collins, D. Deaven, L. Gandin, M. Iredell, S. Saha, G. White, J. Woollen, Y. Zhu, M. Chelliah, W. Ebisuzaki, W. Higgins, J. Janowiak, K. Mo, C. Ropelewski, J. Wang, A. Leetmaa, R. Reynolds, R. Jenne, and D. Joseph, 1996: The NCEP/NCAR 40-year reanalysis project. *Bull. Amer. Meteor. Soc.*, **77**(3), 437–470.

Kaplan, A., M. Cane, Y. Kushnir, A. Clement, M. Blumenthal, and B. Rajagopalan, 1998: Analyses of global sea surface temperature 1856-1991. *Journal Of Geophysical Research-Oceans*, **103**(C9), 18567 – 18589.

Kitoh, A. and S. Murakami, 2002: Tropical pacific climate at the mid-Holocene and the Last Glacial Maximum simulated by a coupled ocean-atmosphere general circulation model. *Paleoceanography*, **17**(3), 1047.

Koutavas, A. and J. Lynch-Stieglitz, 2003: Glacial-Interglacial dynamics of the eastern equatorial Pacific cold tongue intertropical convergence zone system reconstructed from oxygen isotope records. *Paleoceanography*, **18**(4), 1089.

Lea, D., D. Pak, C. Belanger, H. Spero, M. Hall, and N. Shackleton, 2006: Paleoclimate history of Galapagos surface waters over the last 135,000 yr. *Quaternary Science Reviews*, **25**(11-12), 1152 – 1167.

Lees, B. and a. D. P. Y. Lu, 1992: Thermoluminescence dating of dunes at Cape St Lambert, East Kimberleys, Northwestern Australia. *Marine Geology*, **106**, 131–139.

Liu, Z., S. P. Harrison, J. Kutzbach, and B. Otto-Bliesner, 2004: Global monsoons in the mid-Holocene and cceanic feedback. *Climate Dynamics*, **22**(2-3), 157–182.

Liu, Z., J. Kutzbach, and L. Wu, 2000: Modeling climatic shift of El Niño variability in the Holocene. *Geophy. Res. Lett.*, **27**, 2265–2268.

Liu, Z., B. Otto-Bliesner, J. Kutzbach, L. Li, and C. Shields, 2003: Coupled climate simulation of the evolution of global monsoons in the Holocene. *Journal of Climate*, **16**(15), 2472 – 2490.

Mantua, N. and D. Battisti, 1995: Aperiodic variability in the Zebiak-Cane coupled ocean-atmosphere model: air-sea interactions in the western equatorial pacific. *Journal OF Climate*, **8**(12), 2897 – 2927.

McGlone, M., A. Kershaw, and V. Markgraf, 1992: El Nño-Southern Oscillation climatic variability in Australasian and South American paleoenvironmental records. In *El Nño. Historical and Paleoclimatic Aspects of the Southern Oscillation*, Diaz, H. and Markgraf, V., editors. Cambridge University Press, New York, 476.

McPhaden, M., A. J. Busalacchi, R. Cheney, J.-R. Donguy, K. S. Gage, D. Halpern, M. Ji, P. Julian, G. Meyers, G. T. Mitchum, P. P. Niiler, J. Picaut, R. W. Reynolds, N. Smith, and K. Takeuchi, 1998: The Tropical Ocean Global Atmosphere (TOGA) observing system: A decade of progress. *J. Geophys. Res.*, **103**, 14,169–14,240.

Merryfield, W., 2006: Changes to ENSO under CO_2 Doubling in a Multi-Model Ensemble. *Journal of Climate*, **19**, 4009–4027.

Moy, C., G. Seltzer, D. Rodbell, and D. M. Anderson, 2002: Variability of El Niño/Southern Oscillation activity at millennial timescales during the Holocene epoch. *Nature*, **420**, 162–165.

Otto-Bliesner, B. and E. Brady, 2001: Tropical Pacific variability in the NCAR Climate System Model. *Journal of Climate*, **14**(3), 3587–3607.

Otto-Bliesner, B. L., 1999: El Niño/La Niña and Sahel precipitation during the middle Holocene. *Geophy. Res. Lett.*, **26**, 87–90.

Otto-Bliesner, B. L., E. C. Brady, S. Shin, Z. Liu, and C. Shields, 2003: Modeling El Nino and its tropical teleconnections during the last glacial-interglacial cycle. *Geophy. Res. Lett.*, **30**, DOI:10.1029/2003GL018553.

Penland, C. and P. Sardeshmukh, 1995: The optimal-growth of tropical sea-surface temperature anomalies. *Journal OF Climate*, **8**(8), 1999 – 2024.

Power, S., 1991: The El-Niño Southern Oscillation and beer sales in the Australian region. *Bulletin of the Australian Meteorological and Oceanographic Society*, **4**, 47–48.

Rao, V. B. and K. Hada, 1990: Characteristics of rainfall over Brazil: Annual and variations and connections with the Southern Oscillation. *Theor. Appl. Climatol.*, **42**.

Rasmusson, E. M. and T. H. Carpenter, 1982: Variations in tropical sea surface temperature and surface wind fields associated with the Southern Oscillation/El Niño. *Mon. Wea. Rev.*, **110**, 354–384.

Reynolds, R., N. Rayner, T. Smith, D. Stokes, and W. Wang, 2002: An improved in situ and satellite sst analysis for climate. *J. Climate*, **15**, 1609–1625.

Sandweiss, D., K. Maasch, R. Burger, J. R. III, H. Rollins, and A. Clement, 2001: Variation in Holocene El Nño frequencies: climate records and cultural consequences in ancient Peru. *Geology*, **29**, 603–606.

Seager, R., S. Zebiak, and M. Cane, 1988: A model of the tropical pacific sea-surface temperature climatology. *Journal Of Geophysical Research-Oceans*, **93**(C2), 1265 – 1280.

Shulmeister, J. and B. Lees, 1995: Pollen evidence from tropical Australia for the onset of an ENSO-dominated climate at c4000 BP. *Holocene*, **5**(1), 10 – 18.

Smith, N. R., 1995a: An improved system for tropical ocean sub-surface temperature analyses. *J. Atmos. Oceanic Technol.*, **12**, 850–870.

Smith, N. R., 1995b: The BMRC ocean thermal analysis system. *Aust. Meteor. Mag.*, **44**, 93–110.

Stott, L., K. Cannariato, R. Thunell, G. Haug, A. Koutavas, and S. Lund, 2004: Decline of surface temperature and salinity in the western tropical Pacific Ocean in the Holocene epoch. *Nature*, **431**(7004), 56 – 59.

Street-Perrott, F. and R. Perrott, 1993: Holocene vegetation, lake levels and climate of Africa. In *Global climates since the Last Glacial Maximum.*, et al., W. H., editor. The University of Minnesota Press, Minneapolis, USA, 318.

Taylor, K., 2001: Summarizing multiple aspects of model performance in a single diagram. *Journal of Geophysical Research-Atmospheres*, **106**(D7), 7183 – 7192.

Thompson, C., 1998: *A linear, stochastic, dynamical model of El Niño-Southern Oscillation.* PhD thesis, University of Washington, 235.

Thompson, C. and D. Battisti, 2000: A linear stochastic dynamical model of ENSO. Part I: Model development. *Journal of Climate*, **13**(15), 2818 – 2832.

Thompson, C. and D. Battisti, 2001: A linear stochastic dynamical model of ENSO. part ii: analysis. *Journal of Climate*, **14**(4), 445 – 466.

Thompson, L., E. Mosley-Thompson, and K. Henderson, 2000: Ice core paleoclimate records in tropical South America since the Last Glacial Maximum. *Journal of Quaternary Science*, **15**, 377–394.

Tudhope, A., C. Chilcott, M. McCulloch, E. Cook, J.Chappell, R. Ellam, D. Lea, J. Lough, and G. Shimmield, 2001: Variability in the El Niño-Southern Oscillation through a glacial-interglacial cycle. *Science*, **291**, 1511–1517.

Vancampo, E., J. Duplessy, and M. Rossignolstrick, 1982: Climatic conditions deduced from a 150-kyr oxygen isotope pollen record from the Arabian Sea. *Nature*, **296**(5852), 56 – 59.

Vimont, D., J. Wallace, and D. Battisti, 2003: The seasonal footprinting mechanism in the pacific: implications for enso. *Journal of Climate*, **16**(16), 2668 – 2675.

Vuille, M., 1999: Atmospheric circulation over the Bolivian Altiplano during dry and wet periods and extreme phases of the Southern Oscillation. *International Journal of Climatology*, **19**(14), 1579 – 1600.

Wang, B. and S. An, 2002: A mechanism for decadal changes of ENSO behavior: roles of background wind changes. *Climate Dynamics*, **18**(6), 475 – 486.

Wells, L. and J. Noller, 1997: Determining the early history of ENSO. *Science*, **276**, 966–966.

Zebiak, S., 1984: *Tropical atmosphere-ocean interaction and the El Niño-Southern Oscillation phenomenon.* PhD thesis, M.I.T., 261.

Zebiak, S. E. and M. A. Cane, 1987: A Model El-Niño Southern Oscillation. *Monthly Weather Review*, **115**, 2262–2278.

Zelle, H., G. J. van Oldenborgh, G. Burgers, and H. Dijkstra, 2005: El Niño and Greenhouse Warming: Results from Ensemble Simulations with the NCAR CCSM. *Journal of Climate*, **18**(22), 4669–4683.

Appendix A

The Cane and Clement Model

A.1 Introduction

The first modelling study that set out to specifically examine ENSO during the Holocene was that of Clement et al. (2000). Using the ZCM they found that there were fewer warm ENSO events during the early Holocene than there are today. Fewer warm events implies a reduction in the variance due to ENSO. This agrees with the observational data, such as Tudhope et al. (2001), although no estimate of the amplitude of the reduction in the variance is given in Clement et al. (2000).

In this chapter we will take another look at the experiments done by Clement et al. (2000), using the B88 version of the ZCM. We shall first describe the experiment as run by Clement et al. (2000) then show that similar results may be obtained using the B88M. We shall then re-examine the Clement et al. (2000) interpretation of the results using LOAM and propose another explanation for the observed change: that the ZCM is unable to produce very strong cold anomalies, so when the model is forced into a regime where on average the model SST tends to be colder than at present, the time series of nino3 SST becomes skewed towards the warm, and its variance is reduced.

Throughout this chapter we shall frequently refer to anomalies. Although the ZCM is an anomaly model, it is found that when the model is run with its standard configuration the time mean of the model output is not zero. This complicates the definition of an anomaly, so for the sake of clarity we shall refer to the model output as anomalies. Changes in the *average* state will refer to changes in those anomalies, time averaged over 500 years, and the states about which the anomalies are prescribed will be referred to as the *background*

state.

A.2 The Original Experiment and its Interpretation

Clement et al. (2000) use the ZCM to simulate the entire of the Holocene, from 12ka to the present. We recall that the major external forcing that changed over the course of the Holocene was the seasonal cycle of the insolation. The ZCM does not explicitly incorporate the effect of the sun its parameterisations, thus, to mimic its effect, Clement et al. (2000) insert a surface heating anomaly into the SST tendency equation. This anomalous heating varies over the course of the year in order to simulate the change in the seasonal cycle of the insolation (compared to the present day insolation). Note, however, that the background states about which the anomalies are prescribed are not changed in the model. If we do not change the background state in the model we implicitly assume that the mean state of the tropical Pacific does not change.

The model is then run for twelve thousand years with the surface heating anomaly varying over those twelve thousand years in order as per the orbital forcing calculated by Berger (1978). Clement et al. (2000) define a warm event as any occasion that the mean winter nino3 anomaly is greater than 3°C, and they find that in the twelve thousand years of the run, there were fewer of these events in the early Holocene than there were in the present, see fig. A.1(a). Figure A.1(a) shows the number of warm events that occur during a five hundred year moving window, and the average amplitude of the nino3 anomaly of the events in that 500 year window, is shown in fig. A.1(b). This figure is reproduced from Clement et al. (2000). One can see that not only are there fewer warm events during the early Holocene, but also that their average amplitude is decreased compared to the present. Figure A.2 shows results from a similar calculation, using the B88M, rather than ZCM. We see again that there are fewer warm events and that the 500 year average of nino3 is smaller during the early Holocene. This is, qualitatively, the same result as using the ZCM, which is unsurprising since the two models are very similar. Note that the definition of a

"warm event" when using B88M is slightly different to that using ZCM: the mean winter nino3 anomaly must be greater than 1.5°C when using B88M. This redefinition is necessary because the different parameterisations in the two models give rise to different amplitudes of the nino3 index.

Figure A.3(a) shows that the variance of the nino3 index, in a moving 500 year window, from the B88m is reduced in the early Holocene compared to the present. This is consistent with the proxy evidence. The data of Tudhope et al. (2001) shows a reduction in the variance of coral $\delta_{18}O$ of around 80% from the present to 6.5ka. This is larger than the 20 % reduction in variance from the present to 6.5ka that the B88M run shows. Figure A.3(b) shows that the average winter nino3 index increases from 10ka to the present, and fig. A.3(c), shows that from 10ka to 6ka the winter nino3 is positively skewed.

Clement et al. (2000) invoke seasonal changes of the easterly trades to explain the suppression of the model's ENSO. Shown in fig. A.4 are the average seasonal differences between 500 year windows centred on 8ka and today. We see that the east-west SST gradient is stronger during September-February at 8ka than it is today. This stronger zonal SST gradient leads to stronger easterly trades during those seasons. Clement et al. (2000) propose that this intensification of the trades, which begins around September, acts to reduce the intensity of westerly wind anomalies associated with a growing warm ENSO event. Since, in both nature and the model, warm ENSO events tend to begin to grow around September the strengthened easterly winds at this time are proposed to be very effective at reducing the amplitude of the westerly winds associated with a growing warm ENSO event.

What is unclear in this interpretation is how mean anomalies and transient anomalies can interact in the model. The proposed mechanism implies that anomalies on seasonal timescales can effect anomalies on shorter timescales In the experiment as devised by Clement et al. (2000), the background states about which the anomalies operate are not changed, so any changes to ENSO are not brought about by changes in the mean state, per se. It is interesting to examine the change to ENSO that would result from changes in

the background state that are the same size as the change in the mean anomalies shown in fig. A.5. This can be examined by using LOAM

A.3 The Effect of Mean State Anomalies as Mean State

The annual average differences between the mean anomalies over a 500 year window centred on 8ka and the present, for all background states, are shown in fig. A.5 [1]. In order to examine the effect of these differences on the model ENSO when they are treated as background state changes, the T80 version of LOAM was run with its original background states and with background states which were calculated as the original background states with the seasonal differences, shown in fig. A.5, added to them. In order to change the parameterisation that pretains to subsurface temperature anomalies due to movements in the thermocline, the difference in the annual mean thermocline depth anomaly ($\bar{h}$ in the lineariasation of $T_s(h)$ used in Thompson (1998)) is also added to the original background state value.

The variance of the nino3 index, relative to the control run of LOAM, and the period and decay rate of the ENSO mode for various models are shown in Table A.1. Relative to the control run of LOAM using the T80 parameter set, $LOAM$(T80), the run with the complete set of background mean states altered by the 8ka differences, $LOAM + 8ka$, has a much more unstable ENSO mode, the decay rate is .91 year^{-1} compared to .80 year^{-1}. This says that the effect of the mean anomalies, if they are thought of as changes to the background state act to destabilise the ENSO mode. This is the opposite of the effect on the ENSO mode that Clement et al. (2000) propose: that the mean anomalies act to stabilise the ENSO mode. Since it is possible that the change in the seasonal cycle of surface wind and SST do act as stabilisers of the ENSO mode, but that changes in other fields act to destabilise the mode, and thus mask the stabilisation due to SST and windstress, three further experiments were carried out. $LOAM + u_{atm} + T_{atm}$, uses the original background

[1] Figure A.5 shows the annual mean change, however, in LOAM seasonally varying fields are used.

states everywhere but in the surface zonal wind and SST, where the 8ka difference is added is added; $LOAM + u_{atm}$ adds only the surface zonal wind to the original background states; and $LOAM + T_{atm}$ adds only SST from 8ka to original background states. In theses three experiments, changes to the ENSO mode can only come from windstress or SST. As can be seen in Table A.1, in none of these experiments does the ENSO mode become more stable. Thus, we see that if the mean anomalies from 8ka are treated as a change in the background state, they have the effect of destabilising the ENSO mode.

These experiments with LOAM show that the effect of a mean anomaly is different to the effect of a change in the background state. In the next section we will examine what causes the reduction in the variance of nino3 when B88M is run as per Clement et al. (2000).

A.4 What is going on in the simulation of Clement et al. (2000)

The definition of an event in Clement et al. (2000) is a mean winter nino3 anomaly of greater than 3°C. This anomaly is the SST that comes directly out of the model. We see in fig. A.1(b) that there is a change in the size of the 500 year mean winter nino3 SST anomaly over the course of the Holocene. Given that there is a change in the 500 year average nino3 anomaly, a better definition of a warm event would be when the average winter nino3 is greater than some threshold about the 500 year mean winter nino3 anomaly. The event statistics when an event is so defined, are shown in fig. A.6. The exact definition of an event in fig. A.6 is any winter in the 500 year window when the average nino3 is 1.5°C warmer, or colder, than the 500 year average winter nino3. With this definition we see that before 6ka there are no cold events. This is consistent with the change in the skewness, seen in fig. A.3. Before 6ka the skewness is positive, indicating a longer tail on the warm side of the distribution and a shorter tail for cold anomalies. The skewness becomes zero around 6ka: the time at which cold events begin to occur again. The most obvious explanation for this change in skewness is that during the early Holocene the model is saturated and unable to produce very cold anomalies: this removes the end of the cold tail.

This saturation can be explained by examining the function that determines $T_s(h)$ in the SST equation. This function is defined by eqn. 2.8. During the early Holocene the mean nino3 is 0.3 °C cooler than today, this implies that the values of $T_s(h)$ are also generally cooler, which in turn suggests that in the east Pacific h is generally more negative: more negative values of h are consistent with the stronger easterly winds that are seen in fig. A.5(e). This means that $T_s(h)$ is generally evaluated closer to the flat part of the tanh function. In this region of the curve, a change in h results in a negligible change in $T_s(h)$. This means that SST is no longer affected by changes in h. In the present, when h is generally not so negative, $T_s(h)$ is evaluated on the fast changing part of the tanh function, so a change in h will cause a larger change in $T_s(h)$, thus the SST responds more to h. If $T_s(h)$ is insensitive to negative h, as it is during the early Holocene, the model will be saturated with respect to cold events. Since there is no coincident increase in the amplitude of the warm events, the variance of the nino3 index is seen to drop. Thus in the model the reduced ENSO variance comes about because of a non-linear saturation of the subsurface effects - the reduced SST tendency due to changes in a fixed wind forcing. Thus the tell-tale feature of the mechanism that is responsible for the reduction of ENSO variance in Clement et al. (2000) is an increased skewness of the nino3 in the early Holocene. Examination of the skewness of the $\delta^{18}O$ from the coral cores taken by Tudhope et al. (2001) does not show any change to reflect more warm events, the average skewness of the present day coral cores is 0.1 indicating a slight bias towards warm events, at 6.5ka the skewness is -0.4 indicating a bias towards cold events [2]. From this we can concludde that the ZCM is inconsistent with the observations.

[2]Near Papua New Guinea warm ENSO events are characterised by cooler SST and less precipitation which is reflected in more enriched $\delta^{18}O$ at the site; cold event are characterised by more depleted $\delta^{18}O$

A.5 Discussion

We have shown that the mean anomaly as produced by the B88M when treated as a change to the background state does not stabilise the ENSO mode. We have also shown that the observed change in the features of ENSO when the model is run can be explained by the limitation that the model becomes saturated at extreme warm and cold temperatures. Thus the reduction in ENSO observed is the manifestation of a flaw in the model rather than a modelling of some process present in nature.

Table A.1: Variance and properties of the ENSO mode for various experiments where the difference in the mean anomalies at 8ka and the present are added to the present day means in LOAM. Variance comes from a stochastically forced run, with the same amplitude noise for all runs. See text for explanation of individual runs

Model	variance/ variance of $LOAM$(T80)	mode period (years)	mode decay (year^{-1})
$LOAM$(T80)	1	3.9	.80
$LOAM + 8ka$	2.5	3.7	.91
$LOAM + u_{atm} + T_{atm}$	1.5	3.8	.85
$LOAM + u_{atm}$	2.2	3.9	.84
$LOAM + T_{atm}$	1.2	3.7	.81

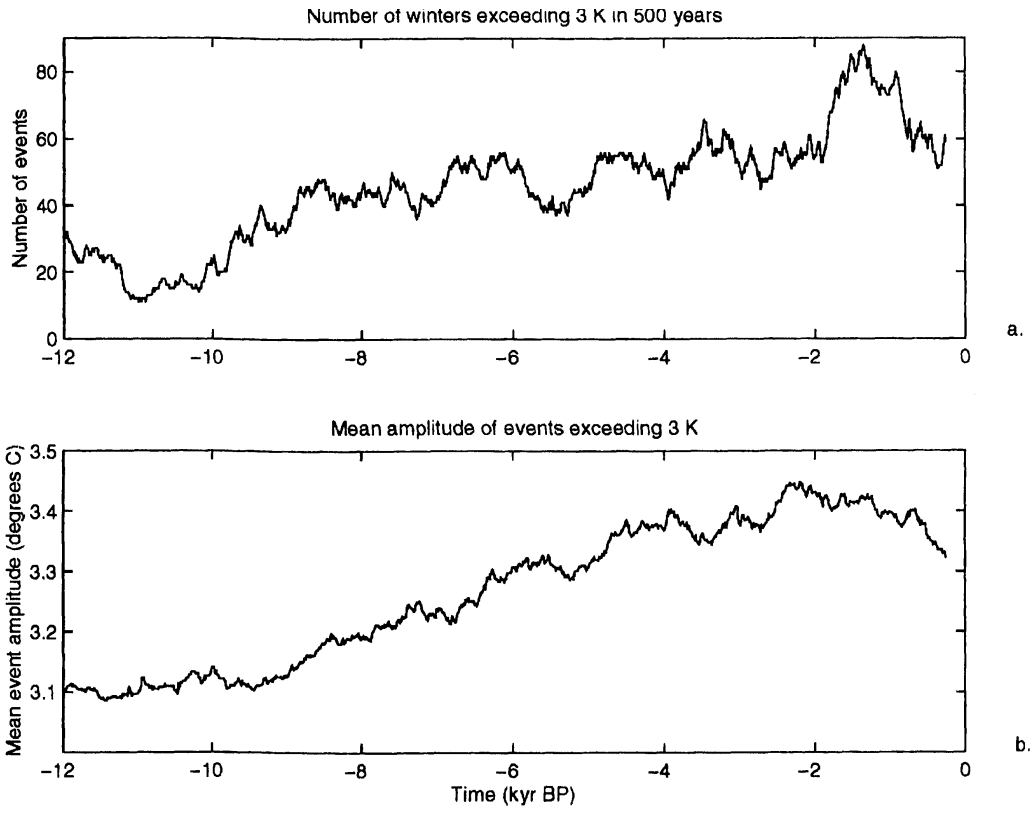

Figure A.1: Event statistics for Zebiak and Cane model. (a) Number of times, in a 500 year window, that the average winter nino3 index is 3°C (b) The average nino3 index of all the events defined in (a). Figure is reproduced from Clement et al. (2000).

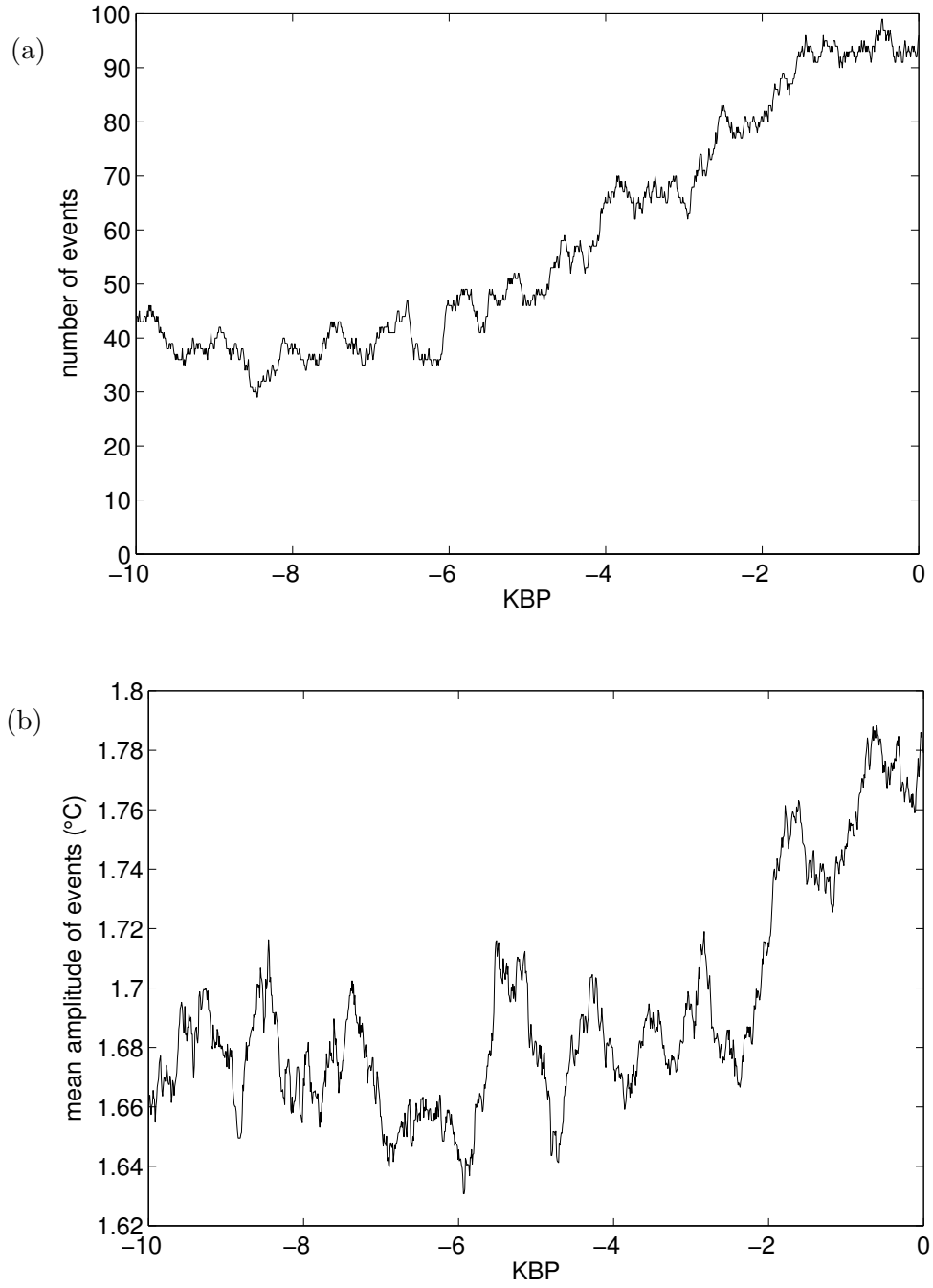

Figure A.2: Event statistics for Battisti model. (a) Number of times, in a 500 year window, that the average winter nino3 index anomaly exceeds 1.5°C. (b) The average nino3 index of the events defined in (a).

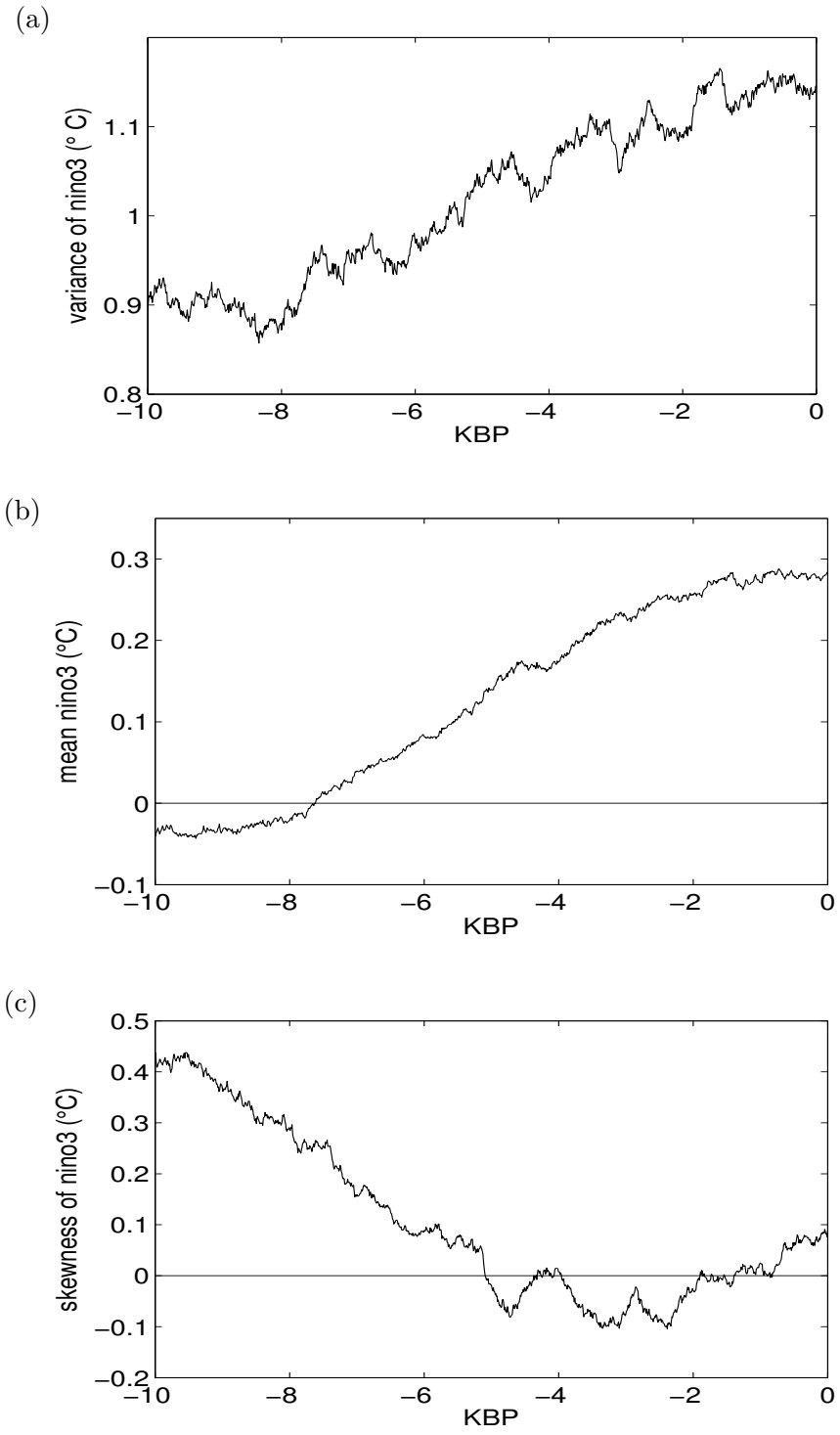

Figure A.3: Statistical moments of the mean winter nino3 SST from the Battisti model. All are calculated in a 500 year moving window. (a) variance, (b) mean, (c) skewness.

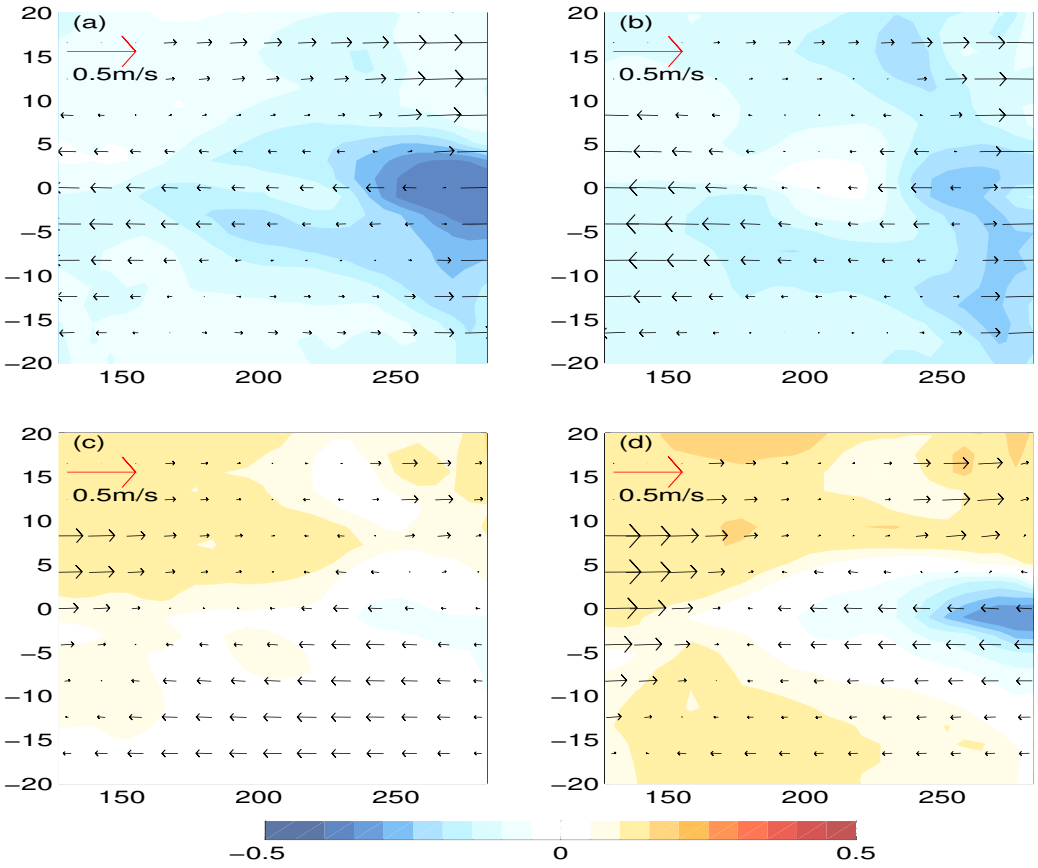

Figure A.4: .

Seasonal mean SST and zonal surface wind anomalies for 8ka-present. (a) December-February, (b) March-May, (c) June-August, (d) September-November. The red arrow indicates a reference zonal wind anomaly of 0.5 ms^{-1}, contours are in °C.

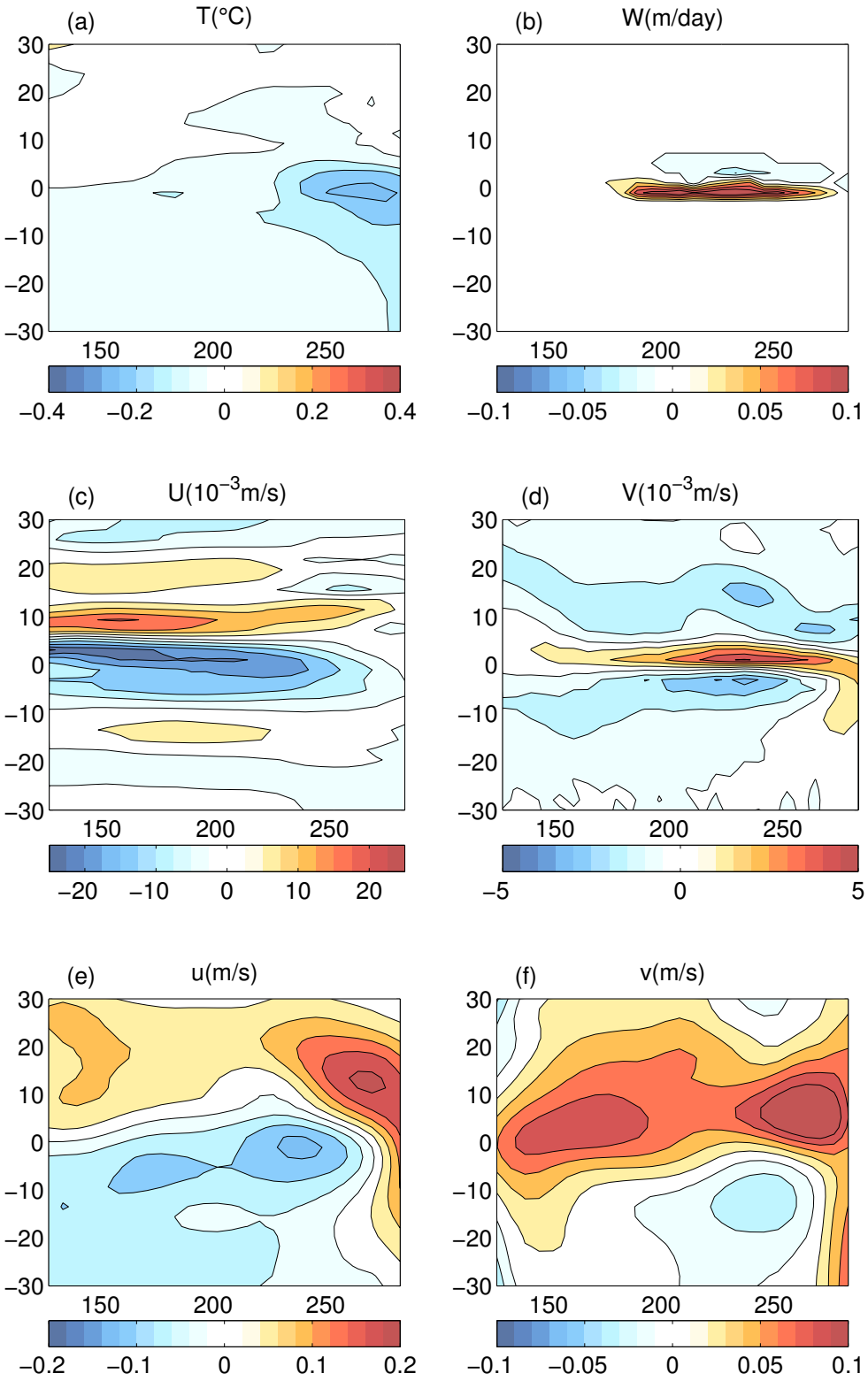

Figure A.5: Differences in the mean anomalies at 8ka and the present, as produced by the B88 model. These are the annual means of the fields that are added to the present means in LOAM. (a) SST, (b) upwelling, (c) zonal current, (d) meridional current, (e) zonal wind and (f) meridional wind.

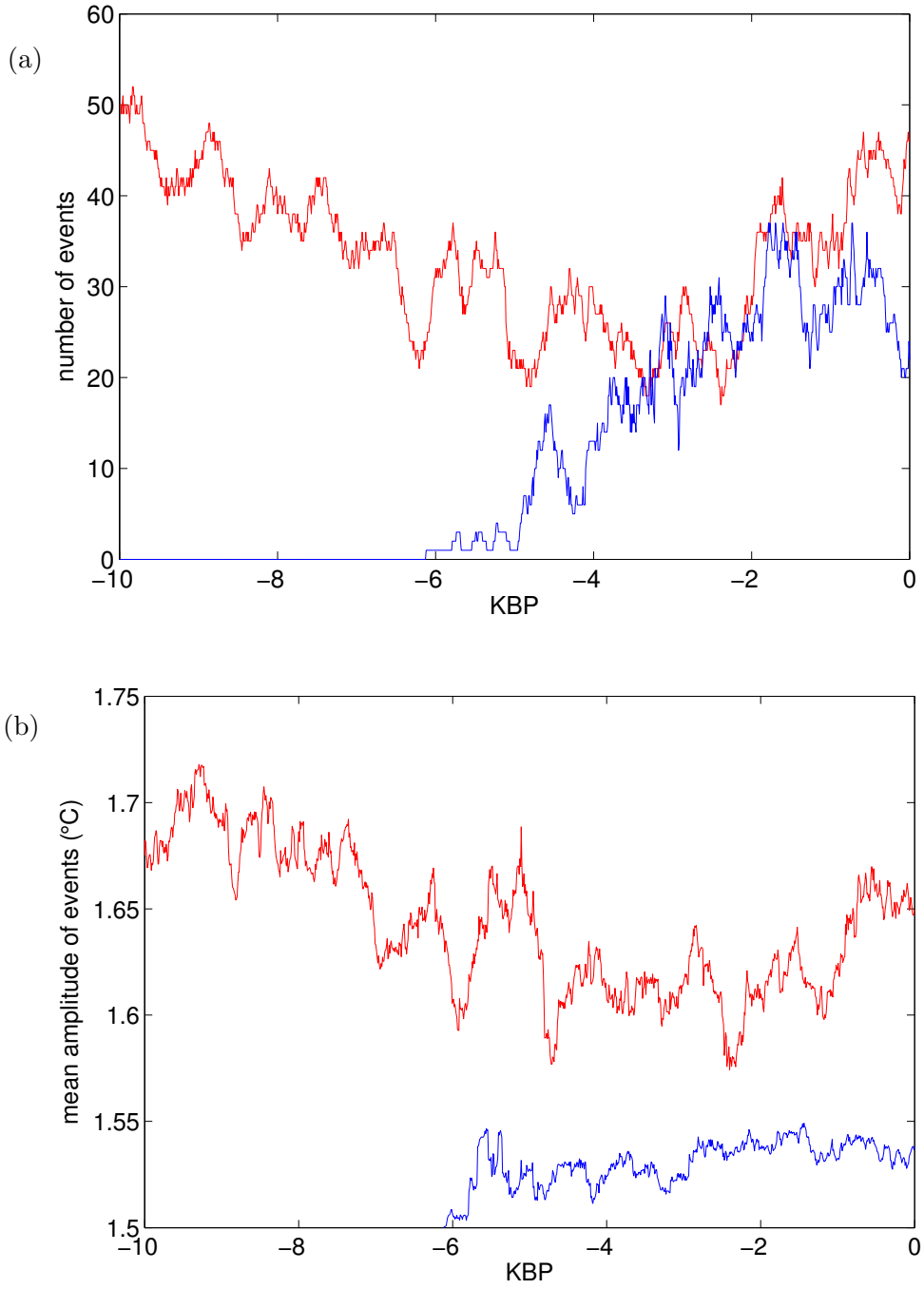

Figure A.6: Event statistics for Battisti model. (a) Number of times, in a 500 year window, that the average winter nino3 index is 1.5°C warmer, red, or colder, blue, than the average winter nino3 of the 500 year window. (b) The average nino3 index of all events, as defined above, relative to the 500 year window average.

Vita

William Henry Gordon Roberts was born in Warrington, U.K. and graduated from the University of Reading with a BSc(Hons) in Physics and Meteorology in 1999. He greatly enjoyed the mumble mumble years spent in the US while getting the PhD.